Experimental Investigation of Flow and Wall Heat Transfer in an Optical Combustor for Reacting Swirl Flows

Suhyeon Park

Dissertation submitted to the faculty of the Virginia Polytechnic Institute and State University in partial fulfillment of the requirements for the degree of

Doctor of Philosophy
in
Mechanical Engineering

Srinath V. Ekkad, Chair
Walter F. O'Brien
Wing F. Ng
Kevin T. Lowe

December 19, 2017
Blacksburg, Virginia, USA

Keywords: Heat transfer, gas turbine combustor, particle image velocimetry, infrared thermography.

ABSTRACT

Experimental Investigation of Flow and Wall Heat Transfer in an Optical Combustor for Reacting Swirl Flows

Suhyeon Park

The study of flow fields and heat transfer characteristics inside a gas turbine combustor provides one of the most serious challenges for gas turbine researchers because of the harsh environment at high temperatures. Design improvements of gas turbine combustors for higher efficiency, reduced pollutant emissions, safety and durability require better understanding of combustion in swirl flows and thermal energy transfer from the turbulent reacting flows to solid surfaces. Therefore, accurate measurement and prediction of the flows and heat loads are indispensable.

This dissertation presents flow details and wall heat flux measurements for reacting flow conditions in a model gas turbine combustor. The objective is to experimentally investigate the effects of combustor operating conditions on the reacting swirl flows and heat transfer on the liner wall. The results shows the behavior of swirling flows inside a combustor generated by an industrial lean pre-mixed, axial swirl fuel nozzle and associated heat loads.

Planar particle image velocimetry (PIV) data were analyzed to understand the characteristics of the flow field. Experiments were conducted with various air flow rates, equivalence ratios, pilot fuel split ratios, and inlet air temperatures. Methane and propane were used as fuel. Characterizing the impingement location on the liner, and the turbulent kinetic energy (TKE) distribution were a main part of the investigation. Proper orthogonal decomposition (POD) further analyzed the data to compare coherent structures in the reacting and non-reacting flows. Comparison between reacting and non-reacting flows yielded very striking differences. Self-similarity of the flow were observed at different operating conditions.

Flow temperature measurements with a thermocouple scanning probe setup revealed the temperature distribution and flow structure. Features of premixed swirl flame were observed in the measurement. Non-uniformity of flow temperature near liner wall was observed ranging from 1000 K to 1400 K. The results provide insights on the driving mechanism of convection heat transfer.

As a novel non-intrusive measurement technique for reacting flows, flame infrared radiation was measured with a thermographic camera. Features of the flame and swirl flow were

observed from reconstructed map of measured IR radiation projection using Abel transformation. Flow structures in the infrared measurement agreed with observations of flame luminosity images and the temperature map. The effect of equivalence ratio on the IR radiation was observed.

Liner wall temperature and heat transfer were measured with infrared thermographic camera. The combustor was operated under reacting condition to test realistic heat load inside the industrial combustors. Using quartz glass liner and KG2 filter glass, the IR camera could measure inner wall surface temperature through the glass at high temperature. Time resolved axial distributions of inner/outer wall temperature were obtained, and hot side heat flux distribution was also calculated from time accurate solution of finite difference method.

The information about flows and wall heat transfer found in this work are beneficial for numerical simulations for optimized combustor cooling design. Measurement data of flow temperature, velocity field, infrared radiation, and heat transfer can be used as validation purpose or for direct inputs as boundary conditions. Time-independent location of peak location of liner wall temperature was found from time resolved wall temperature measurements and PIV flow measurements. This indicates the location where the cooling design should be able to compensate for the temperature increase in lean premixed swirl combustors.

The characteristics on the swirl flows found in this study points out that the reacting changes the flow structure significantly, while the operating conditions has minor effect on the structure. The limitation of non-reacting testing must be well considered for experimental combustor studies. However, reacting testing can be performed cost-effectively for reduced number of conditions, utilizing self-similar characteristics of the flows found in this study.

GENERAL ABSTRACT

Experimental Investigation of Flow and Wall Heat Transfer in an Optical Combustor for Reacting Swirl Flows

Suhyeon Park

The study of flow fields and heat transfer characteristics inside a gas turbine combustor provides one of the most serious challenges for gas turbine researchers because of the harsh environment at high temperatures. Design improvements of gas turbine combustors for higher efficiency, reduced pollutant emissions, safety and durability require better understanding of combustion in swirl flows and thermal energy transfer from the turbulent reacting flows to solid surfaces. Therefore, accurate measurement and prediction of the flows and heat loads are indispensable. This dissertation presents flow details and wall heat flux measurements for reacting flow conditions in a model gas turbine combustor.

The information about flows and wall heat transfer found in this work are beneficial for numerical simulations for optimized combustor cooling design. Measurement data of flow temperature, velocity field, infrared radiation, and heat transfer can be used as validation purpose or for direct inputs as boundary conditions. Time-independent location of peak location of liner wall temperature was found from time resolved wall temperature measurements and PIV flow measurements. This indicates the location where the cooling design should be able to compensate for the temperature increase in lean premixed swirl combustors.

The characteristics on the swirl flows found in this study points out that the reacting changes the flow structure significantly, while the operating conditions has minor effect on the structure. The limitation of non-reacting testing must be well considered for experimental combustor studies. However, reacting testing can be performed cost-effectively for reduced number of conditions, utilizing self-similar characteristics of the flows found in this study.

ACKNOWLEDGEMENTS

I am really grateful to study for a doctorate degree in Mechanical Engineering department at Virginia Tech. I would like to appreciate Dr. Ekkad for offering me the opportunity to work in HEFT lab and APPL team. With his mentorship, he always supported me even when I was depressed with my results. Working experience in the previous project with Dr. Lowe, Dr. Ma and Dr. Ng was a good foundation of my study, in which I was able to improve my abilities. Dr. O'Brien, Dr. Jiangtao Cheng, Dr. von Spakovsky, Dr. Joseph Meadows, and Dr. Borgoltz were very encouraging when I needed their help. And many other professors in VT were my great mentors.

The project couldn't be possible without the sponsors, DOE-NETL University Turbine Systems Research (UTSR) program and Solar Turbines Incorporated. I want to thank the managers Fred X. Liberatore, Ram Srinivasan, Shaun Ho, Hee Koo Moon, Yong W. Kim from Solar Turbines Inc, and Robin Ames from DOE.

It was a fantastic experience to work with David Gomez-Ramirez, who guided my research. Discussions with my colleagues in the group, Sandeep Kedukodi, Yongbin Ji, Siddhartha Gadiraju, Prashant Singh, Shubham Chowdhuri, and Jaideep Pandit were incredibly important to the research and lab works.

It is impossible to name all the people who were part of my education. I want to wish best lucks for Chuyoung Kim, Andrew J. Wickersham, Kris Barboza, Tamar Daniel, Raul Otero, Andrew Boulanger, Vy Nguyen, Mingyang Zhang, Ridge Sibold, Luke Luehr, Edward Turner, Shuo Mao, Stephen Lash, Albrey de Clerck, Wenjiang Xu, Haoting Wang, Yihua Ren, Qingchun Lei, Fan He, Tyler Englerth, Kenneth Brown, Daniel Cadel, Tobias Ecker, Rita Caldwell, Diana Israel, Cathy Hill, officers of Virginia Tech Korean Student Association, administrators of Southern VA Chapter of Korean-American Scientists and Engineers Association, and all my friends in Blacksburg. The struggles during my studies were about engineering, science and technology, but the most valuable thing that I leaned is the warmth of humanity.

TABLE OF CONTENTS

LIST OF FIGURES

LIST OF TABLES

PREFACE

This dissertation is prepared based on manuscripts of previously published articles or the material in preparation for publication. Chapter 1 is an introduction to explain the motivation for current project and basics of gas turbine combustor flow and heat transfer research in general. Since the project is continued form the past research by previous researchers in the group, the introduction is a revisit of the previous work. Chapter 2 describes the combustor used for the later chapters, which was designed and fabricated previously for this project. Chapter 3 reports PIV results including two sets of measurement. The first part of PIV measurement was presented at ASME Turbo Expo 2017, and the other part is in preparation for ASME Turbo Expo 2018. Chapter 4 introduces flow temperature measurement with thermocouple, which is in preparation for at AIAA SciTech 2018. Infrared flame imaging described in Chapter 5 was presented at AITA Conference in Canada 2017. Wall heat transfer measurements in Chapter 6 was a part of presentation at ASME Turbo Expo 2017.

CHAPTER 1. INTRODUCTION

1.1 IMPORTANCE OF GAS TURBINE TECHNOLOGY

Gas turbines are essential in aero-engines and electric power generations, and it is one of the most important area of research in engineering. Energy consumption statistics reported recently states that the amount of natural gas usage is increasing. Concerning the environment issues, renewable energy sources are the most appropriate alternatives to fossil fuels in a long term perspective. However, their costs are not competitive in the beginning stages. Power generation using natural gas is beneficial currently and near future, because of its less effect on the environment compared to other fossil fuels, and technical maturity from the long history of development.

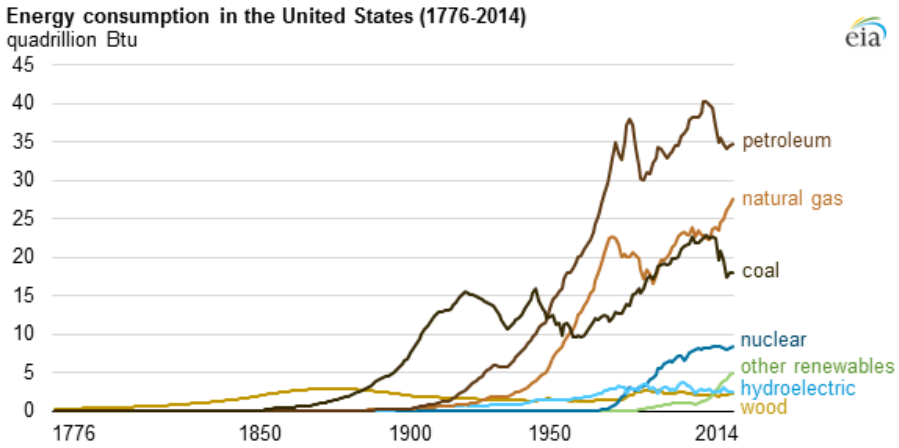

Energy consumption by source in the United States (1776-2014) [1]

The net efficiency of modern combined-cycle gas turbine power plant is over 60% (H-class), which is higher than other types of fossil fuel power generation. Gas turbines are also advantageous with less restrictions on the installation site and the independence of weather and climate. Gas turbines will play a complementary role, even after renewable energy takes over most of the power generation in the future.

This work is motivated by key factors in current gas turbine research, which is increased efficiency and reduced pollutant emissions. For those requirements, higher turbine inlet

temperature is achieved with advanced material and designs of turbine blade, and lean-premixed combustion is more widely used for ground based gas turbines. The complexity of combustor design is increasing consequently.

1.2 BASICS OF COMBUSTOR DESIGN

1.2.1 Efficiency and Turbine Inlet Temperature

Common gas turbine engine is based on open Brayton cycle. Figure 1 shows a schematic of simple configuration and the T-s diagram of the open Brayton cycle.

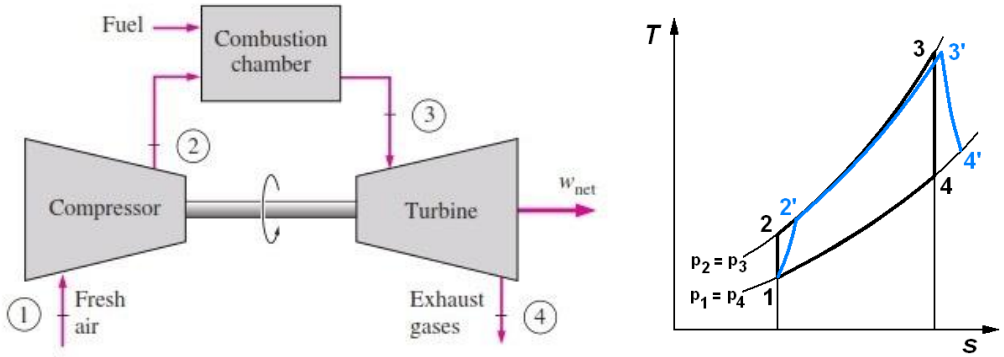

Figure 1. Schematic of Brayton cycle and T-s diagram.

The efficiency (η) of an air-standard ideal Brayton cycle depends on the pressure ratio (r). Equation 1 and 2 shows the efficiency and the power for the ideal cycle [2].

$$\eta = 1 - \left(\frac{1}{r}\right)^{\frac{(\gamma-1)}{\gamma}}, \qquad r = \frac{p_2}{p_1} \tag{1}$$

$$\frac{W}{c_p T_1} = t\left(1 - \frac{1}{r^{(\gamma-1)/\gamma}}\right) - \left(r^{\frac{(\gamma-1)}{\gamma}} - 1\right), \qquad t = \frac{T_3}{T_1} \tag{2}$$

Net specific work generation W increases when the pressure ratio and combustor exit temperature T_3 increase. The pressure ratio can be expressed in terms of inlet T_3 and exit T_4

temperature of turbines using isentropic relation. The equation indicates that the limiting factor of the pressure ratio is the maximum allowable temperature at the turbine inlet.

$$r^{(\gamma-1)/\gamma} = \left(\frac{p_2}{p_1}\right)^{(\gamma-1)/\gamma} = \left(\frac{p_3}{p_4}\right)^{(\gamma-1)/\gamma} = \frac{T_3}{T_4} \quad (3)$$

The higher turbine inlet temperature leads to higher efficiency, higher maximum power, and reduced engine size in accordance. The optimum condition for the work output is achieved when $r^{(\gamma-1)/\gamma} = \sqrt{t}$. Efforts in research are focused on the high turbine inlet temperature for this reason [3]. This relation for the performance of an ideal cycle is also valid for the real engines accounting for losses.

1.2.2 Durability and Emission

Durable design and reduced pollutant emission are two main considerations for combustor performances. A combustor should bear a durability that can be operated at high temperature environment for long lifetime. Thermal barrier coatings and advanced materials extended the lifetime of combustor components [4-7]. The durability of combustor for ground based commercial gas turbines targets 30000 hours of operation [4]. However, there are failures of combustor liners reported in the open literature [4, 8, 9]. Reduced material strength at high temperatures, maximum thermal stresses at the location of maximum temperature gradients, and corrosion affects the combustor durability. [9-11]. Creep and low cycle fatigue (LCF) are the predominant mechanisms of liner failure. Low cycle fatigue is related to startup and shutdown. Creep is slow process of cumulative deformation of material in stress below the yield point. The thermal management, is the most critical part for enhanced durability of combustors and for improved efficiency.

For combustor liner life assessment, transient operation of the engine was simulated by computer modeling [10]. Experimental validation is necessary for the numerical simulation for the confidence of the results, and for the reliability of the modeling. However, the study was limited to qualitative validation on available examples of failed combustors. The authors pointed

out that the experimental data on hot side heat transfer is very limited for different combustor configurations.

Another factor is pollutant emission generated from combustion process. Principal pollutants of primary concerns are nitric oxides (NO_x), unburned hydrocarbons (UHCs) and carbon monoxides (CO). Reducing overall pollutant emission requires two contradicting conditions. Formation rate from atmospheric nitrogen to NO_x increases with increase in flame temperature, but CO and UHC are formed at low flame temperature condition. Reaction mechanisms of NO_x formation are thermal (Zeldovich) mechanism, prompt (Fenimore) mechanism and nitrous oxide (N_2O) mechanism. NO_x emission is significant at temperature above 1850 K, especially for thermal NO_x, which contributes 60% of the total NO_x [12,13]. UHCs result from incomplete combustion of fuel cause by insufficient residence time or low temperature. The optimum flame temperature in consideration of environmental influences is in the range of 1700-1900 K [13].

The lean operation is adapted to many of modern gas turbines to lower the flame temperature and to reduce NOx emissions. The temperature of lean frame ~ 1700 K is still beyond the allowable temperature of liner material (1100 K for common nickel super alloys) [13,14]. Bleed air from the compressor is used as coolant for high temperature component in gas turbine. The amount of the coolant flow rate should be minimized to maintain high turbine inlet temperature. Coolant introduced to the hot gas by film cooling or dilution also affects to UHCs and CO formation by quenching the reaction. For the efforts to reduce emissions, the importance of thermal management of combustor is more emphasized.

Realizing the highest efficiency and output power impacts combustor design conditions. Optimized cooling design of the combustor liner benefits both durability and emission. However, it is impossible without understanding the reacting flow and the associated heat transfer. Accurate characterization of flame side heat transfer is not fully investigated yet. The objective of the present research work is to improve our understanding of flow and heat transfer inside combustor, and to provide insights to the next-generation gas turbine combustor designs.

1.2.3 Conventional Combustor Configuration

Gas turbine generates power from the chemical energy contained in the fuel. Combustor, also called as burner or combustion chamber is a component of gas turbine which converts the chemical energy to thermal energy by process of chemical reaction. Because it directly contacts the reacting flow, the combustor system is exposed to the highest temperature. The pressure condition is also very high, since it is located between compressor and turbine. A diagram of gas turbine configuration shows the location of combustor in Figure 2.

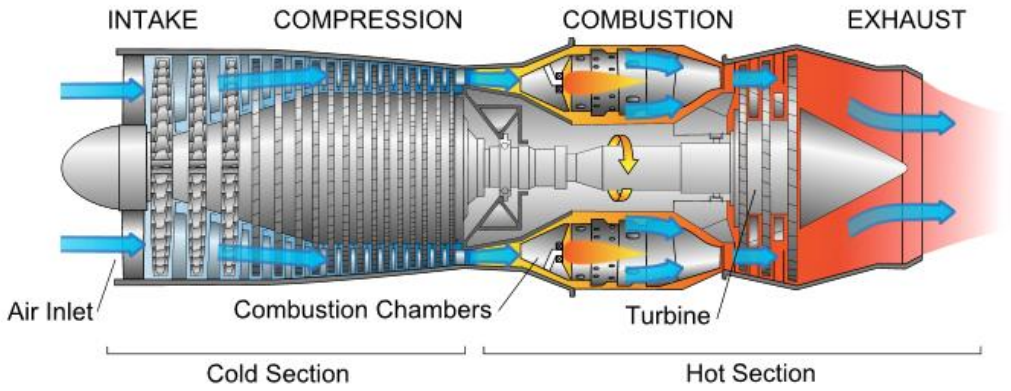

Figure 2. Diagram of a gas turbine engine showing the compressor, combustor, and turbine. Diagram by Jeff Dahl [13].

Fundamentals of gas turbine combustor are available in studies by Lefebvre and Ballal [14] and Mellor [15]. Details of most of the considerations for gas turbine design are given in their works comprehensively. Figure 3 and Figure 4 show a design of conventional combustor and section of a conventional combustor (Rolls-Royce Nene turbojet) of 1940s [16].

Combustor liner or flame tube is contained inside a high pressure casing. Diffuser at the combustor inlet reduces the flow velocity to present stable air flow to the compressor. The flow recovers the dynamic pressure which enhances overall efficiency due to the diffuser. The snout separates the primary and the secondary air. Secondary air is used for cooling and dilution. Swirler and fuel nozzle are mounted on the dome of the combustor. Swirl flow generation is discussed more in the later part of this chapter. Primary zone holes on the liner are strategically placed to stabilize the flame by flow recirculation. Dilution holes introduces more air to adjust the temperature of the hot gas to be allowable for the nozzle guide vanes in the turbine section.

Film cooling holes of slots are to prevent the liner from overheating and related failure by forming a layer of coolant air on the flame side of the liner.

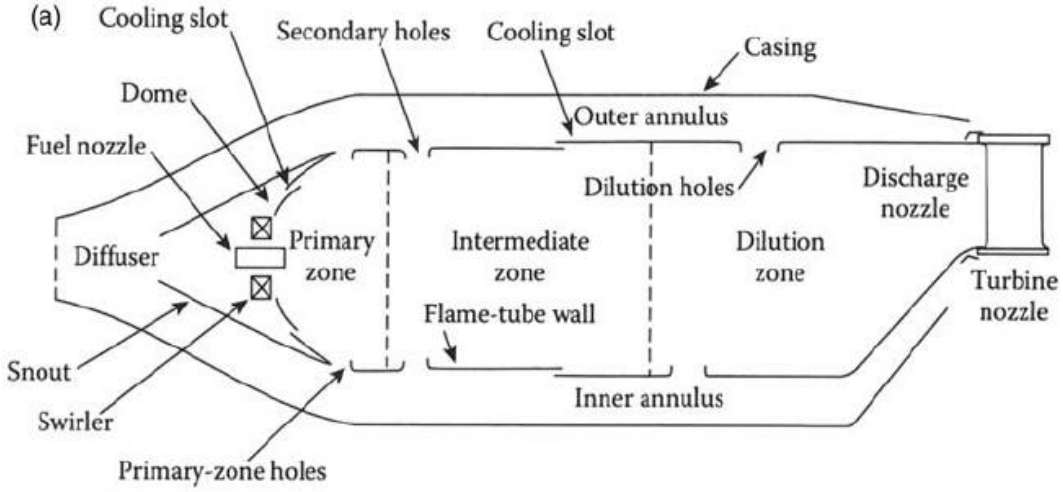

Figure 3. Main components of a conventional combustor [13]

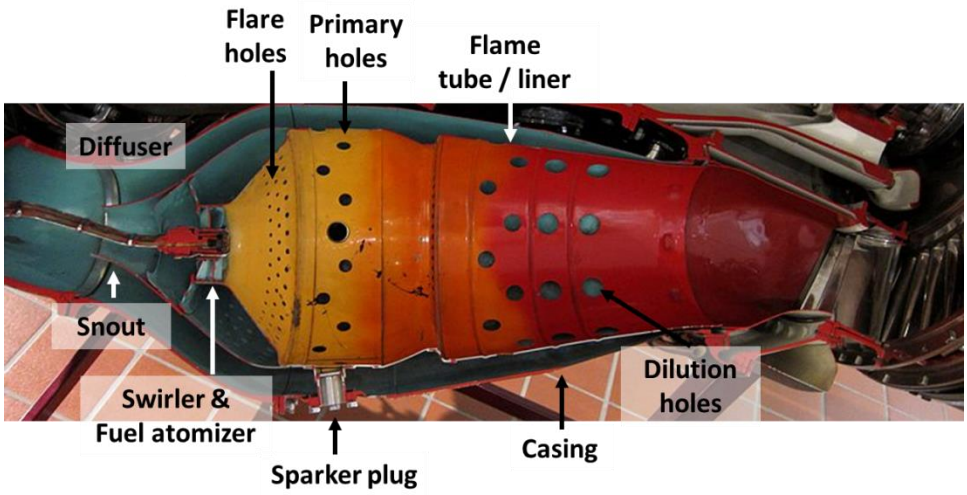

Figure 4. Sectioned Rolls-Royce Nene Turbojet combustor [16].

The inner space of the combustor is divided into three zones. The primary zone is where fuel is mixed with air and ignites. The most of chemical reaction and heat release occurs near the stabilized flame in this zone. More air is introduced at the intermediate (secondary) zone to minimize CO and UHCs. The secondary zone increases the residence time and improves combustion efficiency, especially for early combustors with diffusion flame. Dilution zone is the final region of combustor, where the exhaust gases are mixed with air and tailored to have

desired pattern factor (measure of temperature profile uniformity). Finally, a transition piece connects the combustor to turbine section.

1.2.4 Modern DLE Combustor

Two key features of modern combustors for stationary gas turbines are premixing and reduced cooling. For traditional combustors, diffusion flame was preferred to maintain high stability, and the coolant rate for film cooling and dilution was higher. To enhance efficiency, emission and durability, researchers focused on achieving lower flame temperature and more primary air, by pioneering dry low emission (DLE) technology. The term 'dry' is used opposed to 'wet', because water injection was widely used for early gas turbines to reduce flame temperature and minimize NO_x emission. Stringent requirements drove the development of new DLE technology. The Environmental Protection Agency (EPA) in the United States limits the emission to 15 ppm at 15% O2 for large stationary gas turbines firing natural gas [17]. The pollution management became a top priority for this reason.

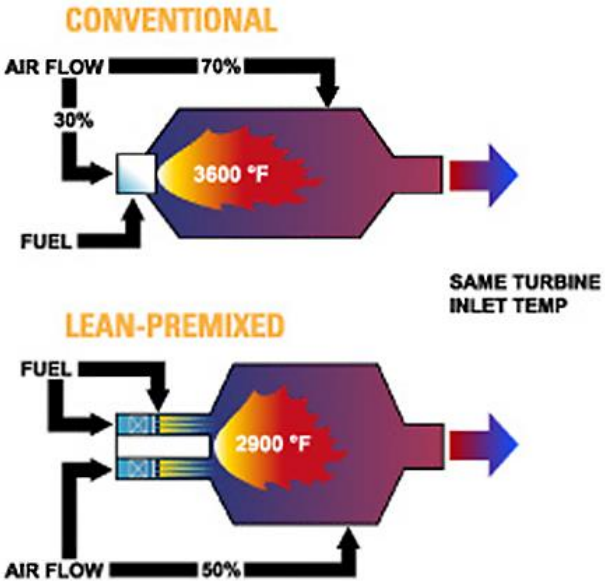

Figure 5. Air distribution in a conventional and a low emission combustor [18].

Solar Turbines Inc. led the early innovations of DLE, featuring their SoLoNOx fuel nozzles. A diagram in Figure 5 shows the difference in the distribution of the primary and

secondary air flows. Modern lean premixed nozzles require less cooling air and they supply more air through primary path for the same turbine inlet temperatures condition. Reduced amount of coolant air flow demands improved thermal management technology.

Figure 6 compares the designs of conventional and SoLoNOx combustor. The SoLoNox combustor features no film cooling on the liner. Instead, coolant air from back side of the dome splash plate (heat shield) exits along the liner near the dome plate. Film cooling and dilution holes are present only to the end of the combustion chamber. The absence the holes in the intermediate zone is contrasting aspect from the conventional combustor.

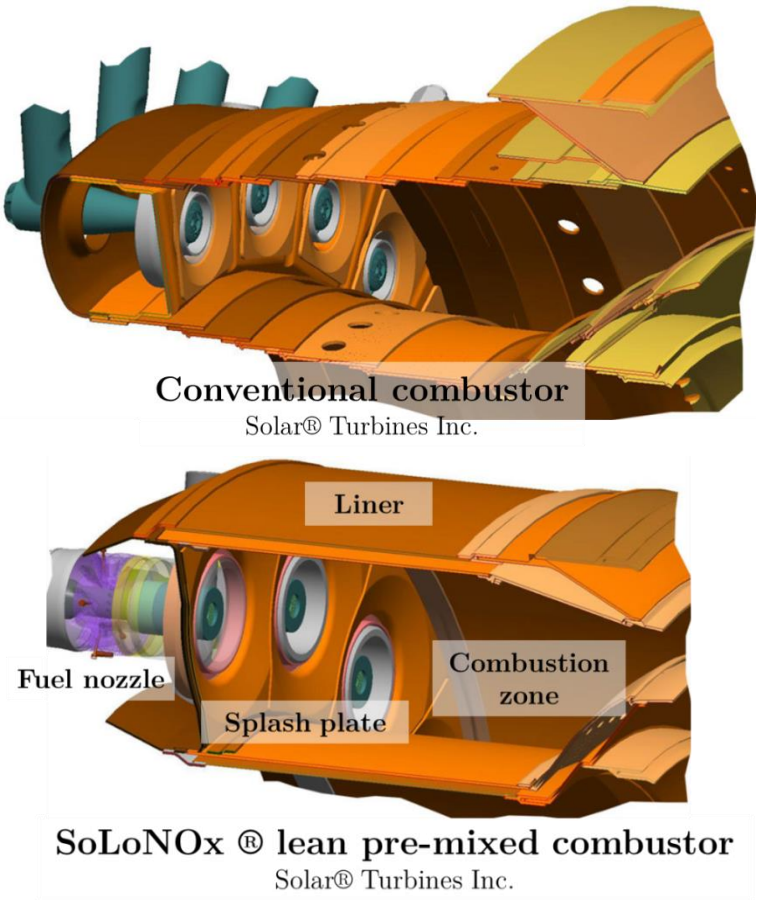

Figure 6. Comparison between a conventional and a modern SoLoNOx ® lean pre-mixed combustor design from Solar Turbines Incorporated [19].

1.3 Background of Flow Field and Heat Transfer Research

1.3.1 Combustor Flow Field

Swirl is tangential rotation of the flow, which is generated by a swirl fuel nozzle before it enters into the combustion chamber. The swirling jet forms flow features for flame stability in the primary zone of the combustor. Typical flow structure in the mean velocity is shown in Figure 7 [20]. Noticeable features of the flow are the location of shear layers and recirculation zones. The inner recirculation zone (IRZ, CRZ, central recirculation zone) brings hot combustion products back to the swirling jet exiting the nozzle, igniting the fresh mixture. An important coherent flow structures are observed at the inner shear layers that enhance the mixing between the swirling jet exiting the fuel nozzle and the recirculated gases. It is important to understand the behavior of the flow particularly for interactions between swirl jet and recirculating flow at the inner shear layer.

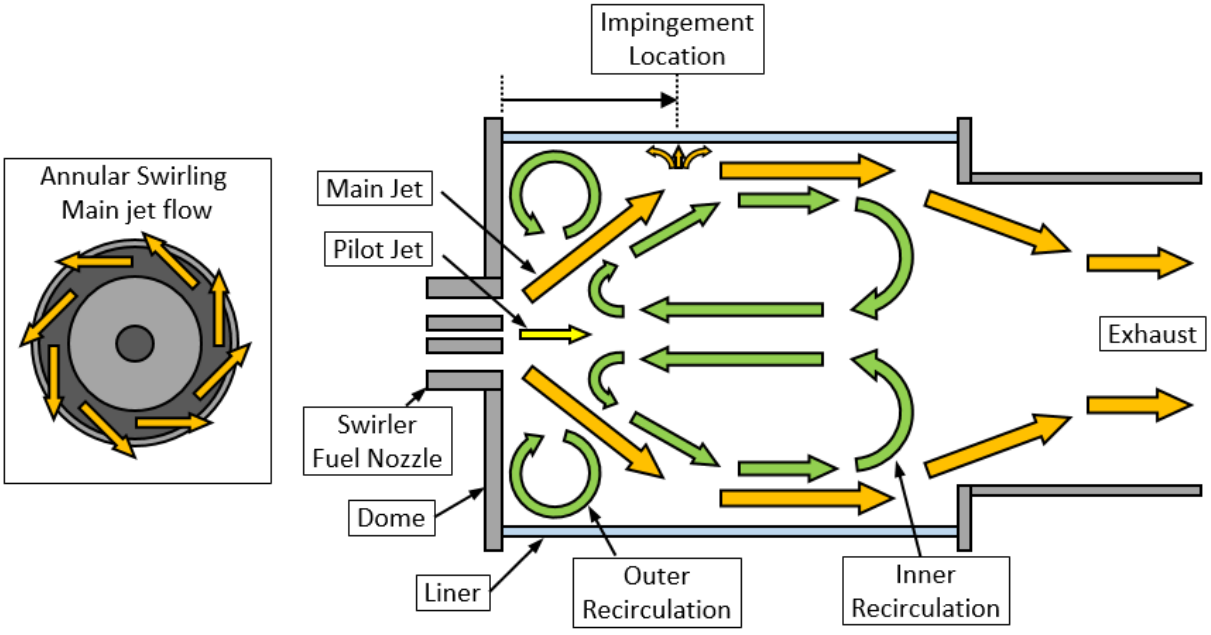

Figure 7. Schematic of typical flow structure inside a swirl combustor

Due to the existence of IRZ, the swirl type burner does not need a blunt body flame holder for stabilization. Heat loss at the blunt body is curtailed with the swirl fuel nozzle, and cooling design can be simplified. Extended residence time due to recirculation shortens the total length of combustor, enhancing the overall efficiency [14].

Researchers has studied the swirling flows within combustors for more than 50 years. Current works focus on understanding the vortex breakdown phenomena which results the central recirculation. Comprehensive reviews are available on combustion in swirling flows by Lilley [21], Beér and Chigier [22], Syred and Beér [23], and Gupta et al. [24]. Continued research works contributed to the characteristics of swirling flows including IRZ, axial pressure recovery of swirling jet, and the trigger of vortex breakdown [20].

A balance equation of centrifugal force and pressure force transmitted from the wall can be applied for a can combustor. The equation for quasi-cylindrical flow at steady state laminar flow is given by Equation 4 [25, 26].

$$\frac{\partial P}{\partial r} = \frac{\rho w^2}{r} \tag{4}$$

Tangential velocity component is w, and radial location from central axis is r. Integration along radial axis yields Equation 5 [25].

$$\frac{\partial P}{\partial x}_{r=0} \simeq \frac{\partial P}{\partial x}_{r=R} - \frac{\partial}{\partial x}\int_0^R \frac{\rho w^2}{r} dr \tag{5}$$

If pressure gradient along x axis is always negative i.e., $\frac{\partial P}{\partial x} < 0$, the fluid will be accelerated to the positive direction until it balances with pressure loss such as viscous force. Flow reversal is possible only if the pressure gradient term is positive. The axial difference of pressure at the center is smaller than that at the wall by the contribution of centrifugal force. During the expansion at the nozzle, tangential velocity of the flow decreases due to conservation of angular momentum. Accordingly, the last term decreases and reaches negative value, as $\frac{\partial}{\partial x}\int_0^R \frac{\rho w^2}{r} dr < 0$. It causes adverse pressure gradient on the flow near the axis with $\frac{\partial P}{\partial x}_{r=0} > 0$. This effect with sufficiently high initial tangential velocity can overcome the axial momentum. After a triggering event, a vortex breakdown bubble is created by this mechanism, forming a inner recirculation zone in the combustor.

Recent works on combustor flow field focused on unsteady behavior and combustion instabilities by Lieuwen [27], Lucca-Negro and O'Doherty [28], Syred [29], and Huang and

Yang. [20]. Various types of vortex breakdown and periodic oscillations in the flow such as precessing vortex core (PVC) and the axial-radial shedding vortices at the combustor exit have been identified in detail. The size and characteristics of IRZ and PVC are determined by the flow properties and velocity profiles at the inlet [25,30,31]. Experimental and theoretical demonstration of inlet radial velocity profile on the onset of flow reversal is reported by Hallet and Toews [32]. Size of recirculation zones increase when central hub or a diverging fuel nozzle were used [21]. Seminal work by Faler and Leibovich [33] on flow visualizations explained the dependence of vortex breakdown on Reynolds numbers up to 10000 with respect to the nozzle diameter. At the highest tested Reynolds numbers, only axisymmetric and spiral vortex breakdown modes were observed. With increased Reynolds number, an upstream shift of the recirculation bubble was identified. The swirl number (S) is a frequently used parameter to represent the strength of swirl. It ratio of tangential momentum (G_ϕ) to axial momentum (G_x) in the axial fluxes with a proportional factor inverse of combustor diameter (R) as defined by Equation 6.

$$S = \frac{G_\phi}{R\, G_X} \tag{6}$$

The swirl number is used in many procedures of combustor designs. Existence of vortex breakdown is the first one determined by swirl number. Its threshold value to ensure vortex breakdown was reported as 0.6-0.7 by Syred [29]. The flow structures are affected by the swirl number. Increase in the swirl number leads to a longer recirculation zone and upstream shift of the bubble location [25]. The swirl number also governs the mass flow of recirculation, which is important for flame stability.

Terhaar and coauthor recently reported about formation and characteristics of vortex breakdown and the effect of inlet flow profile modification using axial injection [34]. The triggering of a conical vortex breakdown was identified at high axial flow injection rate. Carmack et al. showed the differences between axial and radial swirl nozzles for industrial gas turbines by investigation on flow characteristics [35]. Strakey and Yip compared the instantaneous flow and the corresponding time-averaged flow field for non-reacting condition.

PVC elements were identified using a slot swirler with a swirl number of 1.17 [36]. However, their works did not cover reacting conditions.

Comparison of reacting and non-reacting flows was done by Ji and Gore [37]. Instantaneous and time averaged flow fields for unconfined swirl flame were presented with a swirl number of 2.4. The results provided insight to the changes between non-reacting and reacting flows and the importance of instantaneous flow. Larger turbulent kinetic energy and smaller eddy length scales in reacting flow were their main observations.

1.3.2 Combustor Heat Transfer

The first experimental characterization of the heat transfer on the combustor liner was conducted by Lefebvre et al [13,38]. The radiative part of heat transfer is well analyzed by Viskanta [39,40] and Lefebvre [41]. Regarding convective heat transfer, Lefebvre and Ballal mentioned that "the uncertainties regarding the airflow pattern, the state of the boundary layer development, and the effective gas temperature make the choice of a realistic model almost arbitrary" [13]. They estimated the convective heat transfer within combustor using a model of fully developed turbulent pipe flow as in Equation 7. The similar relation can be assumed to be applied for combustor without film cooling, but selecting reference mass flow, velocity, and temperature is difficult for the calculation.

$$Q_C'' = 0.02\ \mathrm{Re}_{C,\infty}{}^{0.8}\ \frac{k_\infty}{D_C}\ (T_\infty - T_W) \tag{7}$$

The authors suggested replacing the coefficient 0.02 to 0.0017 accounting the reduced near wall gas temperature. As an example, the primary zone mass flow was found to be 26% of the combustor inlet mass flow [38]. The information of flow distribution and recirculated flows was critical for this approach for reliable analysis results. Lefebvre and Herbert validated the energy balance model accounting for internal and external liner convection and radiation [38]. The results agreed well with experimental engine wall temperatures for different operating conditions. This provided valuable information for the engineers of gas turbine combustor for

the early designs. However the distributions such as peak heat load and profile on the wall were not discussed in their work.

Convective heat transfer approximately equals to Dittus-Boelter heat transfer correlation (Equation 8) at Pr ≈ 0.706. The gas properties are typically evaluated at the local film temperature, and exponent n_T is set to 0.4 for $T_W > T_\infty$ and 0.3 for $T_W < T_\infty$.

$$\mathrm{Nu}_{Dittus-Boelter} = 0.023\mathrm{Re}_{C,f}^{0.8}\mathrm{Pr}_f^{n_T} \tag{8}$$

Dittus-Boelter equation is accurate when wall to gas temperature is less than 56 K in the range 10000 < Re < 120000. It does not account for the temperature dependent gas properties [42, 43]. After the seminal works, understanding of turbulent flow heat transfer correlations have improved significantly including the heat transfer with more complicated flow features which are found in modern gas turbine combustors [44-47]. Dellenback et al. worked on the experimental study of the heat transfer with swirls flows and sudden expansions [48]. The study identified details on the effects of swirl and mass flow rates for Re < 51000. The increase in the swirl number showed higher heat transfer to the wall, and the location of peak heat transfer appeared consistently upstream of the flow reattachment. Similar heat transfer characteristic about reattachment and outer recirculation was studied by Baughn et al. in sudden expansion without swirl [49]. A study on turbulent decaying swirl flow without sudden expansion have been carried out to study the effect of swirl number and swirl generator configuration [50].

Cooling technologies in combustor have been extensively studied, but the heat transfer still remains not fully characterized. Ekkad et al presented convective heat transfer for can and annular combustors, using simulated industrial swirl fuel nozzles [35, 51-54]. They covered numerical simulation and experimental studies using particle image velocimetry (PIV). Patil et al. identified higher Nusselt numbers than Dittus-Boelter relation, which implies underestimation of convective heat loads. Recently, Andereini et al and Mazzei et al conducted experimental and computational studies on heat transfer and flow field with non-reacting flows using a model combustor with three swirl nozzles [55, 56]. The effects of neighboring nozzles and the film cooling on convective heat transfer were discussed from PIV results, which provided insight to the interaction between flows from multiple nozzles.

Combustor engineers optimize the combustor design and its cooling schemes based on correlations and semi-empirical models, with various numerical and experimental works [13, 57-59]. To enhance the cooling design of modern DLE combustors, detailed thermal load on the liner should be accurately analyzed. Particularly, the convective heat transfer has to be emphasized due to the complexity. Heat loads associated with reacting swirl flow in the primary zone is the most challenging area of research.

1.3.3 High Temperature Heat Transfer Measurement

Numerical models are widely used in industry to evaluate heat transfer, with supplementary experimental liner wall temperature measurements for validation purposes [10, 58-60]. Conventional methods for liner temperature were embedded thermocouples and thermal paints [57, 58]. Thermocouples measures accurate temperatures with limited spatial distribution information, and thermal paints provide temperature distribution with semi-quantitative estimation. Commonly the thermal paint technique utilizes thermocouples as a reference. Due to the limitation of time response of thermocouple, capturing transient behavior is difficult. Therefore, high thermal stress during ignition or shut down cannot be accurately estimated, which may impact combustor durability.

Heat flux measurement techniques for reacting conditions is available in other communities. Thermographic phosphor (TP) technique is can be a candidate to characterize heat transfer in reacting environment [61-65]. Studies on afterburners, internal combustion engines, and fire applications were presented by Aldén et al [61]. TP needs to be carefully selected for proper temperature range. The available temperature range of YAG:Dy is suitable for gas turbine combustor studies. Also, the availability of TP material and complexity of the setup can be barriers for the implementation. Sensor probe or gauge are used in internal combustion engines for heat flux measurements [66-68]. This technique offers good temporal resolution, but the measurement is an intrusive method. Besides, the temperature range of the sensor is often limited to about 1000 °C [69].

Common heat flux measurement techniques used in the fire community are calorimeters and Schmidt-Boelter heat flux sensors [70]. Using the two sensors in combination can determine convective and radiative heat transfer from flames [69]. One method is differentiating the

amount of radiative component using two thermopiles with different emissivities [71]. Heat flux sensor measurement removing the effect of convective heat transfer with windows can be another method [72]. Infrared thermography was used for total heat flux and measurement to overcome the spatial limitation by Rippe and Lattimer [73]. The radiative and convective components were measured as well. Hindasageri et al. used infrared thermographic camera to monitor the temperature and total heat flux from impinging flames to quartz glass plate [74]. However, the use of correlations for convective heat transfer which is still challenging for complex geometries.

Studies on flame impingement are available in the open literature for wide variety of applications. A review written by Baukal and Gebhart summarized the experimental works [75-77]. Earlier research was reviewed by Viskanta [78]. Those reviews pointed out the importance of flame impingement for convective heat transfer, and the relative contribution of radiative and convective components are one of the concern. Baukal and Gebhart quantified the contributions of radiation of non-luminous flame and thermochemical heat release [79]. The radiative heat transfer accounted for 9.8% in their results. A more recent review was done by Chander and Ray [80]. The type of radiation affects the contributions of heat flux components. Luminous radiation of soot particles in the flame is known to contribute enormously [13, 81]. Non-luminous radiation due to H_2O and CO_2 yields small contribution on the contrary [82]. A study on the radiative heat transfer by Keramida et al simulated radiative heat transfer in a furnace and compared it with experimental temperature measurements [83]. Radiation component is shown to be necessary for accurate modeling of heat transfer in the furnace.

Liner wall heat flux measurement technique using infrared camera for reacting combustor was developed recently by David Gomez-Ramirez [84]. The author demonstrated the technique with non-reacting flow and reacting flow. The tests covered a single case of reacting condition, but the effect of combustor operating condition was not fully characterized.

1.4 PROJECT OBJECTIVES

The heat load under reacting condition is important for thermal management of gas turbine combustor, however, the available experimental data is not sufficient. The objective of this work is to characterize the flow and heat transfer for reacting flows in a model combustor. A specific

overall goal is to better understand thermal interaction between reacting flow and liner wall. Measuring and identifying the flow features and properties are the essential topics, since the convective heat transfer is closely related to the flow. As a strategic approach at current stage, the scope of this research is set to investigate various aspects of the flow properties and wall heat transfer by implementing novel diagnostic methods on the recently built optical combustor test rig.

The project includes four main topics: 1) velocity field measurement for different reacting conditions, 2) flow temperature measurement, 3) infrared measurement of reacting flows, and 4) liner wall heat transfer measurement. The first and the last topics used the same technique as the previously developed methodology. Second topic used conventional technique for flow temperature measurement. Third topic is an assessment of flow visualization technique using infrared thermographic camera.

The tests are performed under realistic condition as much as possible. The test rig is equipped with an industrial swirl fuel nozzle SoLoNOx, which is made by Solar Turbines. The nozzle provided realistic reacting flow conditions to simulate DLE combustor. The design of the test rig was to achieve realistic testing conditions for industrial combustor components and flexibility for potential broadening of the study area. This facility provided flow rates and flow properties closer to real engine operating conditions, compared to scaled research combustors. Atmospheric pressure condition is a limitation for the tests, since pressurized setup could not be built with the given amount of time and budgets.

CHAPTER 2. COMBUSTOR TEST RIG

This chapter describes the combustor test rig. A model combustor rig was used throughout the work. Features and capabilities are mainly discussed. Further details on the design of this research combustor including development process, function, structure and performance can be found in [85].

2.1 OPTICAL MODEL COMBUSTOR RIG

The optical combustor rig is housed at the Advanced Power and Propulsion Laboratory (APPL) at Virginia Tech. Figure 8 shows the schematic of the test rig. The experiments were performed on the model combustor test rig. The design of the facility targeted reacting combustor study with industrial swirl nozzle. Capability of elevated pressure was a part of the design as well. However, the high pressure configuration were not built completely due to time and budget limit. The experiments in this study were performed at atmospheric pressure.

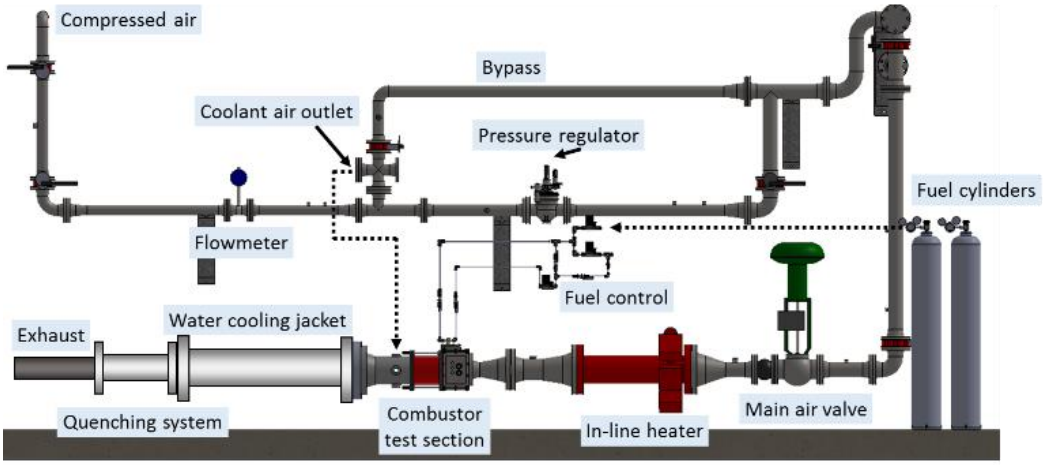

Figure 8. Schematic of optical combustor test rig

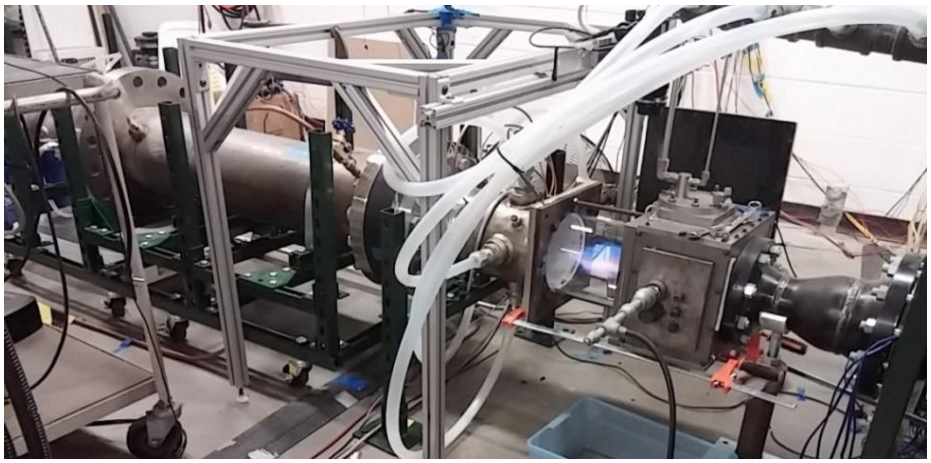

Figure 9. Photograph of the optical combustor rig with a pilot flame inside.

2.2 RIG CONTROL AND MONITORING

Compressed air was supplied to the settling chamber from a compressor through pipe connections with maximum capacity of 1.27 kg/s (2.8 lbm/s) mass flow rate. The atmospheric pressure was ~0.93 atm at 630 m altitude of Blacksburg, and inlet air was ambient temperature (~20°C) when it is not preheated. Compressed air supplied at 160 psig was regulated to 15-30 psi for precise control with a control valve. Control valves and rig monitoring was done with an integrated LabVIEW application.

The uncertainty of the air flow rate is ~2 %. The pressure of the test section was at atmospheric (~0.93 atm at 630 m altitude of Blacksburg, VA). An in-line heater provides preheated inlet air. Typical inlet air temperature without preheating was ~23°C. For main air control valve, PID control was implemented to compensate compressed air inflow fluctuations.

Two mass flow controllers from Alicat Scientific controlled fuel lines. The integrated LabVIEW application was connected to the controllers through RS-232 interfaces. Main fuel controller has 100 ms response time, 0.2% repeatability, and 200:1 turndown ratio. Calculated overall uncertainty of total fuel flow rate was ~ 2.8% for typical fuel flow rates. Propane was used as fuel in this work.

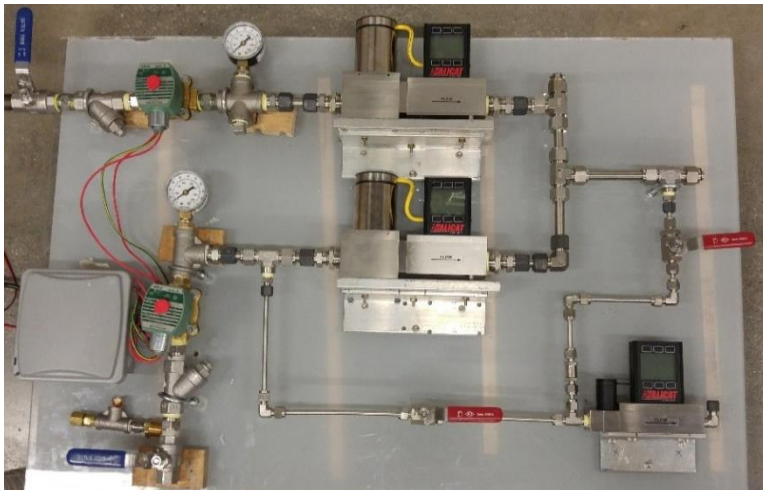

Figure 10. Photograph of assembled fuel supply system.

2.2 TEST SECTION

The rig is designed with the flexibility to install different combustor components and test them on the rig. Modular design of the test section provides the versatility to be modified for different test parts such as fuel nozzles, dome plates, liners, or transition pieces.

The test section is a can type model combustor made of transparent glass to ensure visibility for both regular visual cameras and infrared cameras. The design of test section is shown in Figure 11. The primary zone of test section is made of an air-cooled flat dome plate and a 4 mm thick tubular quartz glass (fused silica, GE 214) liner. The liner has an axially symmetric tubular shape which allows 360-degree optical access perpendicular to the axis. Optical access from the sides is available for full primary zone of the combustor.

A settling chamber (plenum chamber) is where the dome and fuel nozzle is installed upstream of the combustor primary zone. The settling chamber was designed to allow for easy assembly. The material used for manufacturing the settling chamber is SA-516 carbon steel that can withstand temperatures of 1000°F (810 K) and 850°F (727 K).

The mixture of gas reacted in the primary zone then flows through a transition piece. A straight metallic transition piece is connected after the quartz liner, and coolant air is supplied to the outside periphery of the transition piece. Combustion product and the coolant air were mixed after the exit of the combustor. The exhaust flow safely exits the test section to exhaust pipe connections.

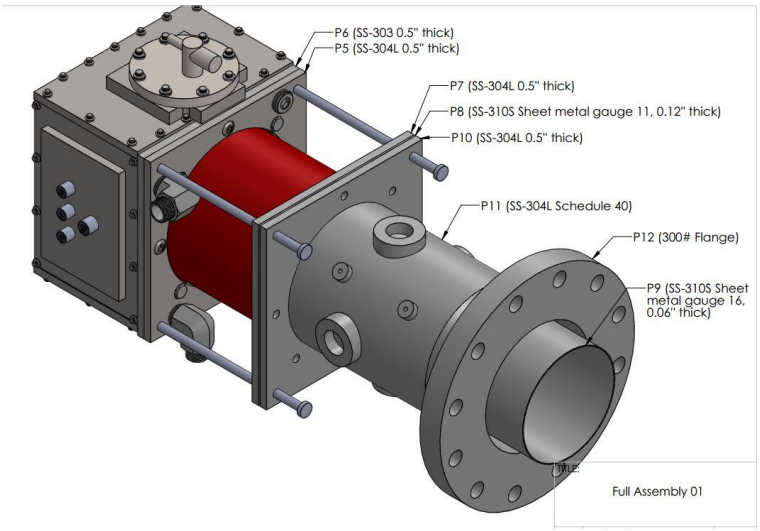

Figure 11. Full Assembly of the Test Section

Water cooled jacketed pipe and quenching unit further cools down the mixture gas from the transition piece exit. For typical reacting operations, gas temperature in the exhaust was 200-500 °C depending on the flame temperature and the rate of coolant air. Water circulation system was installed for the cooling jacket and quenching system. About 1.7 gallons per minute of water circulated the water, and small portion of water was sprayed in the quenching unit. Temperature of the water thank was monitored with a thermocouple. Cold water was supplied to compensate the used amount in the quenching unit, and to reduce the temperature.

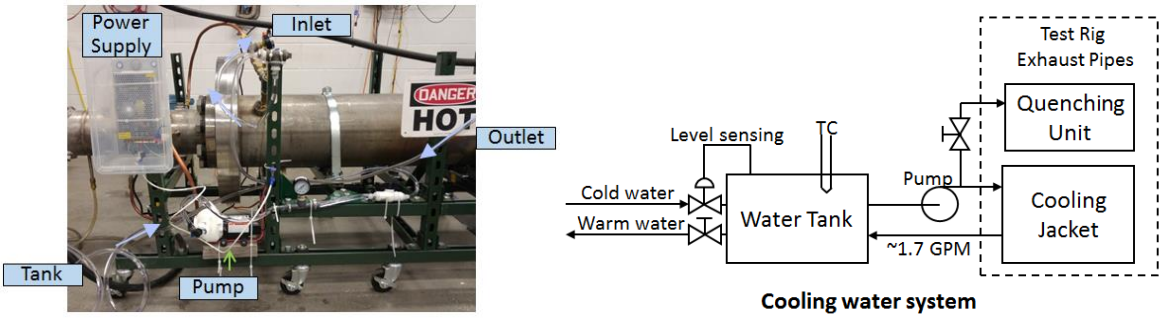

Figure 12. Independent cooling water circulation

Figure 13. Photograph of dome plate installed on the settling chamber.

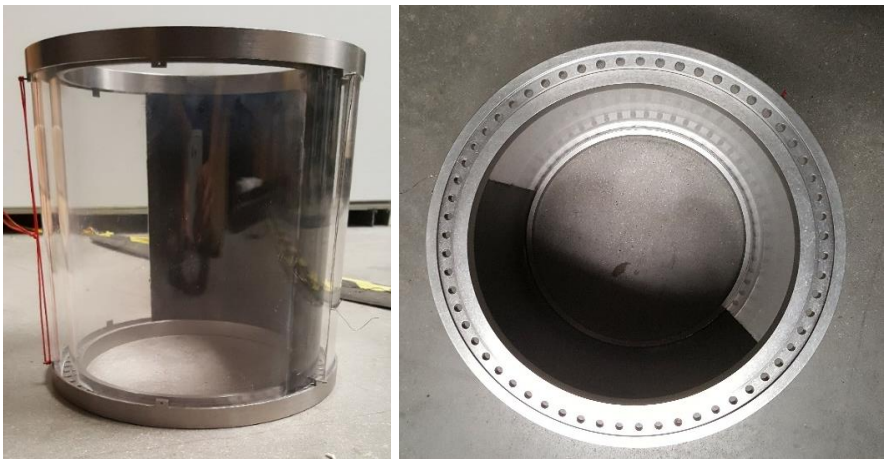

Figure 14. Double liner configuration with coolant holes for liner cooling

The test section has capability to control forced coolant airflow on the combustor liner. Double liner configuration is made with two glass tubes with different diameter, and two metal pieces (add-on piece) to secure the tubes together. The liner assembly can be installed between the dome plate assembly and transition piece assembly. There are holes on the add-on piece for coolant airflow, which is supplied from coolant air pipeline. The liner coolant air control was not applied in this work, due to lack of additional control valve. Forced cooling and different liner geometry, cooling schemes with metal liner are left as future works.

2.3 SWIRL FUEL NOZZLE

The research combustor is equipped with a lean premixed swirl fuel nozzle made by Solar Turbines Inc. Figure 16 is a schematic of the industrial fuel nozzle installed on the rig. Methane or propane was used as fuel. Air and fuel are premixed in the fuel nozzle before it enters the test section.

There are two passages through the nozzle, an annular main nozzle and a circular pilot nozzle at the center. As air passes through annular main nozzle, vanes generate swirl in the flow. The axial swirl vanes inside the nozzle generates swirling flow after the flow entered into the test section, and an annular main jet was formed at the primary zone in a cone shape. The swirl flow from the main nozzle stabilizes a conical main flame with inner recirculation and outer recirculation flows. A pilot flame is at the center ensures flame stability. Air and fuel flow at the pilot is approximately 2 % of the total flow. Since the design of the swirl fuel nozzle is property of Solar Turbines Inc., the detailed dimensions are not discussed in this dissertation.

Figure 15. Swirl fuel nozzle (SoLoNOx) designed by Solar Turbines Inc.

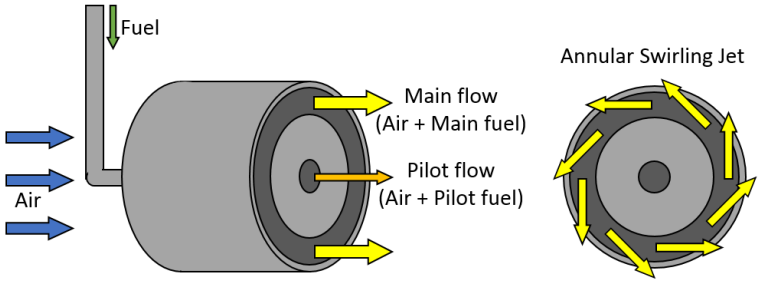

Figure 16. Schematic of premixing axial swirl fuel nozzle installed in the combustor rig.

CHAPTER 3. PIV FLOW FIELD MEASUREMENT

In this chapter, flow details for reacting flow conditions in a model combustor are provided. Gas turbine combustor improvements require accurate measurement and prediction of reacting flows. However, flow measurements inside combustors under reacting conditions is a very serious challenge. Understanding thermal energy transfer requires the study of flow characteristics and associated heat load. Experimental investigations are presented on the effects of combustor operating conditions on the reacting flow in an optical single can combustor. The swirling flow was generated by an industrial lean pre-mixed, axial swirl fuel nozzle.

3.1 PIV MEASUREMENT IN REACTING FLOWS

The first PIV measurement used methane fuel. Effects of equivalence ratio, pilot split ratio, and air mass flow rates on the flow features were tested.

3.1.1 Background

Flow velocities within combustors have been studied since the early 1980s (e.g., the seminal work of Heitor [86] and the reviews of Lilley [21] and Syred [23]). The majority of those early investigations focused on diffusion flames within combustors. The main concern for early combustors was stability, contrary to modern burners which have shifted their focus to improve emissions. This has been accomplished with the use of lean premixed fuel nozzles, primarily used in land based engines where stability can be partially sacrificed (and where the fluctuations in operating conditions can be more easily controlled). The use of modern lean fuel-premixed nozzles and the goal to reduce emissions has brought important new challenges to combustor design. There are few studies that have focused on detailed measurements for these type of combustors.

The objective of this work is to examine the reacting flow fields produced by a lean-premixed fuel nozzle at different combustor operation conditions including variations in equivalence ratios, pilot fuel split ratios, and Reynolds numbers (mass flow rate). Since a significant portion of the heat load on the combustor liner is transferred by convection,

understanding the velocity fields in the reacting flow is crucial to enhance cooling techniques on combustor components. Investigating the effect of these parameters on the reacting flow structures and non-dimensional flow properties is the goal of this work, with a special focus on flame jet impingement locations as these determine the regions of highest convective heat transfer.

The recent work by Weigand et al. [87] reported measurements of reacting flow with laser Doppler velocimetry (LDV), OH planar laser induced fluorescence (PLIF), and laser Raman scattering in a laboratory scale model combustor, and concluded that flame structures and reacting flow fields are very similar at different combustion regimes. Stopper et al. [88] used a commercial swirl burner in a high pressure test rig, and measured reacting flows with similar methods. Stopper et al. found that reacting flow behavior is not sensitive to variation of combustor parameters tested (4 cases at different pressures, mass flow rates). Even though, effects of other important combustor operating parameters (equivalence ratio, pilot fuel split ratio, etc) remained unrevealed. The work of Ji and Gore [37] focused on the comparison between a non-reacting and reacting case for a lean premixed fuel nozzle, but the extent of their observation was limited by their optical access. Moreover, the work of Ji and Gore was performed for a single reacting condition and in an effectively open condition (unconfined), there were no liner walls in their burner which can cause important changes in the fluid dynamics.

The present work expands on this by studying several combustor operating conditions and using an optical liner with full optical access to confine the flame. The burner was also designed to be as simple as possible to facilitate the validation of computational models. Gomez et al. [89] performed PIV flow field measurements in non-reacting (isothermal) conditions in the same rig, focusing on impingement locations at the liner wall. For the non-reacting flow, self-similar velocity fields were measured at different mass flow conditions. The present work further focused on the flame jet impingement locations of reacting flows under different operating conditions, given their relevance in determining the location of peak heat loads on the liner wall. In the current study, the main accomplishments include non-dimensional analysis of the flow fields, and quantitative determination and comparison of the swirl impingement locations for different combustion operating variables.

Recent advances in optical heat transfer measurement using infrared thermographic camera was demonstrated by Gomez et al. [84, 90]. Outer wall and inner wall temperature

distributions were measured simultaneously on a partially painted black coating of a quartz glass liner. The same method was applied for multiple cases of reacting flows in this work to compare heat load distribution with the flow field features.

3.1.2 Basic Principle of PIV Measurement

Particle image velocimetry (PIV) is a flow visualization technique, which is partially intrusive. The basic principle is that two images were compared with a specific time delay, and then the difference between the images is analyzed to obtain velocity vectors from shift of particle locations. Planar PIV is the most common setup which uses a single camera. Small sized particles submerged in the flow in motion are illuminated by a laser sheet. The camera captures the particle images in the measurement plane which coincide with the laser sheet. Cross-correlation and accompanied calculations, a 2D velocity vectors are measured. Figure 17 shows procedures of PIV measurement.

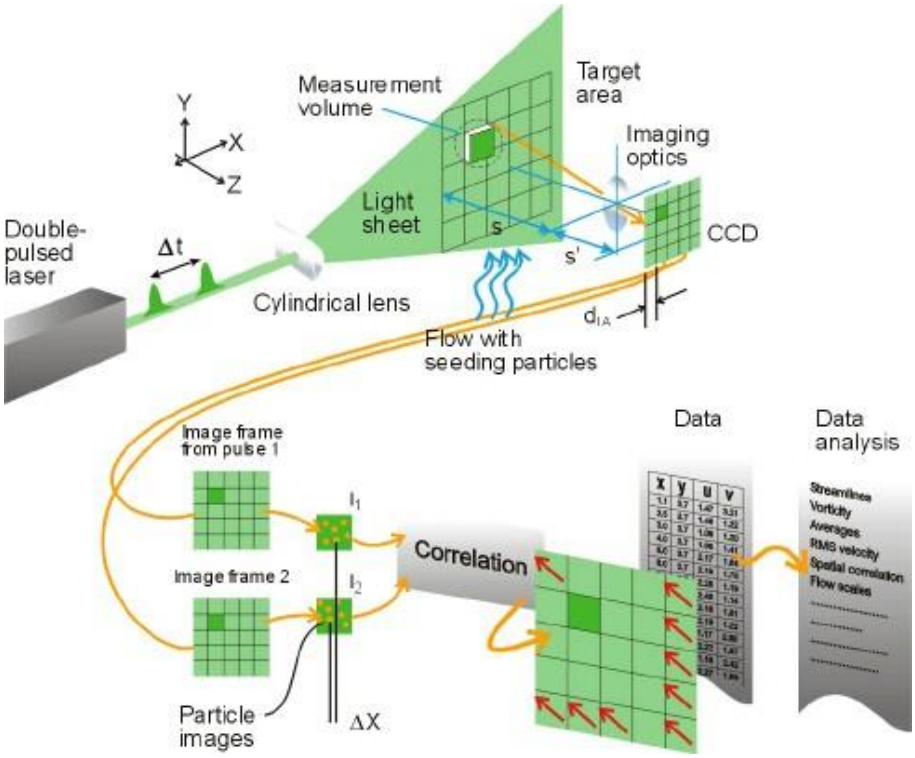

Figure 17. Principle of particle image velocimetry [91]

First, pair of images are obtained with a time delay Δt. Cross-correlation is performed in each interrogation area as shown in Equation 9. Peak of the cross-correlation is searched followed by subpixel interpolation. Finally, velocity vector is obtained in each interrogation area.

$$R_{II}(x,y) = \sum_{i=-K}^{K} \sum_{j=-L}^{L} I(i,j)I'(i+x,\, j+y) \tag{9}$$

3.1.3 Experimental Setup

The PIV measurement setup comprises of a light source and an image capturing device. Figure 18 is a schematic of the PIV system installed at the combustor rig. A double pulse Nd:YAG laser (Nano-L-135-15 double cavity Q-switched) with maximum pulse energy of 140 mJ at 532 nm and a PIV camera (FlowSense 4M MkII) were used. An optical band pass filter (Omega Optical 532BP10, 10 nm bandwidth at 532 nm) and a neutral density filter (ND 8) were attached in front of the 76 mm lens system of the camera. The control of the measurement system and data acquisition was performed by Dantec Dynamic Studio software. The collected data were pairs of images with a 2048×2048 resolution.

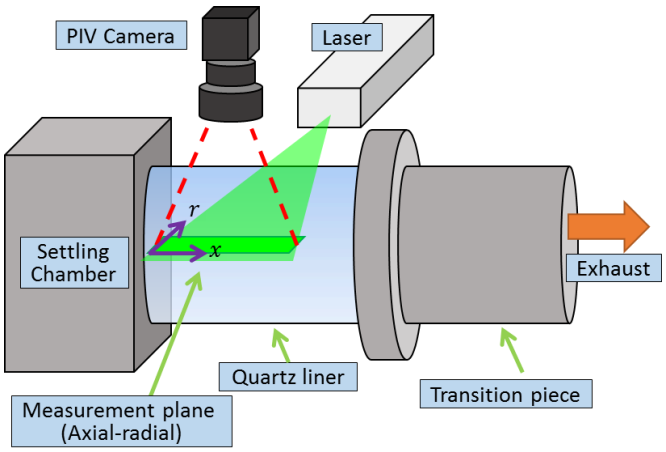

Figure 18. Schematic of PIV flow field measurement at the model combustor rig

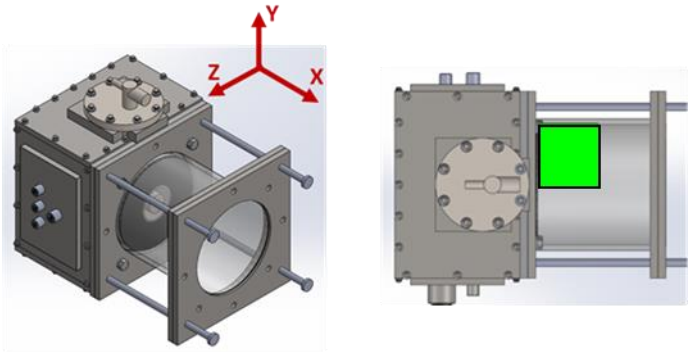

Figure 19. Region of interest for PIV measurement

For seeding, a cyclone seeder was designed, consisting of a cylinder sealed at both ends with an inlet port on the side surface (tangential air entry), and an outlet port on the top surface. The particles at the bottom are agitated and carried by the air flowing from the inlet, thus providing the seeding for the PIV experiments. The inlet airflow can be controlled to increase/decrease the particle density for the experiment. Titanium oxide particles (diameter 1-2 μm) were injected to the main air at the settling chamber for seeding from upstream of the fuel nozzle. The relaxation time of the particles, defined by $\tau_s = d_{particle}^2 \rho_{particle} / (18\,\mu_{fluid})$, provides a measure of the capacity of the seeding particles to follow the fluid [37]. The relaxation time was 13-52 μs for the 1-2 μm TiO_2 particles used at 1 atm air and 293 K. This relaxation time satisfied the required time response to represent the flow field from the seeding particles velocities. Relaxation time reduces at higher flow temperature due to increased flow viscosity.

3.1.4 Challenges and Guidelines for Optimized Measurement

The flow field produced by the fuel nozzle was previously studied at non-reacting conditions [89]. Measuring velocity fields in reacting flow with PIV is experimentally more challenging compared to non-reacting flow due to additional optical noise, e.g. flame luminosity, infrared radiations from solid surfaces. The control parameters of the PIV system (laser power, camera setting, and optical filters on the camera) were optimized to minimize signal contamination from the optical noise. The laser sheet was guided to the outside of the camera view after it passed the test section to reduce undesired glare. Under the optimal condition, it was possible to obtain enough signal intensity from the seeding particles. For stable and accurate

measurements, the camera and laser were mounted on sturdy frames to protect them from mechanical vibrations. Those instruments were cooled by external electric fans to prevent overheating by heat radiation from the combustor. A higher output power for the laser was preferred to maximize the Mie scattering signal from the particles relative to the unwanted optical noise which in general was independent of the laser intensity (except near the wall or when strong reflections are present, which were minimized in the present setup). Laser optical output was set close to its maximum (~130 mJ per pulse) during the measurement. An ND (neutral density) filter and a band pass filter in front of the lens module decreased external light and prevented saturation of the imaging sensor due to the strong laser signal. The focal plane was aligned on the laser sheet. Aperture of the lens system was fully open (f/2) to minimize noise from off-plane scattering, taking advantage of the narrower depth of field focused on the laser sheet. Any remaining background light scattering from the liner inner wall located out of the focal plane was removed by a background removal algorithm [89]. The data processing sequence incorporates background noise removal, an adaptive correlation, and peak validations. Due to higher noise in the reacting flow data, modifications were made on the previous sequence for robustness, which are avoiding dynamic range reduction when integer values are divided or subtracted, and applying median filter after averaging 400 snapshots (previously done on each snapshot).

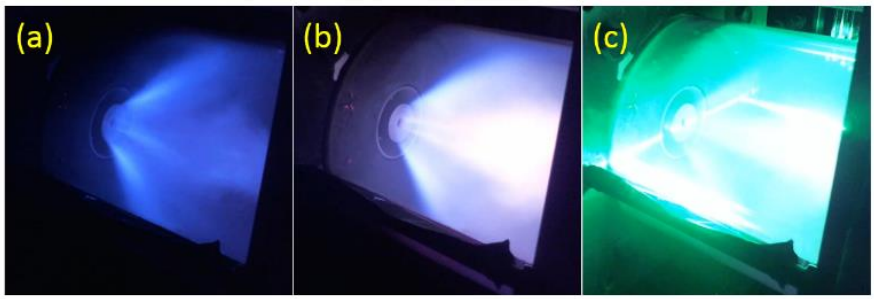

Figure 20. Photograph of PIV measurement in reacting flow;
(a) Flame luminosity (b) Glow from injected seeding particles (c) Scattering from laser sheet

There were two additional major technical difficulties during the reacting flow measurement after the optical optimizations mentioned above. First was maintaining a uniform and constant seeding density. Gently shaking the seeding particle container with an external force during the measurement improved the particle density quality, by dislodging any particle

clumps and allowing a more uniform mixture within the cyclone seeder. The second issue was minimizing seeding particle deposition on the optical liner. During the measurements, seeding particles gradually deposited on the liner wall, which generated a strong optical noise that deteriorated the acquisition as the measurement progressed. The particle deposition was not severe at non-reacting conditions. It appears that the high temperature or chemical content after reaction (e.g. formation of water vapor) in the reacting flow increased the amount of particle deposition on the optical liner during the experiment. This problem was minimized by cleaning the optical liner before each data acquisition and reducing the time span of the particle injection. The number of images taken during an experimental run was limited by acquisition duration and repetition rate. The maximum duration of data acquisition before liner contamination was about 1 minute, during which the PIV system could take 400 pairs of valid images at a 7.4 Hz repetition rate. The images taken after 1 minute of continuous particle injection could not be used due to degradation by particle deposition on inner liner wall.

3.1.5 Test Conditions

Experiments were designed to investigate differences in the flow fields depending on combustion parameters. Control variables were fuel-air equivalence ratios (ϕ), pilot fuel split ratios, and nozzle Reynolds numbers. To completely compare effects of pilot fuel ratios, equivalence ratios, and Reynolds numbers, a total of 7 cases were carried out. For each control variable, three different cases were compared as shown on Table 1. The characteristic length for non-dimensional scales and Reynolds number calculations was the fuel nozzle diameter.

Table 1. Test matrix of PIV velocity field measurement in reacting flow (k: $\times 10^3$)

Case	ϕ	Pilot %	Re #
R1	0.65	6	50 k
R2	**0.55**	6	50 k
R3	**0.78**	6	50 k
R4	0.65	**0**	50 k
R5	0.65	**4**	50 k
R6	0.65	6	**75 k**
R7	*0.55*	6	**110 k**

Steady and stable operation of the burner was achieved when the combusting flow avoided any strong thermo-acoustic instabilities or near blowout conditions. Therefore, the set points of the control variables were chosen within the stable flame regimes for the combustor setup. The stable equivalence ratios at a Reynolds number of 50000 were within 0.5-0.8, but this uppermost limit in equivalence ratio was reduced for a Reynolds number of 110000. To maintain a stable flame regime consistent with the other cases, the equivalence ratio set point of case 7 (Reynolds number 110000) was set to 0.55.

3.1.6 Flow Fields in Non-Reacting Flow and Reacting Flow

Flow structures inside a swirl combustor are shown in Figure 21. The premixed air fuel mixture expands forming a conical main jet flow until it interacts with the wall. Jet impingement location is where axial velocity component equals to zero near the liner wall. After the impingement, the main flow is attached to the liner wall, and moves downstream. A small portion of the flow moves upstream from the impingement towards the dome, which formed corner recirculation (outer recirculation). Due to swirl effect, another recirculation occurs in the center as well. Central recirculation (inner recirculation) is formed by vortex breakdown process when swirl number is more than a threshold value. This condition is determined by the swirler geometry. In this work, the swirl number of the flow was 0.74, which is higher than the threshold 0.6 [21]. Therefore, central recirculation was formed for all tests in this work.

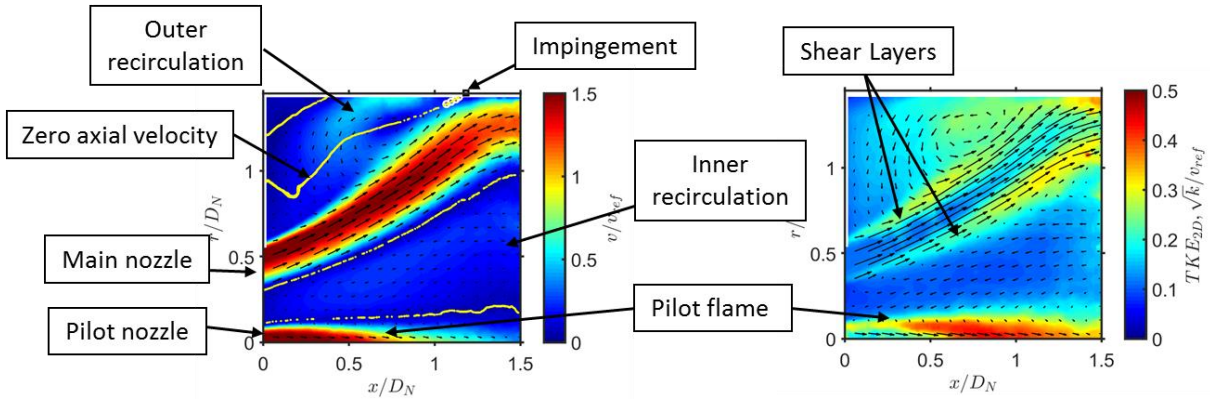

Figure 21. Features in PIV time average and TKE.

The characteristics of reacting flows are distinctly different from non-reacting flow. Figure 22 compares snapshots of instantaneous PIV measurements in non-reacting flow and reacting flow. The color scale represents magnitudes of velocity vectors for each pixel.

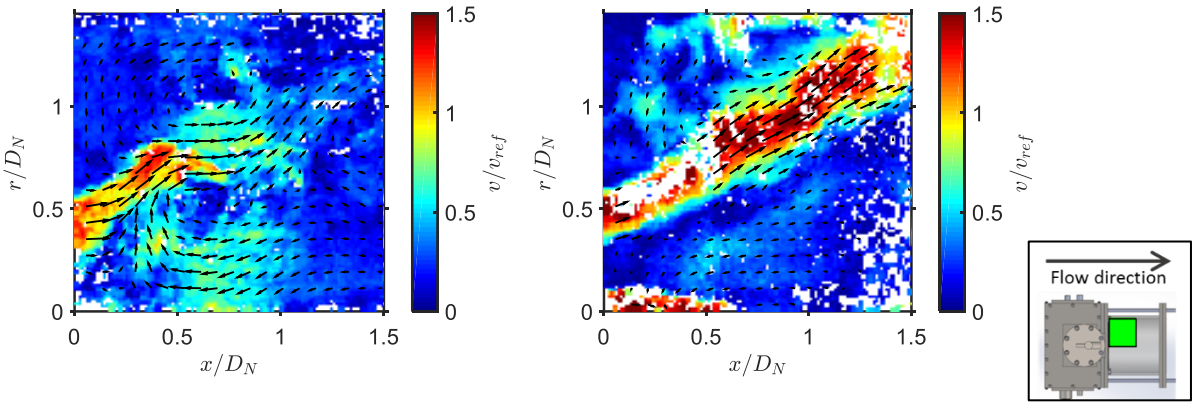

Figure 22. Snapshots of instantaneous flow field; (Top) Non-reacting flow, (Bottom) Reacting flow. There are no values at white spots.

The lean premixed swirl stabilized fuel nozzle was located on the left side of each figure, the bottom of each contour corresponds to the axis of the burner, and the liner wall would be located on the top of the contours. The measurement plane ($1.7\ D_N \times 1.7\ D_N$) included the fuel nozzle and the main flow impingement locations. The flow field was measured 2-dimensionally on the axial-radial plane, and the 2D velocities vectors can be denoted with two components.

$$\boldsymbol{v_{xr}} = v_x\hat{x} + v_r\hat{r} \tag{10}$$

Large scale vortices were recurrently observed in the non-reacting flow. In comparison, smaller vortices were distributed throughout the reacting flow. This vortex breakdown is consistent with previous flow field studies on reacting swirl flow [37]. An annular main flame is shown as a straight jet in the measurement plane. It is clear from these instantaneous images that the two regimes produce different flow behavior. The energization of the flow due to combustion is very strong for the reacting flow case. The central small jet shown on the bottom of the figure in reacting case is a pilot flame. When there is no particle signal at an interrogation area instantaneously, velocity value was not measured for the corresponding pixels, which are white spots in the Figure 22. These are excluded in averaging.

The mean velocity field in reacting flow was obtained from PIV measurements in reacting condition as shown in Figure 23. The arithmetic mean of the 400 snapshots ($\overline{\boldsymbol{v}}$) was used for each mean vector field. A 3×3 median filter was applied to the mean vector field to remove unphysical values (due to noise). Reynolds decomposition, as given by Equation 11, was then used to extract the fluctuating velocity component.

$$\boldsymbol{v} = \overline{\boldsymbol{v}} + \boldsymbol{v}' \tag{11}$$

The fluctuation part ($\boldsymbol{v}'$) was used to calculate the turbulent kinetic energy (TKE). This TKE distribution represents local velocity fluctuation, which is an important factor for flame stability and for convection heat transfer at the combustor liner. TKE in 2-D is characterized by the root-mean-square (RMS) of axial and radial velocity fluctuations, or the turbulence normal stresses in the measurement plane (Equation 12). This represents the mean kinetic energy associated with eddies in turbulent flow that were captured in the 2-D data.

$$k = \frac{1}{2}\left(\overline{v_x'^2} + \overline{v_r'^2}\right) \tag{12}$$

The magnitude of normalized velocity is presented in color scale. The reference velocity was the mean nozzle velocity (Equation 13), which was calculated from the inlet air flow rate divided by area of the nozzle (annular area between outer perimeter at the nozzle casing and inner perimeter at the center hub).

$$v_{ref} = \frac{\dot{m}_{air}}{\rho_{air} A_{nozzle}} \tag{13}$$

Figure 23 a and b show contour plots of mean vector fields in non-reacting and reacting flows respectively. Combustor parameters of the reacting case were 50000 Reynolds number, 0.65 equivalence ratio and 6% pilot fuel ratio. The annular jet velocities in general were higher in the reacting case because of the combustion reaction causing flow energization and forward volume expansion in the flow (high density gradient across the flame front). The maximum velocity in the main flow was about 1.1 v_{ref} in non-reacting flow and 1.6 v_{ref} in reacting flow.

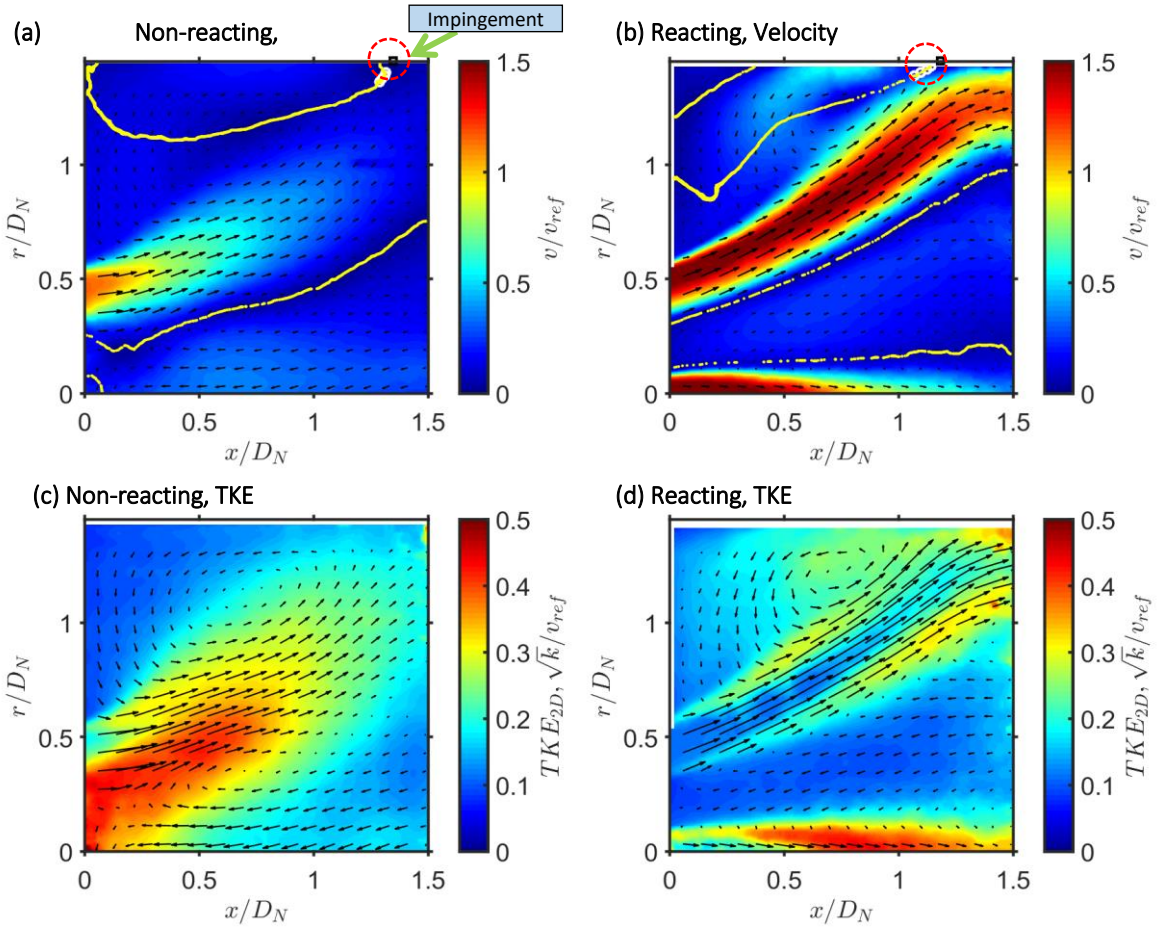

Figure 23. Mean velocity and TKE comparison between non-reacting and reacting flow; (a, c) Non-reacting NR1, Re 50 k, (b, d) Reacting R1 ϕ: 0.65, Pilot: 6%, Re 50 k (Fixed condition: Reynolds number: 50 k)

Thin yellow lines on the mean velocity contours are zero axial velocity locations. One of the lines was extended to the liner wall locations to determine the impingement locations of the flame. Corner recirculation and some part of central recirculation zones were observed in the mean flow field. Corner recirculation is clearly more intense, and the location of the center moved downstream in reacting flow. The pilot flame in the reacting flow broke down the central recirculation observed in the non-reacting case, splitting the central recirculation zone and confining it between the exiting annular jet and the pilot flame. TKE contour plots in Figure 23 c and d were based on two dimensional vectors from the PIV data, the vectors from the mean velocity field were overlaid on the plot for a clear reference on the flow structures. Shear layers are observed in the TKE plots. High turbulent regions lie on shear layers in case of reacting flow,

contrary to the non-reacting case with high turbulence in the inner recirculation zone. The TKE was high at the shear layer locations both in the main annular and pilot flame boundaries. The pilot flame in the reacting flow also induced high turbulence, because of the interaction with the inner recirculating flow. The amount of turbulent energy contained in the pilot flame is small compared to the main flame considering their actual volume in a cylindrical coordinate in 3-D. The precessing vortex core (PVC) effect is believed to be damped in the presence of combustion heat release and pilot flame, leading to the difference in TKE distribution observed at non-reacting conditions.

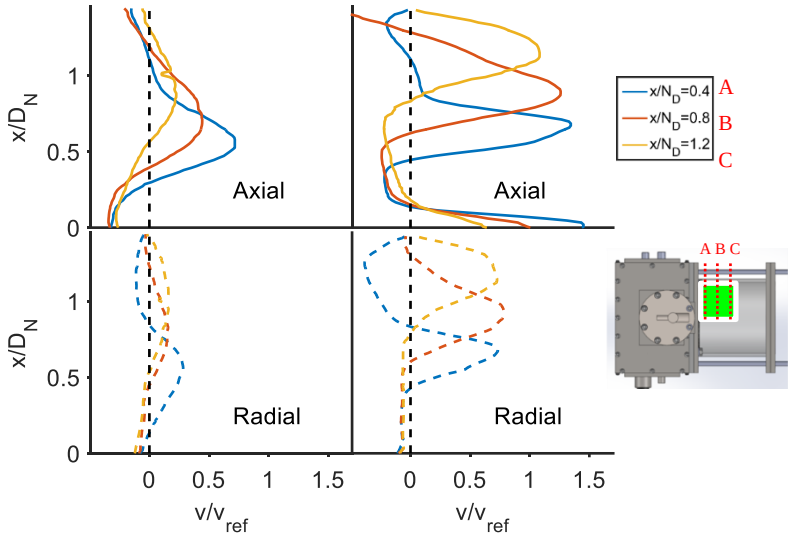

Figure 24. Velocity component profiles comparison; (a) Non-reacting NR1, Re 50 k, (b) Reacting R1 ϕ: 0.65, Pilot: 6%, Re 50 k (Fixed condition: Reynolds number: 50 k)

Axial and radial velocity components at multiple axial locations are shown in Figure 24 in non-dimensionalized scales. Three axial locations are shown in different colors. Axial velocity profiles were normalized with respect to the reference velocity at the fuel nozzle. Both the axial and radial velocity decayed down quickly in the non-reacting flow, but the rate of decay was slower in reacting flow. This indicates that the reacting main jet flow expands due to heat release from combustion and the density decreases as the jet flows downstream. Another notable difference is the radial location of the velocity peaks. The peaks on the reacting flow were farther from the center at the same axial locations, which indicates that the annular jet dissipates less and expands faster in reacting flow. This was contrary to the expectation, which assumed that the inner recirculation bubble was the main driving mechanism for the annular jet

expansion. This inner recirculation was broken down by the pilot flame, and in spite of this, annular jet expansion was faster in the reacting case.

3.1.7 Self-Similarity in Reacting Flows under Different Conditions

Self-similar flow features were observed in reacting flow under different equivalence ratios. Flame size, shape and magnitude of velocity in the main flame at different equivalence ratios are compared with the mean velocity contours. The TKE contours were qualitatively compared to understand the effects of the test variables in the turbulence properties.

Figure 25 shows comparisons of mean velocity fields and TKE distributions under different fuel-air equivalence ratios (0.55, 0.65, and 0.78). Pilot fuel split and Reynolds numbers were maintained constant for the three cases. Different equivalence ratios affect the flow inducing minor changes on the flame shape. The main annular flame was larger and more intense at the highest equivalence ratio (c). The width of the annular jet was also larger at this condition, suggesting that the higher equivalence ratio leads to a more rapid exchange of momentum with the surrounding flow, broadening the annular jet. For the low equivalence ratio (d), TKE was higher because of two reasons, first being the damped vortices, and second the flame was slightly less stable leading to larger oscillations. The recirculation intensity also increased at higher equivalence ratio. Apart from these observations, the flame shape in general, including swirl impingement locations on the liner wall, were similar for all tested equivalence ratios.

TKE was relatively high for an equivalence ratio of 0.78. TKE was also high with low equivalence ratio, because flame structure vibrates in time due to slight instability. Among these cases, the most stable flame was observed with an equivalence ratio 0.65. High TKE locations near liner impingement were similar.

The second control variable was the pilot fuel split ratio. The self-similarity also holds for different pilot fuel flow cases. Pilot fuel ratio had an insignificant effect on the main flow as observed in the mean flow field. The mean velocity field and TKE were almost identical for different pilot fuels. TKE at the boundary regions slightly increased as pilot fuel flow decreased, because of reduced stability of the main flame.

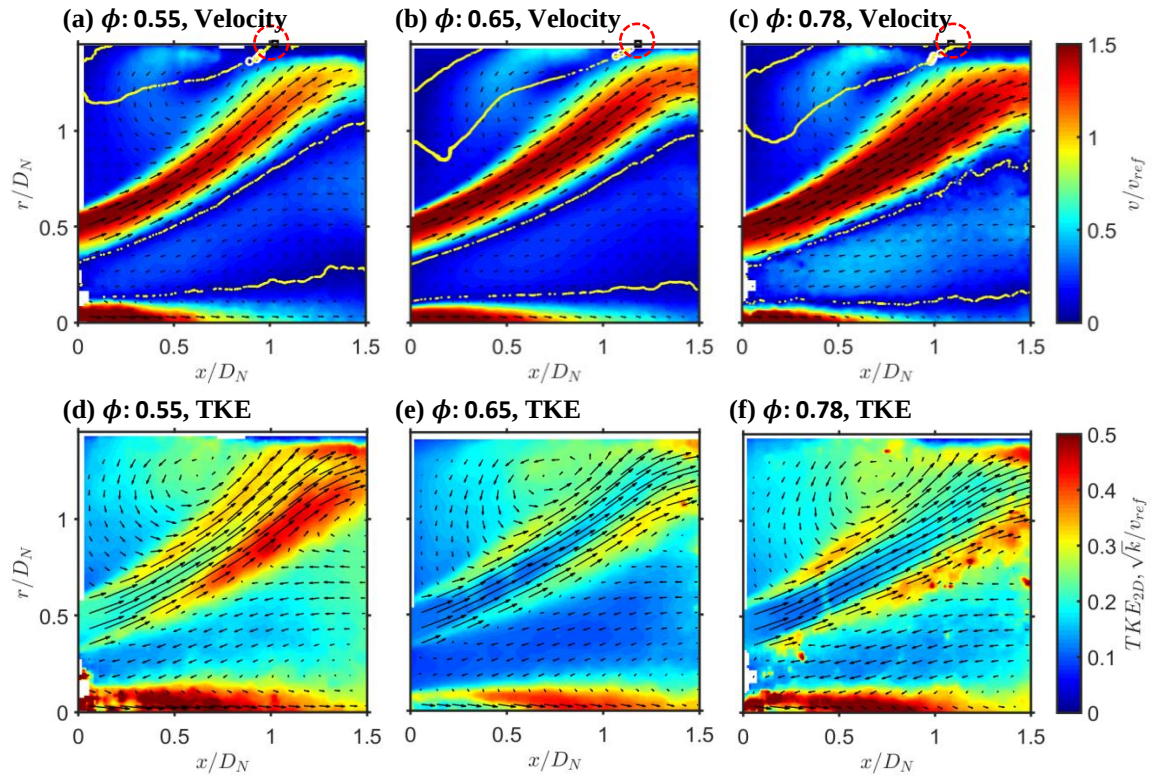

Figure 25. Mean velocity and TKE comparison with different equivalence ratios (Fixed conditions: Reynolds number: 50000, Pilot: 6%)

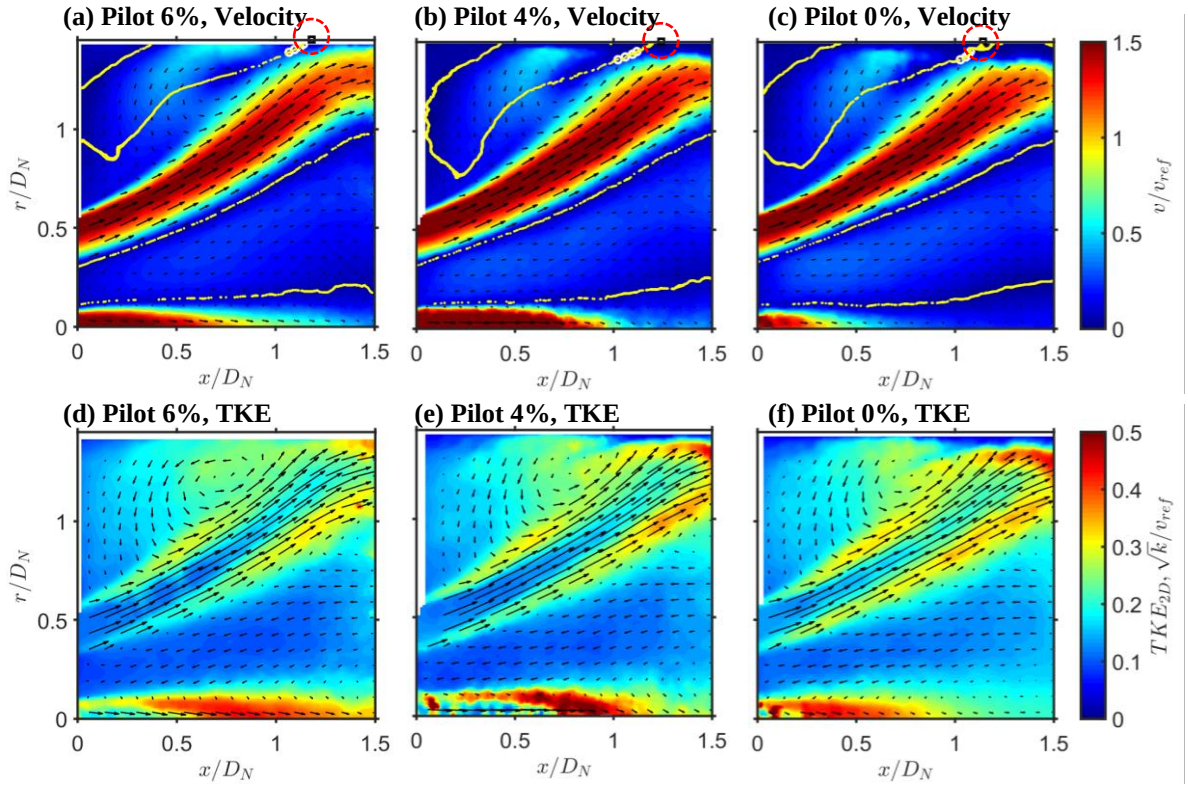

Figure 26. Mean velocity and TKE comparison with different pilot fuel split ratio (Fixed conditions: Reynolds number: 50000, ϕ: 0.65)

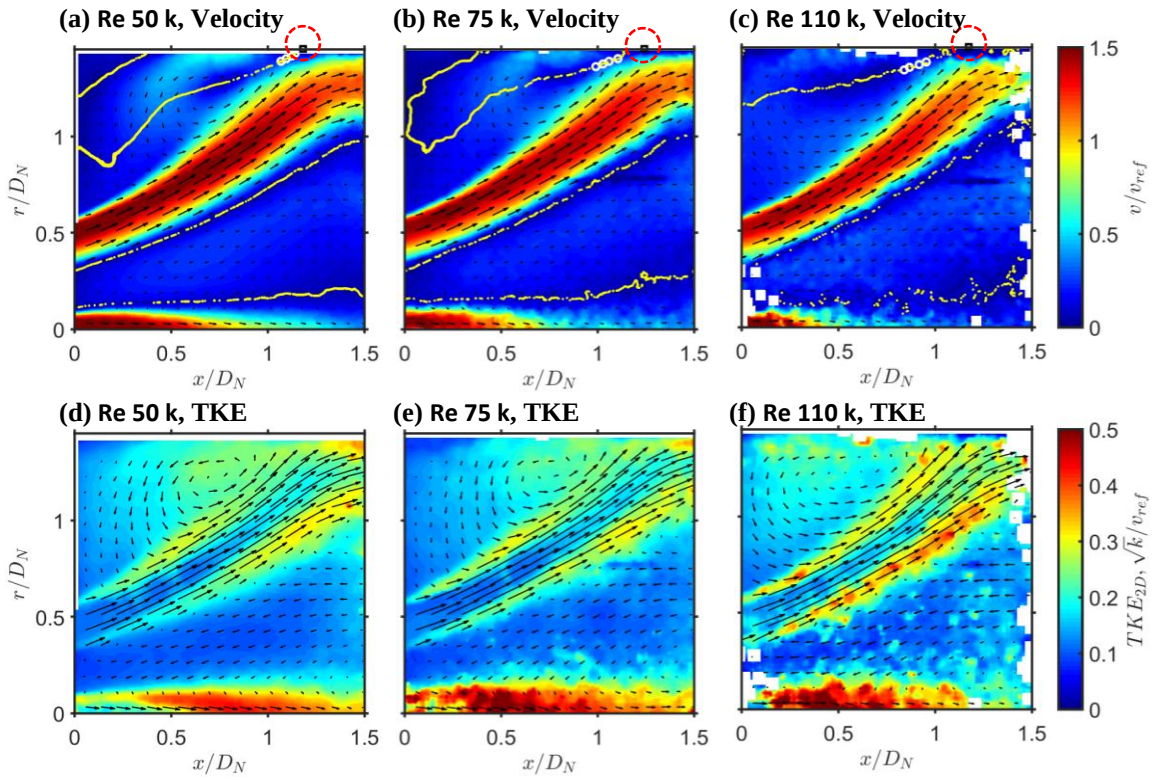

Figure 27. Mean velocity and TKE comparison with different Reynolds numbers (Fixed conditions: Pilot 6%, ϕ: 0.65 for a, b, d, e, ϕ: 0.55 for c, f)

There was no pilot fuel supplied during the zero pilot case (c, f), but there was still forward flow downstream of the pilot nozzle. This is because a few percent of the flow in the main annular premixing portion of the nozzle flows through pilot. This leads to a central jet flow, even with the pilot fuel valve closed completely. This was an interesting phenomenon that was not previously noted in previous studies.

Within the range of studied pilot set points (0 – 6%), there appears to be only minor effects on the mean and fluctuating flow. Usual conditions of operation for low-emission gas turbine combustors maintain low pilot fuel ratios to reduce emissions, since the local equivalence ratios in the pilot flame are generally higher than in the main flame.

The last control variable was Reynolds number, or mass flow rate. The self-similarity was also observed for different Reynolds numbers in Figure 27 consistent with observations at non-reacting conditions [88]. Reynolds numbers with respect to the fuel nozzle diameter were set to 50000, 75000 and 110000. In the 110000 Reynolds number case (c and f), a stable flame

could not be achieved at an equivalence ratio of 0.65. In consequence, the main flame zone was thinner due to a lower equivalence ratio. The peak main flow velocity increased with Reynolds number, but the normalized velocity fields were self-similar with Reynolds number. After the velocity was normalized with respect to the velocity at the fuel nozzle, the magnitudes of the peak were almost the same.

Self-similarity with respect to the different combustor operating conditions can also be observed in the mean velocity component profiles. The velocity components at different conditions (R2-R7 in Table 1) are compared in Figure 28, which can also be compared with R1 in Figure 24. Top figures are axial velocities and bottom ones are radial velocities for each case. Cross-section locations are the same as those shown in Figure 24. Most of the observable features in the flow velocity were independent of pilot fuel ratio, equivalence ratio, and Reynolds number. In other words, the reacting flows show small differences, compared to the differences observed between non-reacting and reacting conditions as shown in Figure 24. The equivalence ratio changed the magnitudes of the peaks and width of the main annular flame jet (a, b in Figure 28). The recirculation velocity was also higher with high equivalence ratio. However, there was no consistent effect observed in the locations of the velocity peaks suggesting that the flame expansion was independent of all tested conditions.

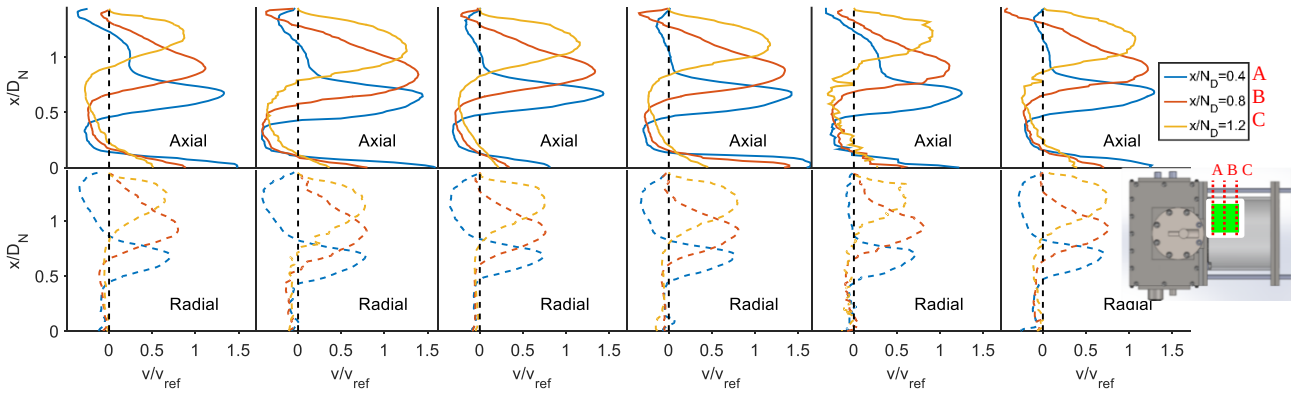

Figure 28. Velocity component profiles comparison with different conditions: R2-R7. x/DN=0.4(Blue), 0.8(Red) 1.2(Yellow)

3.1.8 Impingement Locations of Reacting Flows on the Liner Wall

The reacting flow impingement locations on the liner wall were compared in reacting flows under different conditions. Zero axial velocity crossings at several axial velocity profiles were

identified near the wall, and then the zero axial velocity location at the wall ($r = 1.45\ D_N$) was determined from a line fitting extrapolating the jet expansion trend observed. This procedure is exemplified in Figure 29. Four lines were used near maximum radial location available in the data. The reason for extrapolating the location of impingement was that the data near the liner wall was unreliable due to the intense glare and reflection from the laser sheet in PIV experimental data.

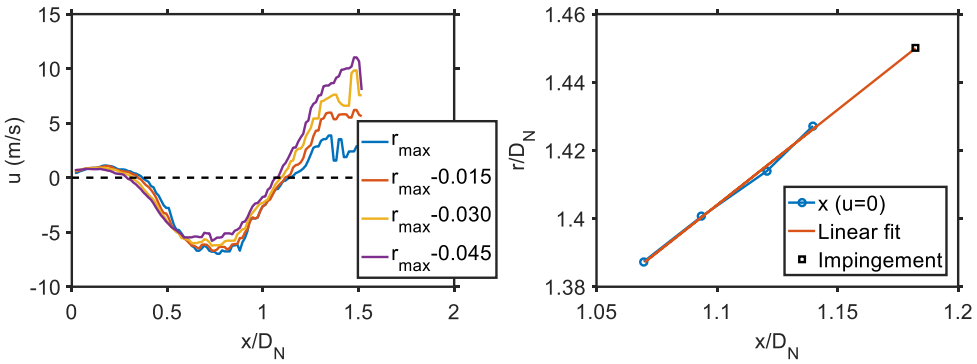

Figure 29. Procedure to determine impingement location; Left: Axial velocity profiles (along the x/D_N direction) near the maximum radial location (rmax), Right) Extrapolation of zero velocity location.

The impingement locations found at different combustor operating conditions are shown in Table 2. In this study, the locations were consistent around $x = 1.16\ D_N$ with standard deviation of 7% ($0.08\ D_N$) in the 7 reacting cases. Impingement locations found in two non-reacting measurements are given as a reference as well. In the non-reacting case, impingement locations were at a farther downstream axial location ($x \approx 1.33 D_N$). As observed in Figure 24, the main flow expands more in reacting flow. As a consequence, impingement locations are different in reacting flows. This is an important finding as liner cooling geometry design will depend on this impingement location.

Figure 30 shows the mean axial velocity near the wall as a function of axial location (radial locations within $1.3\ D_N \leq r \leq 1.4\ D_N$ range). Although the zero crossing on this plot could not accurately measure the jet impingement location, the difference in the reacting flow and non-reacting flow is clearly visualized. This was also contrary to the speculation of the flow expansion across the flame front leading to a downstream impingement location compared to the non-reacting case.

Table 2. Jet impingement locations on the liner wall in non-reacting flows (NR) and reacting flows (R)

Case	ϕ	Pilot %	Re #	x/D_N	Deviation
R1	0.65	6	50 k	1.18	+1.9 %
R2	0.55	6	50 k	1.01	-12.8 %
R3	0.78	6	50 k	1.10	-5.0 %
R4	0.65	0	50 k	1.17	+1.0 %
R5	0.65	4	50 k	1.23	+6.2 %
R6	0.65	6	75 k	1.25	+7.9%
R7	*0.55*	6	110 k	1.17	+1.0 %
NR1	-	-	50 k	1.34	-
NR2	-	-	50 k	1.32	-

This observation conflicts with the results in numerical investigations. This could be due to the limited data close to the liner wall in the experiment. The effect of reaction to the flame structure needs to be studied further both experimentally and computationally to draw a firm conclusion.

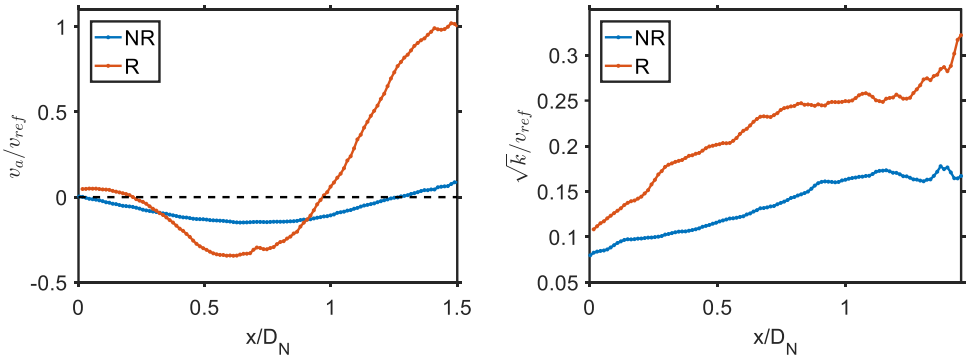

Figure 30. Averaged near wall profiles; Left: axial velocity, Right: TKE in non-reacting flows (Blue) and reacting flows (Red), for radial location $1.3\ D_N \leq r \leq 1.4\ D_N$.

3.1.9 Summary and Discussion

Flow fields were measured with planar PIV for reacting flow in a lean-premixed swirl-stabilized can combustor. Significant differences between non-reacting and reacting flows were observed in mean flow fields and TKE fields. The rate of velocity decay along the main annular jet flow was higher in non-reacting case. Size of vortices decreased in reacting flow. Flow energization

due to heat release expanded the flow and generated strong density gradients at the jet boundary in reacting flow.

This work has addressed the effects of important combustor parameters on the reacting fluid dynamics and self-similar characteristics of reacting flows observed in a realistic gas turbine combustor with an actual industrial fuel nozzle. An observation of practical importance in the current study was the self-similarity in reacting flows. Regardless of the combustor operating conditions, the normalized flow fields and TKE were similar.

Observations within our group have shown that the geometry downstream of the combustor primary zone has a significant impact on the flow field and heat transfer within the combustor [52,92]. If the heat transfer characteristics depend on the transition piece shape and size; it is important for the design of combustors to characterize this dependence. For this reason, future work should focus on reacting PIV measurements of the flow field using different geometries downstream of the combustor primary zone.

3.2 PIV MEASUREMENT AND POD ANALYSIS

The second set of PIV measurement used propane fuel. After a rig upgrade, control and measurement were more accurately performed. Effects of equivalence ratio, air mass flow rates and inlet air temperature on the flow features were tested. An attempt of POD analysis was applied to capture the coherent structure.

3.2.1 Background

Heat transfer and flow structures are important aspects to develop improved combustor designs. The flow field properties drive convection heat transfer from the flow to the solid surface. Understanding the mechanism of lean premixed combustion at swirling flows in modern combustors is a challenging topic of research. Experimental studies on effects of combustor conditions on the flow fields are necessary to understand the behavior of realistic reacting flows in the combustors.

Early studies on swirl flows were reviews by Lilley [21] and Syred et al.[23], which cover vortex breakdown mechanism and presence of PVC. These investigations were mostly about diffusion flames. Lean premixed combustors are widely used in modern gas turbine combustors to lower pollutant emissions and to enhance efficiency especially for land-based gas turbines [93]. To better understand heat transfer and flow fields in lean premixed swirl combustors, Patil et al. [51], Andreini et al. [55] conducted detailed measurement of convective heat transfer on the liner wall along with PIV flow field measurements. These PIV measurements on non-reacting flows focused on relationship between flow structure and heat transfer, but their scope did not cover reacting flows.

Reacting flow fields of lean premixed fuel nozzles have been extensively studied. Ji and Gore [37] focused on the comparison between a non-reacting and a single reacting condition in unconfined flows. Flows under various topology were reported by Chterev et al. [94]. Huang and Yang [20] reported combustion dynamics study regarding stability in the swirl flow. Stopper et al. [88] quantified pressure influence on flame shapes. Kewlani et al. [95] used swirl combustor to investigate impact of equivalence ratio. Berrino et al. performed POD analysis on the PIV flow field data [96]. These recent research progresses have extended understanding of flow fields remarkably.

The objective of this work is to investigate the effects of reacting conditions on the flow structures including air flow rate, equivalence ratio and inlet temperature under realistic swirl flows using an industrial swirl nozzle. For future use in heat transfer study, jet impingement location on liner wall is one of the major focuses. Previous works within the group provided basis of this work [52,89,97].

3.2.2 Experimental Setup

A PIV camera was installed on top of the test section and captured image pairs on a flat laser sheet parallel to the ground at the same height as the central axis of the combustor as shown in Figure 18. Distance from the laser sheet and the camera was ~0.9 m. The aperture of camera lens system was f/2 (fully open). The camera was cooled down with an electric fan to protect from heat and to keep steady focus setting. Laser power was set close to its maximum (~130 mJ per pulse). The time between laser pulses was set to 30 μs. Repetition rate was set to 7.4 Hz which was limited by the camera.

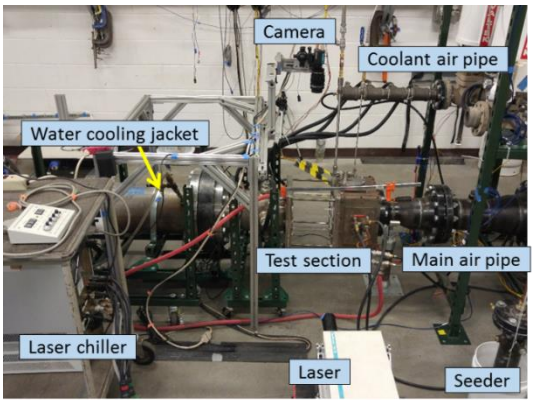

Figure 31. Photo of optical combustor test rig and PIV system

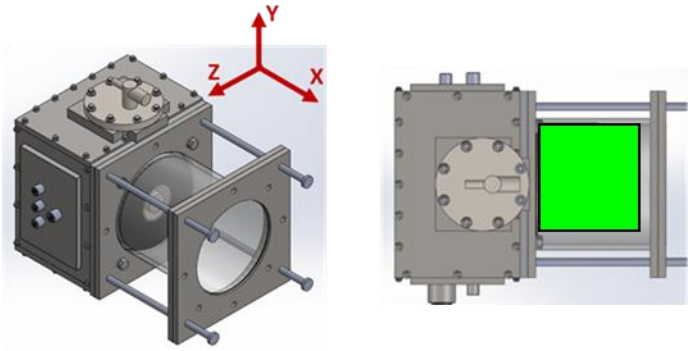

Figure 32. PIV region of interest for full primary zone

A cyclone seeder was used for seeding. A bypass air was tapped from upstream of air control valve, which supplied about 1-2 g/s air to the seeder. 1 μm alumina particles (Baikowski, CR1) were injected into the settling chamber, and introduced to the test section along with air. PID control of the control valve compensated the amount of bypass air for seeding. The relaxation time of the particles, defined by $\tau_s = d_{particle}^2 \rho_{particle} / (18\,\mu_{fluid})$ was calculated as 12.1-2.4 μs, assuming 1 μm alumina in air at 15-1600 °C. Particle seeder was being gently shaken during the measurement, to maintain sufficient particle density continuously.

Initial data processing was performed with Dynamic Studio. The background was calculated from a local minimum of multiple images, and subtracted from the raw images. Then, the corrected images were normalized with time-averaged images. Each pair of images were analyzed using adaptive correlation with a final interrogation area of 32×32 yielding 128×128 vectors [89]. Neighborhood and peak validations verified the vectors after adaptive cross-correlation. Invalid vectors and substituted vectors (during validation process) were excluded in the analysis. Further analysis and plotting was performed in MATLAB. Functions such as 'nanmean' and a variation of 'nanmedfilt2' were used for mean calculation and noise removal in the data.

A significant challenge of PIV measurement was about laser glares. Due to tubular geometry of the quartz glass liner, multiple reflections of laser glares from the solid surfaces were difficult to avoid, which caused data loss at some locations.

3.2.3 Test Conditions

The test matrix for experiments is shown in Table 3. Four different air mass flow rates were selected for non-reacting flow cases. The Reynolds number is a parameter representing air mass flow rate. Control variables for reacting flows are air mass flow rate, fuel-air equivalence ratio, and inlet air temperature. 2-3 cases of different conditions were compared to a base case for each property. Pilot fuel split ratio was constant at 6% of the total fuel flow. The measurements were conducted when the flame is steady and stable by observing acoustic noise and flame luminosity.

Table 3 Test matrix of PIV measurements

Control variable	T_{inlet} (°C)	Re ($\times 10^3$)	ϕ	Case #
Re (NR)	23	**50**		C1
	23	**70**		C2
	23	**90**		C3
	23	**110**		C4
Re (R)	23	**50**	0.60	R1
	23	**70**	0.60	R2
	23	**90**	0.60	R3
	23	**110**	0.60	R4
ϕ (R)	23	50	**0.55**	R5
	23	50	**0.60**	R1
	23	50	**0.65**	R6
	23	50	**0.70**	R7
T_{inlet} (R)	**23**	50	0.60	R1
	100	50	0.60	R8
	200	50	0.60	R9

Reynolds numbers for air mass flow rates were calculated with respect to fuel nozzle throat diameter (D_N). Characteristic length for non-dimensional length scales was the nozzle diameter as well.

3.2.4 PIV Measurement Results

The flow field was measured 2-dimensionally on the axial-radial plane, and the 2D velocities vectors can be denoted with two components.

$$\boldsymbol{v_{xr}} = v_x\hat{x} + v_r\hat{r} \qquad (14)$$

The mean velocity field in reacting flow was obtained from PIV measurements in reacting condition. The arithmetic mean of the 400 snapshots ($\overline{\boldsymbol{v}}$) was used for each mean vector field. A 3×3 median filter was applied to the mean vector field to remove unphysical values (due to noise). Reynolds decomposition, as given by Equation 15, was then used to extract the fluctuating velocity component.

$$\boldsymbol{v} = \overline{\boldsymbol{v}} + \boldsymbol{v}' \qquad (15)$$

The fluctuation part ($\boldsymbol{v}'$) was used to calculate the turbulent kinetic energy (TKE). This TKE distribution represents local velocity fluctuation, which is an important factor for flame stability and for convection heat transfer at the combustor liner. TKE in 2-D is characterized by the root-mean-square (RMS) of axial and radial velocity fluctuations, or the turbulence normal stresses in the measurement plane (Equation 16). This represents the mean kinetic energy associated with eddies in turbulent flow that were captured in the 2-D data. Root of TKE $\sqrt{k}$ was normalized with the reference velocity and used for the plots.

$$k = \frac{1}{2}\left(\overline{v_x'^2} + \overline{v_r'^2}\right) \qquad (16)$$

Vorticity is another flow property obtained from PIV data. Equation 17 shows definition of vorticity in this 2D measurement plane. Vorticity was calculated from the instantaneous snapshots, and then time averaged.

$$\Omega = |\boldsymbol{\nabla} \times \boldsymbol{v}| = \frac{\partial v_r}{\partial x} - \frac{\partial v_x}{\partial r} \qquad (17)$$

The magnitude of normalized velocity is presented in color scale. Field properties such as velocity were scaled with reference velocity, which is mean nozzle velocity (Equation 18), which was calculated from the inlet air flow rate divided by the area of the nozzle (annular area between outer perimeter at the nozzle casing and inner perimeter at the center hub).

$$v_{ref} = \frac{\dot{m}_{air}}{\rho_{air} A_{nozzle}} \qquad (18)$$

3.2.5 Effect of Reaction on the Flows

Significant differences were observed by comparing non-reacting flow and reacting flow with mean velocity, turbulent kinetic energy, and vorticity in Figure 33. Flow direction is from left to right with the nozzle on the left side (x = 0, -0.5 < r/D_N < 0.5).

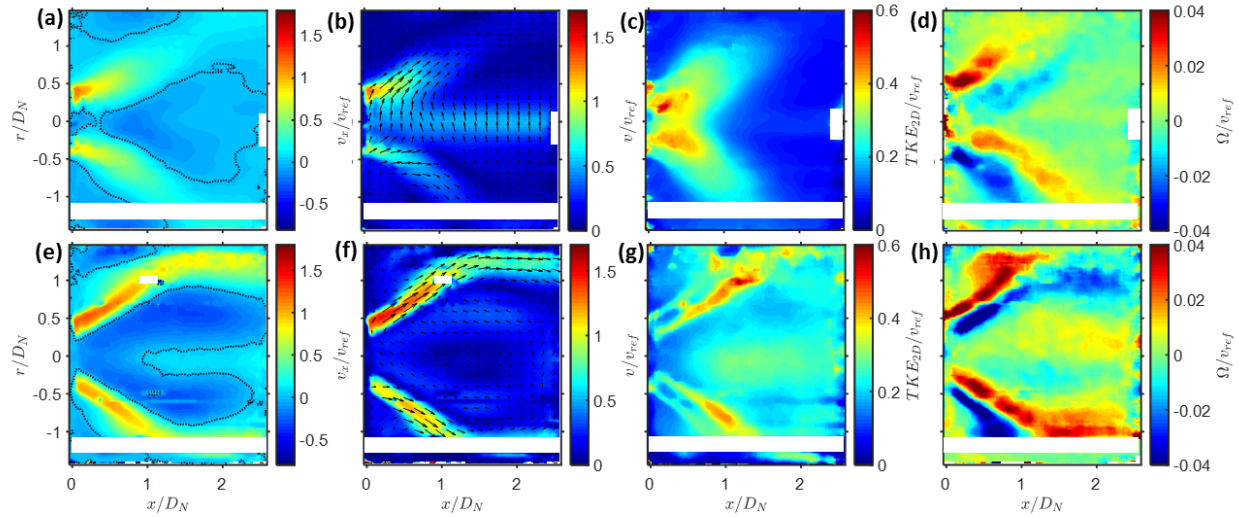

Figure 33. Axial velocity (a, e), velocity vector (b, f), turbulent kinetic energy(c, g), vorticity (d, h), distributions of non-reacting flow (a, b, c, d) and reacting flow (e, f, g, h)

The magnitudes of time-averaged axial velocity for non-reacting flow (a) and for reacting flow (e) are compared in Figure 33. Black dotted contours show the location where axial velocity is zero. These zero axial velocity curves were used to determine impingement locations. Plot (b) and (f) show time-averaged velocity vectors and velocity magnitudes in color scale. Plot (c) and (g) are TKE distribution in non-reacting and reacting flows. Time-averaged vorticity plots are shown in (d) and (h). The area where the noise covers the signals from the particle were marked in white.

The maximum normalized velocity in the main flow was about 1.1 in non-reacting flow and 1.6 in reacting flow. The annular main jet velocities were higher in the reacting case because of the combustion causing flow energization and forward volume expansion in the flow. In other words, the reacting main jet flow expands due to heat release from combustion and the density decreases as the jet flows towards downstream. During this process, the density of the fresh air-fuel mixture is higher than surrounding fluids. The density ratio of reactant to product was estimated as 5-7 from combustion calculations. Main jet flow in non-reacting case decays quickly,

and axial velocity is lower at the wall attached flow. Pilot jet is not visible in the PIV data, because of low momentum of pilot flow. It seems to be not high enough to be detected or the measurement plane was not positioned exactly at the flow axis.

Shear layers are observed in the TKE plots and also vorticity plots. High turbulent regions lie on shear layers in case of reacting flow, contrary to the non-reacting case with high turbulence is located near the dome. High vorticity of the opposite direction is more prominent in reacting flow. High TKE region inside inner shear layer of non-reacting flow can be explained with precessing vortex core (PVC). PVC is usually found near the inner shear layer in non-reacting swirl flow, but not in reacting flows. Propagation of the flame into the incoming mixture and heat release from the flame breaks down the vortex. Vortices in reacting flows are turned to small eddies and then dissipates [95].

3.2.6 Effects of Conditions on Reacting Flows

Flow fields were not affected by air mass flow rates. Flow structures observed in normalized mean velocity fields with different Reynolds numbers are compared for non-reacting flows (Figure 34) and reacting flows (Figure 35). Expansion angle of jet flow, the magnitude of normalized velocity are very similar for four different Reynolds number cases for both non-reacting and reacting flows.

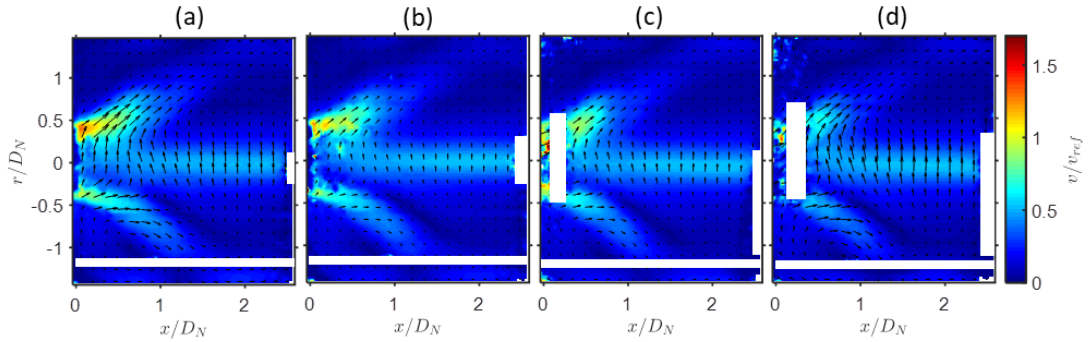

Figure 34. Velocity vectors of reacting flows with different air mass flow rates, Re = 50000 (a), 70000 (b), 90000 (c), 110000 (d) with respect to the nozzle diameter.

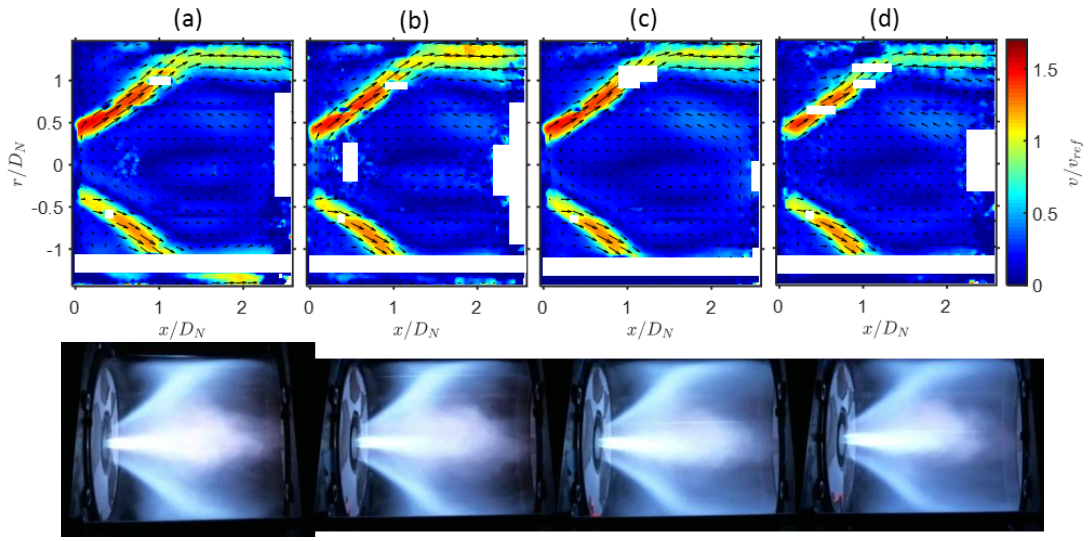

Figure 35. Velocity vectors and flame images of reacting flows with different air mass flow rates, Re = 50000 (a), 70000 (b), 90000 (c), 110000 (d) with respect to the nozzle diameter.

Cases with different equivalence ratios are compared in Figure 36. Flow structures, in general, were invariant, but velocities at wall attached flow were higher with high equivalence ratio. Normalized magnitudes of velocity at location x/D_N= 1.8, r/D_N= 1.2 were 0.7, 0.9, 1.0, and 1.1 for equivalence ratios 0.55, 0.60, 0.65 and 0.70. Velocities at the main jet flow from the nozzle showed the same trend implying high density gradient across the flame front. There was no significant difference in the velocities observed in the other regions. Size of corner recirculation zone and central recirculation zone in the measurement plane were similar as well.

The flow fields were not sensitive to inlet air temperature. In Figure 37, the flow structures are similar, but the velocity is higher for high inlet temperature case. Velocity in the inner recirculation also increases with inlet temperature increase. The increase was expected because the reference velocity did not account the volume expansion due to preheating. If the actual mean velocity at the nozzle were used for normalization, the flow fields would have been almost identical.

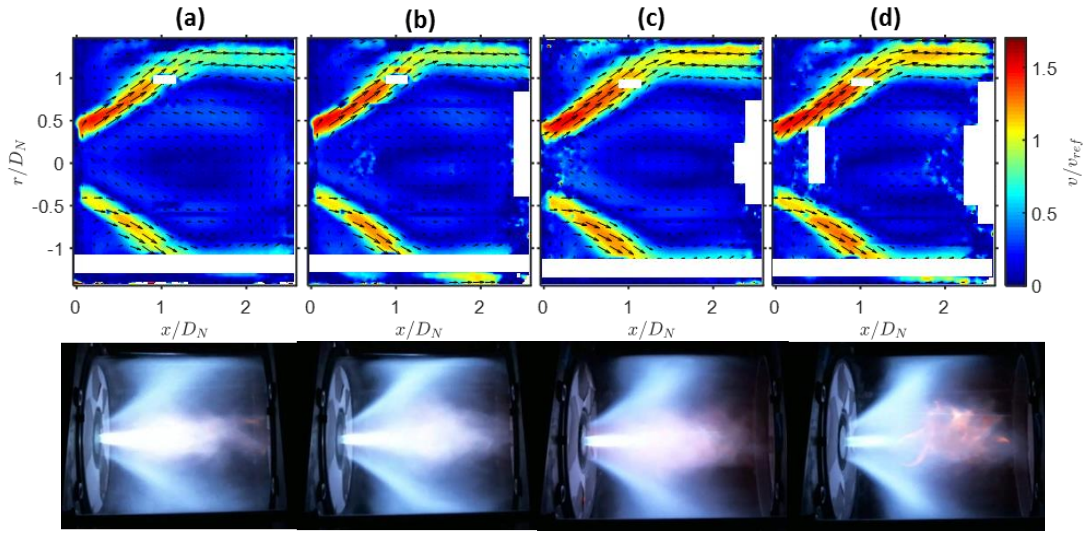

Figure 36. Velocity vectors and flame images of reacting flows with different equivalence ratios, ϕ = 0.55 (a), 0.60 (b), 0.65 (c), 0.70 (d)

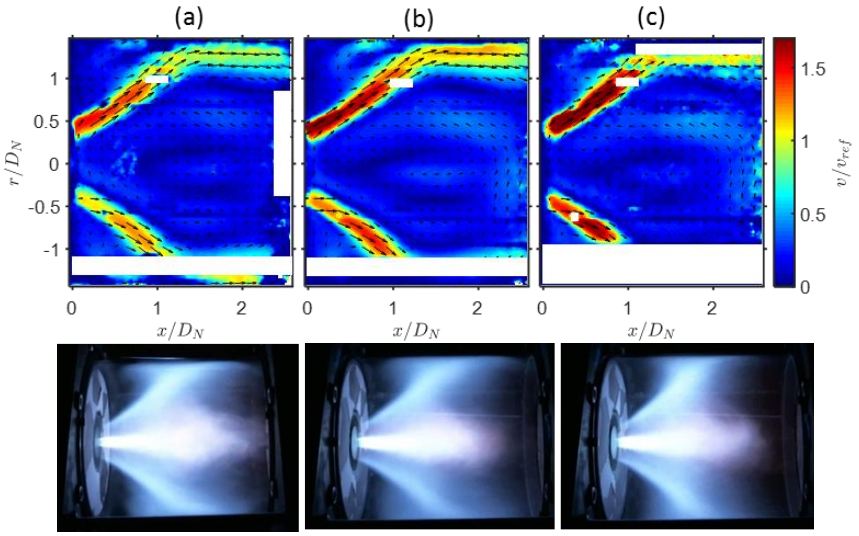

Figure 37. Velocity vectors and flame images of reacting flows with different inlet air temperatures, T = 23 °C (a), 100 °C (b), 200 °C (c).

A notable observation in the equivalence ratio test and inlet temperature test is that the trends of central recirculation velocities are different. Normalized magnitudes of velocity at the center recirculating flow (x/D_N = 1.7, r/D_N = 0.5) were consistent at 0.3 for equivalence ratio variations, but they were more than 0.4 for preheated cases. This is the color difference in the contour. Although both control variables provides thermal expansion in the flow, but their effects are different. Flow expansion by heat from reaction inside the combustor is more complex to explain than the incoming expanded air by preheating.

3.2.7 Impingement Locations

The jet impingement on the liner wall is important in confined reacting flow because the heat transfer is closely related to the flow structure. In this work, zero axial velocity location near the wall ($r = 1.45\ D_N$) is defined as impingement location.

The impingement locations found at different combustor operating conditions are shown in Figure 38. In this study, the locations were consistent around $x = 1.14\ D_N$ with standard deviation of 3.5% for 11 reacting cases. The impingement locations in 6 non-reacting cases were around $x = 1.39\ D_N$ with standard deviation of 2.1%. Repeatability of the locations was checked with multiple measurements. Standard deviations of impingement locations with 3 non-reacting runs and 3 reacting runs were 0.026 D_N (1.8%) and 0.019 D_N (1.6%) respectively.

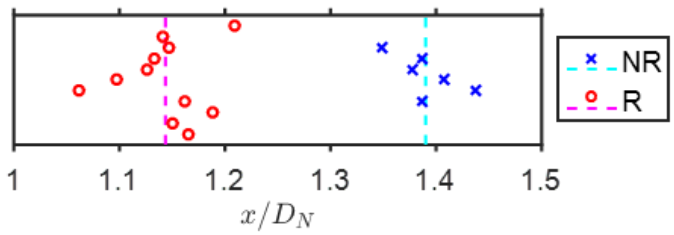

Figure 38. Measured jet impingement locations on the liner wall of non-reacting (NR) and reacting (R) flows

The impingement occurs closer to the dome in reacting flow than non-reacting flow. Size of corner recirculation zone changes due to different flow structures and the impingement location changes at the same time. Other combustor operating conditions, which are Reynolds number, equivalence ratio, or inlet air temperature, did not show a significant effect on the impingement location. The location is function of swirl number and combustor geometry only [94].

This conclusion does not agree with the previous numerical study on the same combustor geometry [52]. The simulation using RANS model might not be able to accurately estimate the impingement location. LES simulation result performed on a similar type of combustor by Kewlani et al. [95] agrees to this experimental result.

3.2.8 POD Analysis

There are three components in the instantaneous flow fields, which are time average, coherent, and random components. Total fluctuation of the flow is combination of coherent and random components. The PIV system can be operated at 7.4 Hz acquisition rate, which is not able to resolve high-frequency phenomena in the flow. Proper orthogonal decomposition (POD) method can extract information about coherent structures in the flow even though the data is not time-resolved. Detailed description and the mathematical procedure can be found in [89,96].

POD first computes eigenvalues, eigenvectors from autocovariance matrix of PIV data. The eigenvalues represent fluctuation energy contributions, and the eigenvectors provides temporal information of the modes. POD mode is obtained by projecting the original data on the eigenvectors. The POD modes are ordered by energy contributions to identify spatial information of the most energetic coherent structures in the flow.

PIV data were analyzed by POD. One non-reacting case and two reacting cases with different equivalence ratios were selected. Mode energy contribution and three most energetic modes for selected cases are shown in Figure 39-Figure 41. The first reacting case is a typical condition (R1, base reacting case), and the other reacting case is a lean condition.

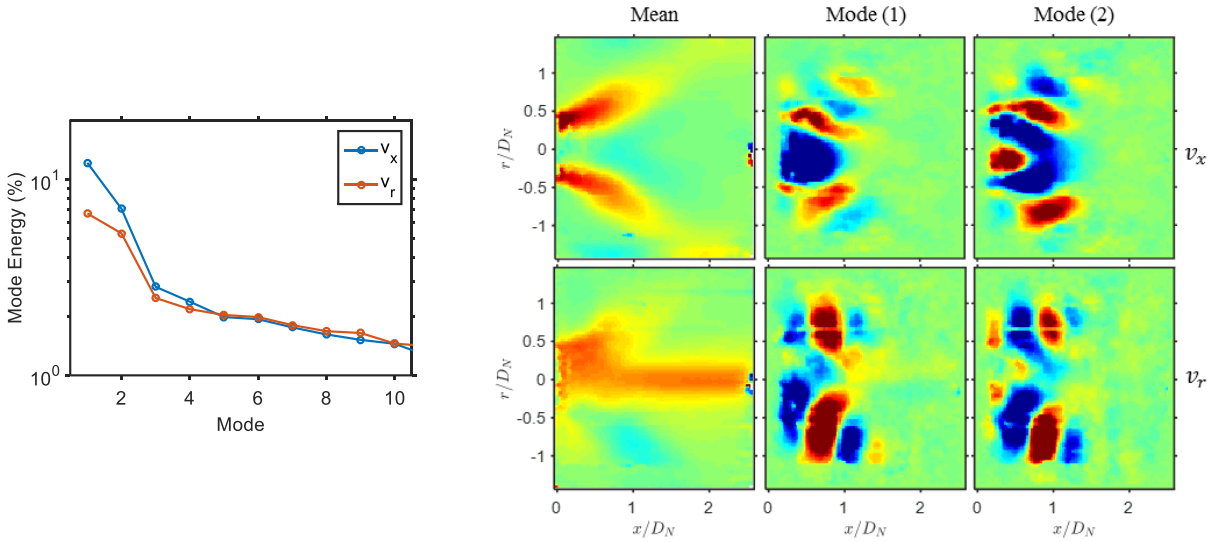

Figure 39. Mode energy contribution and three most energetic POD modes for case C1 non-reacting flow

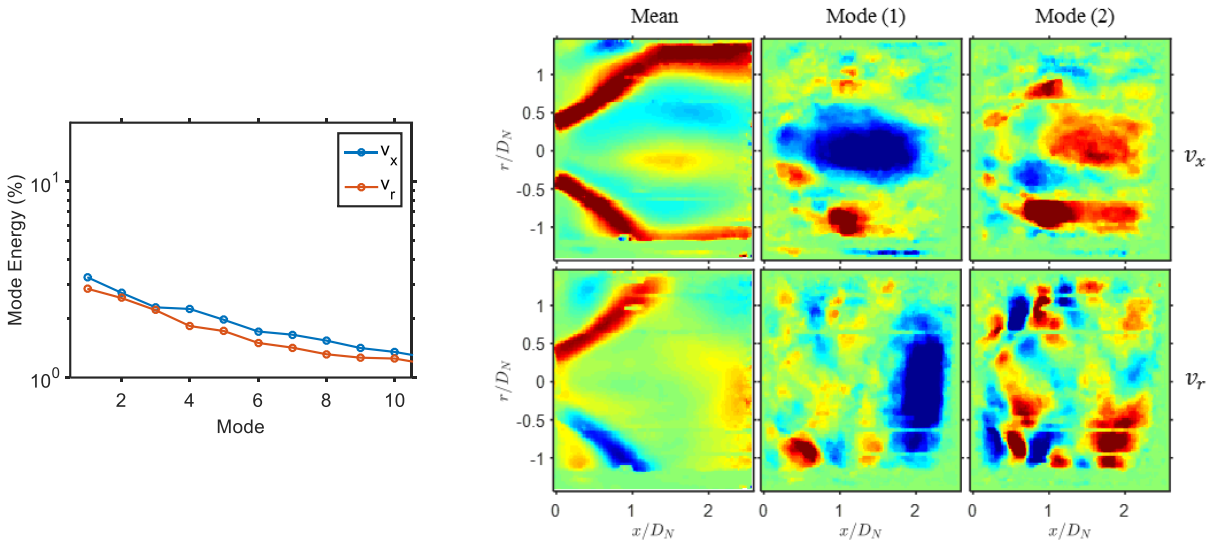

Figure 40. Mode energy contribution and three most energetic POD modes for case R1 reacting flow

First two modes contained most of the turbulent energy in the non-reacting flow, which is about 19% and 12% for each component. The first and the second POD modes are spatially correlated, from which can be interpreted as the dominant coherent structure. This coherent structure is related to the periodic shedding of the flow which appears to be related to PVC in a similar way as in TKE plots. This observation agrees with the previous results of POD analysis on non-reacting flow PIV measurement.

In the previously reported results, POD analysis of reacting flow was not reported. Figure 40 shows mode energy contributions and POD modes contours for reacting flows (R1). Reacting case (R1) was very stable condition with ϕ = 0.60. The first two modes contained about 5% of turbulent energy. POD modes shows random fluctuations due to small eddies at the flame front, and also measurement noise. Due to damped PVC and small energy contents of periodic structures in reacting flows, coherent structures was not captured even with this POD analysis. Most of other reacting flow cases showed similar results.

One exceptional reacting case was observed for R5 case (Figure 41), while most of the other reacting cases showed similar structures and energy contributions to R1 case. The total energy contribution is similar to non-reacting case, by looking at energy contents in mode 1 and mode 2 of axial velocity (v_x, blue in the mode energy plot). Peaks of these modes are located in the central recirculation zone in the POD mode plots. Periodic fluctuations of the flow in the recirculation zone formed dominant coherent structure. This unstable behavior could not be

noticed in the mean / TKE plots. Using POD analysis, the coherent structure inside central recirculation zone was revealed for a lean operation case.

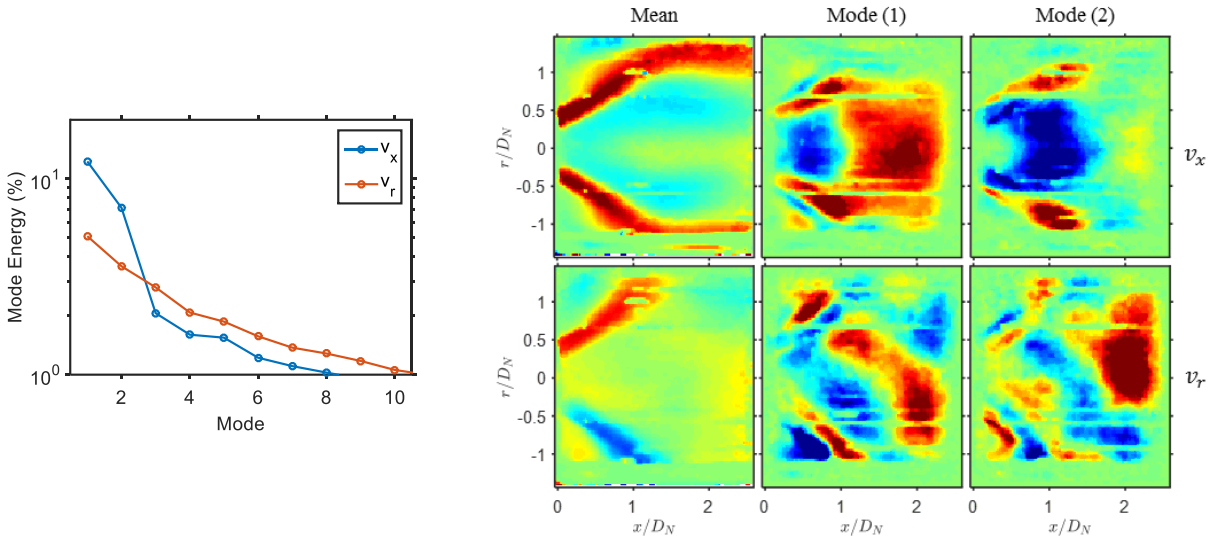

Figure 41. Mode energy contribution and three most energetic POD modes for case R5 reacting flow (lean)

In this report, POD analysis was used to investigate coherent structure by comparing reacting flow and non-reacting flow. Further attempts including phase identification and reconstruction will provide more temporal information of the reacting flows.

3.2.9 Uncertainty

The flowmeter for air flow provides 2.0% uncertainty. Airflow drift due to pressure oscillation from compressor on/off operation adds 1.4% of uncertainty at approximate period of 3 minutes. The overall uncertainty of air flow rate is 2.5%. The subpixel accuracy of PIV data processing is 0.1 pixels, which corresponds to < 0.7 m/s depending on the size of measurement plane. Flow rates were compared between two independent measurements by flowmeter and by axial component of PIV measurement. Under the assumption of axially symmetric geometry, integration of axial velocity profile and flowmeter reading showed 5.6% difference in average.

3.2.10 Summary and Discussion

A set of measurements was performed with a 2-D PIV system. Time-averaged flow velocity, vorticity and turbulent kinetic energy (TKE) were obtained from PIV data and flow structures under different conditions were compared. Jet impingement location on the liner wall was determined as well.

For reacting flows, cases of 4 Reynolds numbers, 4 equivalence ratios, 3 inlet air temperatures were selected to examine the effect of combustion operating conditions on the flow field structure. Flow structures observed in PIV measurement were significantly affected by reaction. Structures of non-reacting flow and reacting flow showed distinct structures. The flow structures were invariant with combustor operation variables for reacting flows when the geometry was fixed, because the flame shape and flow structure are functions of geometry such as swirl number and contraction ratio.

Main jet impingement location in the liner wall was one of the main focuses of the experiment. The impingement locations on the wall were experimentally found to be closer to the dome plate in case of reacting flows compared to non-reacting flows. This observation agrees with LES numerical simulation results known in the literature.

POD mode comparisons between non-reacting and reacting flows showed significant differences. Reacting flows under lean condition contained more coherent periodic fluctuation in the central recirculation zone, which was not observed in the mean flow field. From the POD analysis, it was found that the operation of combustor was very stable for most of typical reacting flow conditions for this particular swirler nozzle and combustor geometry. Comparing this result with pressure data will also be interesting.

CHAPTER 4. FLOW TEMPERATURE MEASUREMENT

This chapter reports experimental flow temperature measurements in a research combustor under reacting condition. Thermocouple scanning system was built and mapped the spatial temperature distribution on a 2-D plane for the swirl flow under reacting condition in an optical model gas turbine combustor. The probe was designed to be inserted into the model combustor from exhaust side opening. The measurement was conducted at methane flame stabilized with lean-premixed swirling nozzle inside an optical model can combustor rig. Features of premixed swirl flame were observed in the measurement. Non-uniformity of temperature profiles were observed at combustor outlet as well. The thermocouple measured temperature distribution was compared to an infrared radiation map measured with a thermographic camera. The experimental data can be used to validate CFD calculation, and also to understand flow structure and heat transfer in a swirl type combustor. The result shown for a particular swirl combustor is useful information to study the structure of swirl flames and associated heat transfer to solid surfaces.

4.1 BACKGROUND

Experimental measurements are essential to understand flow structure and heat transfer in a lean premixed swirl stabilized combustor. The study of flow field characteristics in reacting flow in such a harsh environment at high temperatures is very challenging. In combustor studies, accurately measuring experimental data is important especially for turbulent reacting flows, due to their inherent complexities. Numerical analysis of complex turbulent reacting flows is technically difficult, and the accuracy of characterizing such flows is limited compared to non-reacting cases.

Traditionally, thermocouple probes were used to measure to measure fluid temperature under reacting conditions in combustion researches [98]. In many applications in the industry, thermocouples are advantageous since they are simple, rugged, and inexpensive. Thermocouple technique is suitable for references to new techniques owing to their proven reliability and easier

access. Appropriate selection can be made from wide temperature ranges from various materials for high temperature environment such as in combustors. PtRh/Pt (Type-B) thermocouple is one of common high temperature thermocouples. In this chapter, homemade scanning thermocouple probe measurements are presented. Practical strategies for how to build the probe and to acquire data are also provided.

4.2 Experimental Setup

4.2.1 Scanning Themocouple Probe

A home-made probe was designed to be inserted into the model combustor from exhaust side opening. Type B (PtRh/Pt) thermocouple wires were used for this setup which can measure 1700 C at maximum. The length of the thermocouple ceramic insulation rod was about 45 cm (18 inches) from the tip to the connector. And the rod was mounted at the tip of an end of a 1 m long steel rectangular tube for extended reach. The steel support was installed on a 2D traversing stage system. The setup was made to avoid damage during the measurement. Hot burnt gas flows to the exhaust side opening where the probe setup is located. Exposure to flow at high temperature easily breaks the mounting structure of the thermocouple probe if it is not made with proper high-temperature material. Thus, the thermocouple connector side has to be protected by blocking heat transfer from surrounding to the connector with an insulation box. The box was made with ceramic tiles, and zirconia paste which can sustain at higher than 1200 °C. The enclosed connector mount inside an insulation box could stably secure the thermocouple.

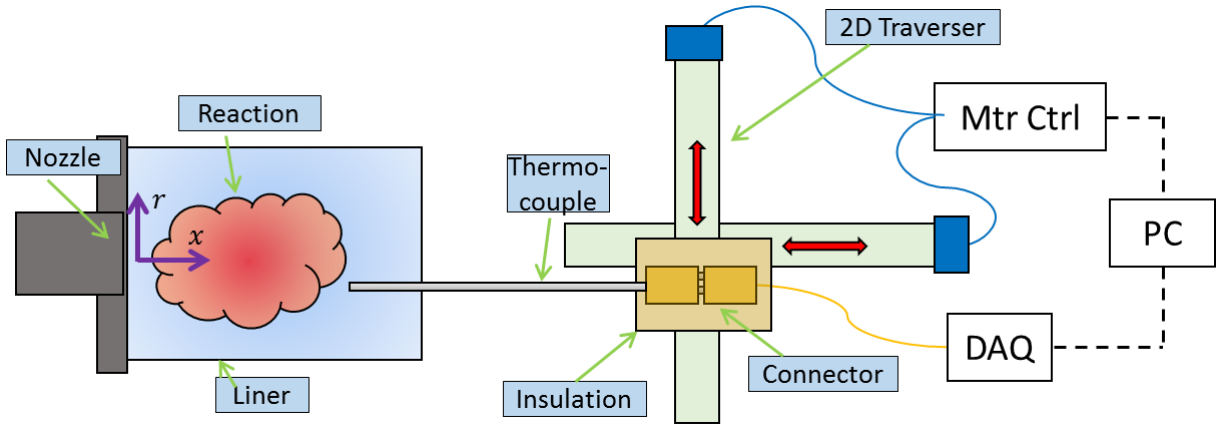

Figure 42. Themocouple scanning probe setup in reacting flow

Air cooling of the connector is also necessary to prevent the thermocouple junction temperature from rising. According to Seebeck effect principle, two different type of material of thermocouple generates a voltage signal proportional to the temperature difference between two ends. For type-B thermocouple, reference junction location is at thermocouple wire connection to copper extension wire. If the reference junction temperature rises more than 200 °C, about 3% error will be added to the measured temperature assuming the tip at 1200 °C. An air hose was connected to the insulation box and supplied cold air continuously to cool down the thermocouple connector and the insulation box. In this way, maximum reference temperature was lower than 200 °C during the measurement.

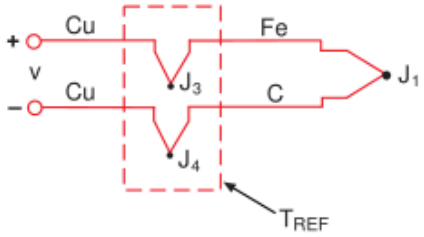

Figure 43. Example of copper wire thermocouple extension
(cf: Thermocouple used in this research is not this type)

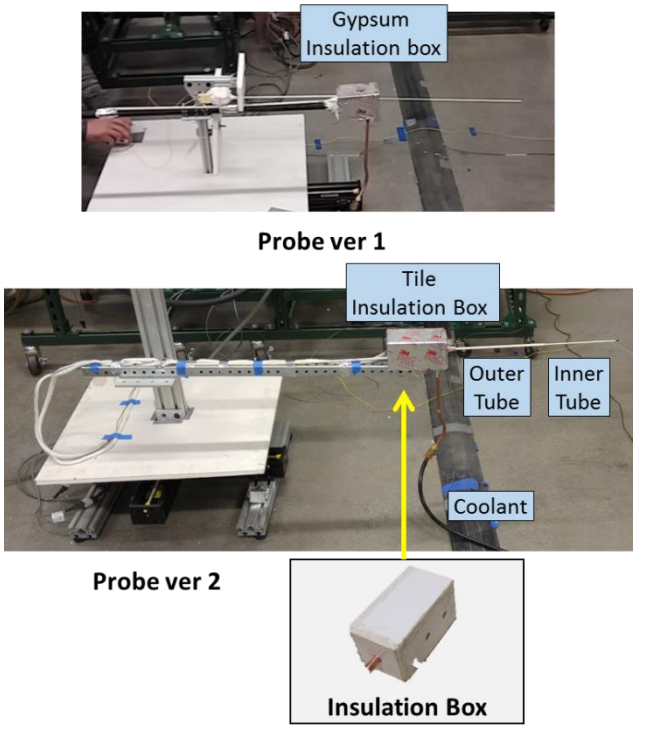

Figure 44. Thermocouple probe with 2D traversing stage

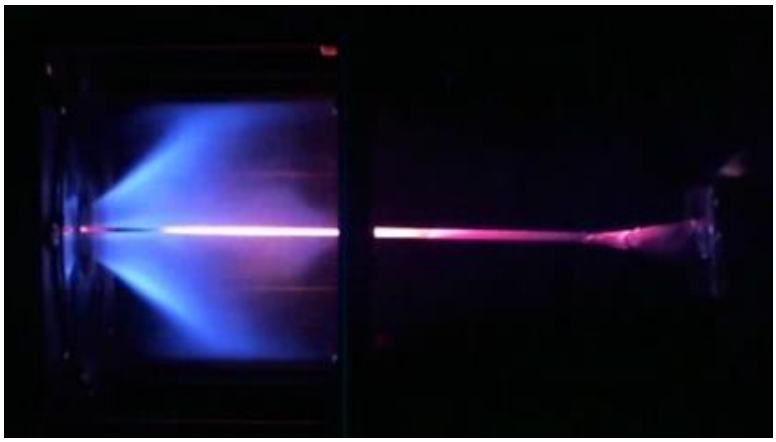

Figure 45. Thermocouple inserted to optical combustor during temperature measurement

4.2.2 Automated Data Acquisition

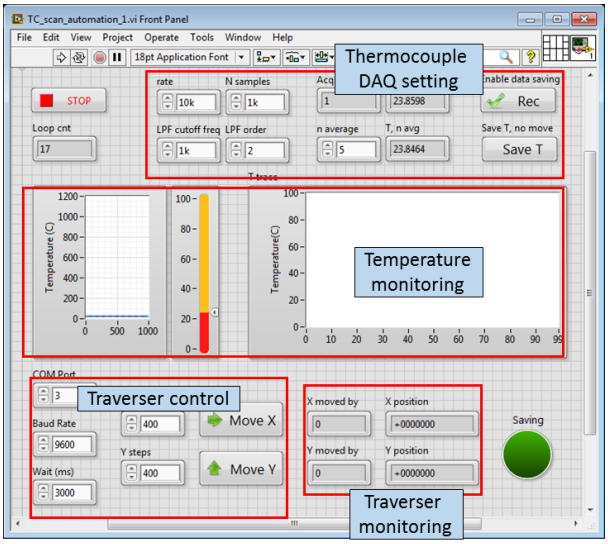

Figure 46. LabVIEW application (virtual instrument) for traverser control and thermocouple acquisition

A custom integrated LabVIEW application operated motor controller and acquired thermocouple data. To measure spatially resolved temperature, the linear stage system moved the position of the probe by a distance while the rig is operated with flame. This capability enabled the test fully operable from a remote location. Spatial resolution determined the distance of each motion. The total duration of operation was limited to about 2 hours by our current fuel supply system. Optimum resolution of scan was selected by trade-offs. A USB thermocouple data

acquisition device from National Instrument TC01 was connected to the extension wire from the probe. Three sets of samples were acquired at each point at 2 Hz. Data was saved when the standard deviation of samples was less than the threshold value (typically 0.5%) to automatically find equilibrium state of the probe tip temperature. After data saving, the thermocouple moved to next location in the radial direction. The process was repeated at the different axial location.

4.2.3 Combustor Operation

For all temperature field measurements reported herein, combustor was operated at one typical combination of set points which is at Reynolds number 50000, overall equivalence ratio 0.65 and pilot fuel split ratio 6-7%. Air split ratio between the pilot nozzle and annular main nozzle is not designed to be controlled by the operator. It is known that a few percent of air flows through the pilot nozzle. For thermocouple measurement, the liner and transition piece were disconnected during thermocouple scanning in the primary zone.

4.3 Combustor Exit Temperature

Radial temperature distribution was measured at different axial locations in transition piece. Flow temperature coming out from the transition piece is important design factor of combustor because it is closely related to turbine inlet condition. The capability of measuring accurate flow temperature in our test rig will also be helpful in the future for a more detailed study about geometry effect to combustor characteristics.

Five axial locations from A (x/D_c = 1.64) to E (x/D_c = 3.34) were selected as labeled in Figure 47. The axial distance was measured with respect to the fuel nozzle location. The length of our combustor was about x/D_c = 3.3 at the exit of the transition piece.

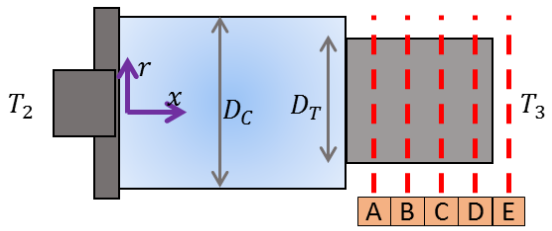

Figure 47. Combustor outlet temperature profile measurement

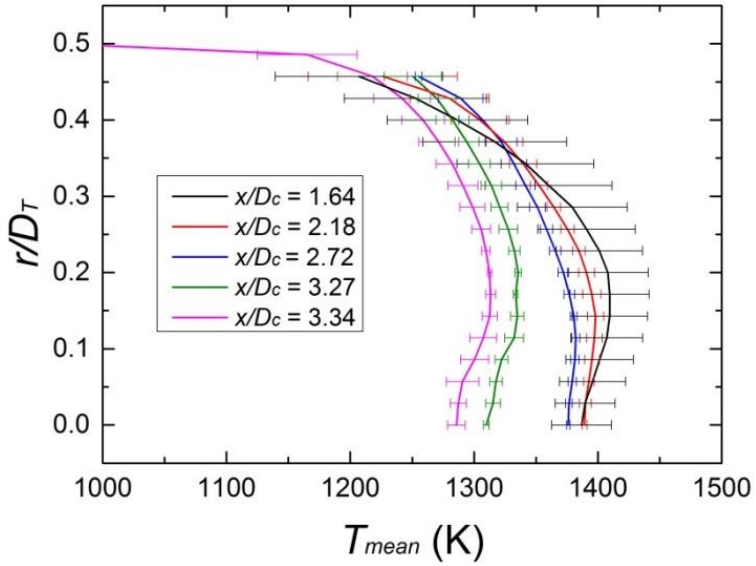

Figure 48. Radial temperature profiles of reacting flow at combustor exit

Measured radial distribution was shown in Figure 48. The black curve which was measured at the closest location from the nozzle showed highly non-uniform temperature profile. Peak temperature was found at $r/D_T = 0.17$. Lower temperature at the center $r = 0$ might be caused by an error from slight reference temperature increase. Flow temperature was measured until $r/D_T = 0.45$. The temperature at the outer region was lower than the center. A possible explanation might be heat transfer to liner/transition piece wall and corresponding, although the solid walls were not actively cooled. Inner recirculation might also contribute to non-uniformity. Burnt hot gas from the conical flame recirculates to the center as the flow moves to the downstream. More uniform radial distributions were observed at the downstream locations due to continuous mixing in the combustor, as well as reduced swirl.

Bulk averaged temperature was calculated under the assumption of ideal axisymmetric distribution and uniform density using the measured profiles at each axial location. The average temperature did not significantly vary along the axial locations at 1300 K. Non-symmetric temperature, and non-uniform density/composition are sources of error.

Pattern factor is widely used to study the durability of hot sections downstream of the combustor. In this study, extended definition of pattern factor was used to compare the degree of non-uniformity of the temperature profiles. Pattern factor is defined as Equation 19 where T_2 is combustor inlet temperature.

$$\text{Pattern factor (PF)}: \frac{T_{max}-T_{mean}}{T_{mean}-T_2} \quad (19)$$

The pattern factor was measured inside combustor was shown in Figure 49. T_{mean} is bulk mean temperature at each axial location. As location moved downstream, the pattern factor decreased monotonically from 0.1 to 0.04. The pattern factor is known to be a function of axial length, liner diameter and pressure-loss factor. The relation to the axial length is shown in this result for this type of swirl combustor.

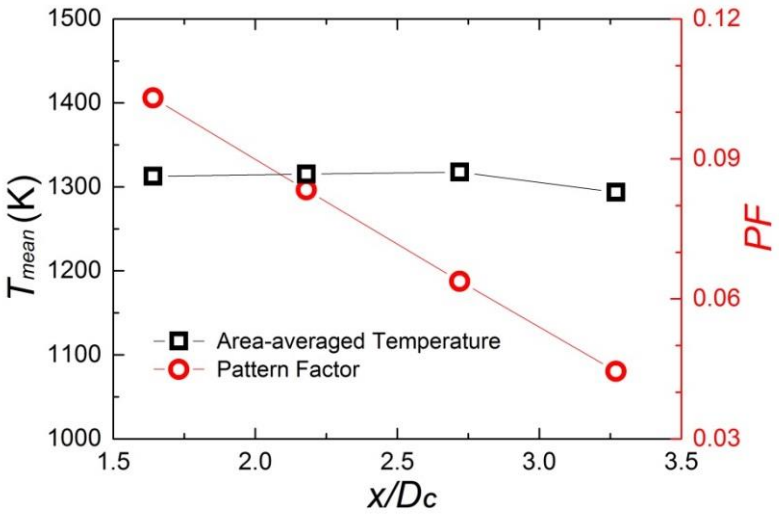

Figure 49. Mean temperature and pattern factor at transition piece

4.4 PRIMARY ZONE TEMPERATURE

4.4.1 Axial Direction Linear Scan

Temperature distribution was measured with axial direction traversing in combustor primary zone. Radial locations are chosen at the center, half liner radius and near the wall. Length scales are dimensionless with respect to fuel nozzle diameter. The inner radius of tubular liner was 1.45 D_N.

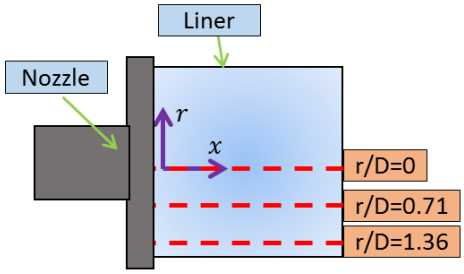

Figure 50. Axial line temperature profile measurement

Figure 50 shows three axial temperature profiles at different radial locations. The maximum and minimum temperature were measured at the half radius (r/D_N =0.71). The lowest temperature was about 400 K, which is close to the fresh air-fuel mixture. The location of (r/D_N = 0.7, x/D_N = 0.4) was close to the nozzle. The peak temperature of 1600 K was found at 0.3 D_N downstream of lowest temperature location. Most of the heat is released from a chemical reaction at the flame front which lies on the shear layer between the fresh mixture and recirculating hot gas. Location of highest temperature increase (r/D_N = 0.7, x/D_N = 0.6) agrees with previously measured flow field. Sources of mismatching of flame front location are thermal expansion of probe and downstream geometry effect on flow field structure. There are sections of different profile features. First is low temperature section (1000-1100 K) at $0 < x/D_N < 1$. Second section shows increasing temperature at $1.1 < x/D_N < 1.8$. Last high-temperature section (1300-1400 K) was found at $1.8 < x/D_N$.

This thermocouple measured temperature profiles can provide insights on the driving mechanism of convection heat transfer. The previous experimental study in the same swirl combustors reported the flow velocity characteristics and heat transfer. Unlike uniform temperature flow, reacting flow in the combustors shows strong non-uniformity. As in Figure 10, temperature ranges more than 400 K at near wall. This non-uniform flow temperature can significantly contribute to the convection heat transfer to the liner wall.

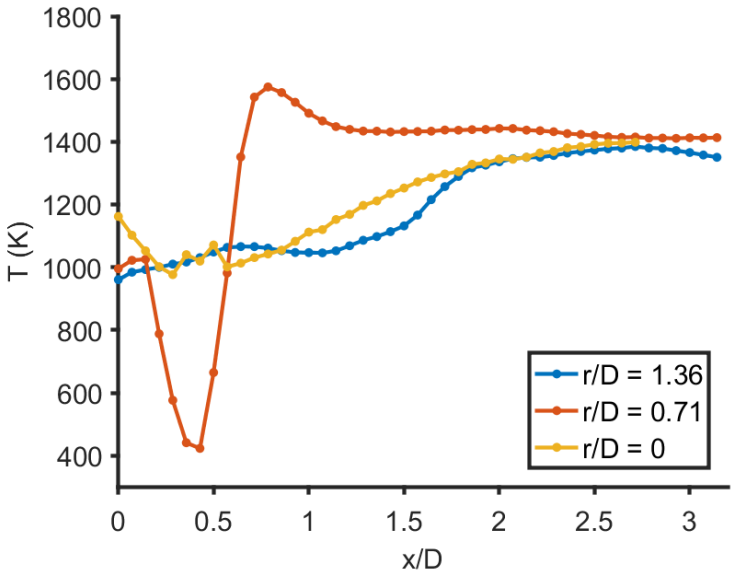

Figure 51. Axial profile of temperature of reacting flow

4.4.2 2-Dimensional Map

A complete 2-D mapping of reacting flow temperature was conducted at the same combustor operating conditions. Number of nodes are 320 in total. Covered area was within $0 < r/D_N < 1.36$, $0.14 < x/D_N < 0.29$ region. Figure 52 shows the area of measurement.

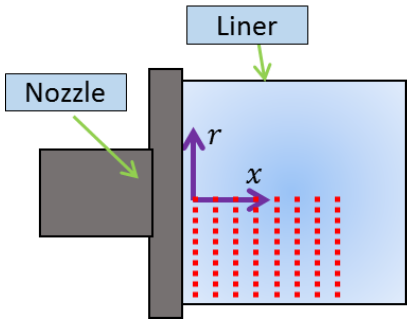

Figure 52. Axial-radial plane temperature measurement

Selected 6 out of 20 lines of axial profiles are shown in Figure 53. Radial profiles are shown in Figure 54 in a similar way. Same features were observed as in previous axial line measurement. Maximum and minim temperature are almost the same as 400 K and 1600 K. Propagating main jet flow was noticeable in radial profiles. The jet impingement location on the wall seems to exist between $1.1 < x/D_N < 1.4$. This observation agrees with flow field result.

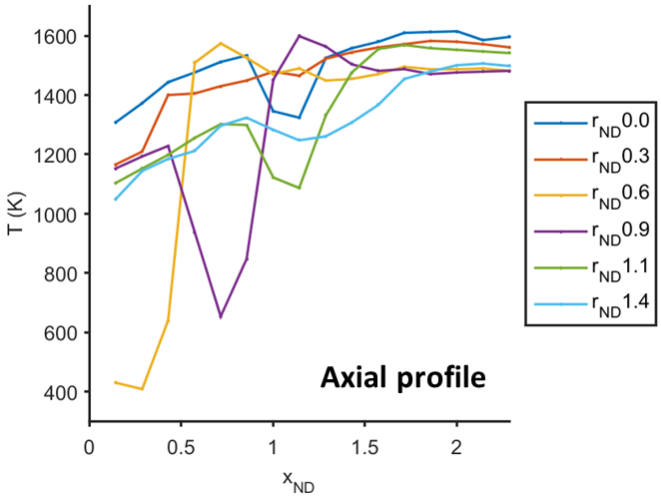

Figure 53. Axial profile of temperature of reacting flow

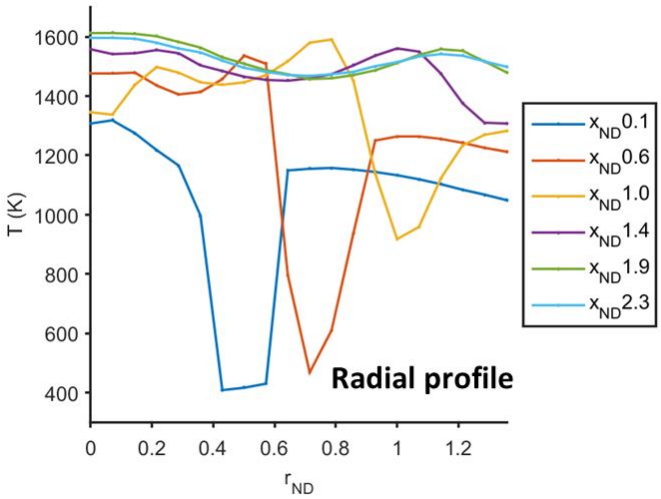

Figure 54. Radial profile of temperature of reacting flow

Temperature distribution in 2D map is plotted to help visualization of temperature field. Figure 55 is contour plot of raw data in 16 ×20 resolution. Blue region of low temperature is the fresh fuel-air mixture incoming jet from the annular main nozzle. The jet forms a cone before the jet impinges on the liner. The flow impinges on the wall at an angle where expected impingement location is at $x/D_N \sim 1.1$. As the flow approaches the wall, the temperature increased due to reaction. The flow temperature in the outer recirculation zone is lower than the other area due to quenching and heat loss.

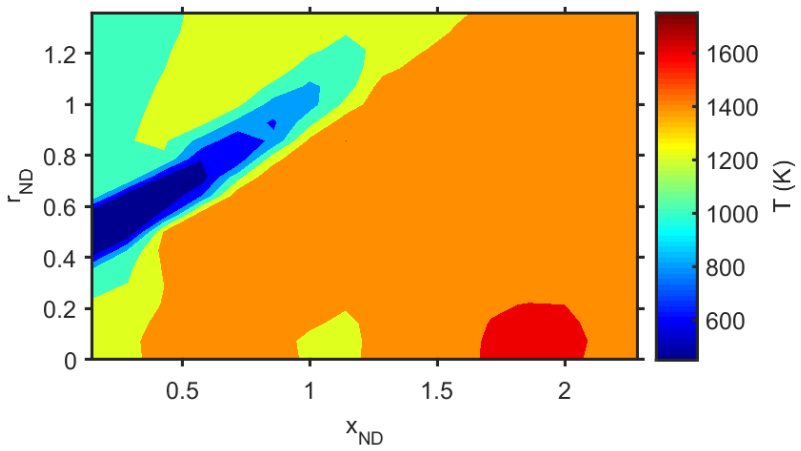

Figure 55. Radial-axial plane temperature distribution in reacting flow

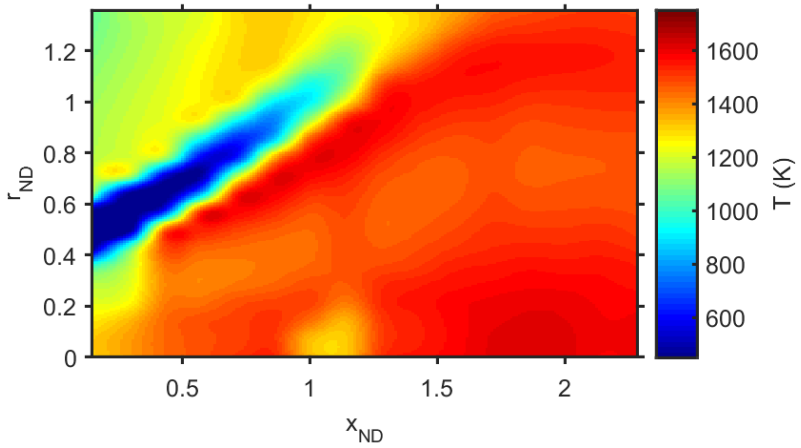

Figure 56. Interpolated radial-axial plane temperature distribution in reacting flow

4.4.3 Comparison with CFD

Figure 57 is numerical simulation result from the previous work [52]. The temperature of corner recirculation zone (100K-1200 K) is lower than that of CFD (1500-1700 K). This seems to be caused by ideal heat transfer condition at the boundary of the CFD, which is not easy to measure in the real world. If CFD utilizes measured heat transfer data as a boundary condition, more accurate simulation will be achieved.

The conical shape of main flame jet agrees for both experiment and CFD. However, angle of main jet flow shows small difference. It was reported from our team that the downstream geometry affects the size of central recirculation zone and shape of the conical mainstream jet. Due to the limitation of intrusive type of temperature measurement technique using thermocouple

probe, it might not possible to repeat temperature measurement with different combustor downstream geometry. This effect can be studied further, with non-intrusive techniques, such as optical flow temperature measurement.

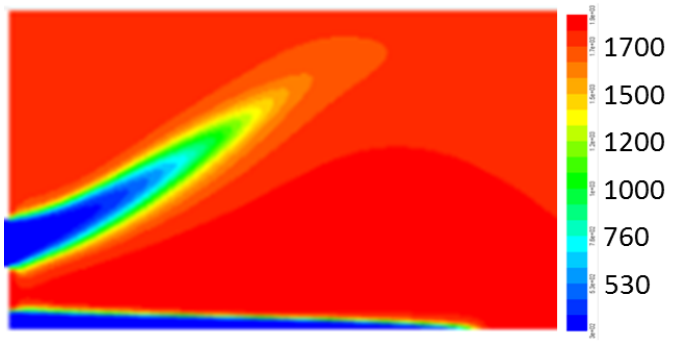

Figure 57. Radial-axial plane temperature from CFD result for comparison [52]

The flow temperature field agrees with the flow velocity field in terms of geometrical structure and quantified jet impingement location. Interpolation was applied to better visualize the raw data as shown in Figure 54. Roughly speculated extension of low temperature jet flow lies near the flow impingement location at $x/D_N \sim 1.1$. Highest temperature was observed on inner shear layer. There is smaller peak temperature on the outer shear layer as well. It is noted that heat release without visual wavelength light occurs on the outer shear layer, because luminous flame was not observed on the outer shear layer for this combustor operation condition.

4.5 MEASUREMENT UNCERTAINTY

The effect of other sources of error (radiation, conduction) are shown on the Table 4. The equations followed standard procedure of gas temperature measurement found in a paper written by Moffat [98]. The major sources of error are radiation error (11.1 K) and reference junction error (19.2 K).

The reference junction error is caused by increased temperature of the thermocouple reference junction. The junction is reference for the tip temperature. Even though the junction is protected with an insulation box and active air cooling, enormous amount of heat transfer from surrounding increases the temperature. The increased junction temperature reduces temperature difference and voltage reading at the DAQ. Most of time during the measurement, the junction

temperature was maintained less than 157 °C. The corresponding amount of error is calculated as 1.2%. The maximum junction temperature was 200 °C only for a short time, which can contribute maximum 3% bias error reducing the measurement value.

Table 4. Uncertainty of thermocouple measurement. Equations are from [98]

Source	Calculation	Estimated Max. Error
Conduction error	$E_C = \frac{T_r - T_M}{\cosh L(4h_c/dk_s)^{1/2}}$	0.15 K (at 1600 K)
Radiation error	$E_R = \frac{K_R \sigma \epsilon A_R (T_J^4 - T_W^4)}{h_c A_c}$	11.1 K (at 1600 K)
Transient error	$E_{tr} = \tau \frac{dT_J}{dt} = \frac{\rho c d}{4h_c} \times \sqrt{6}(STD)$	0.0016 K (at 1600 K)
Thermocouple error		±0.05K
Reference junction error	Maximum ref. jct. T : 430 K Voltage error: 0.1 mV / 8.2 mV	1.2% ~ -19.2 K (at 1600K)

Transient error was estimated by traversing the thermocouple multiple times in a steady state flame. Scanning was performed in two directions and the mean values and deviations are shown in Figure 58. There is notable hysteresis depending on scan direction. This means that thermal equilibrium of the probe tip could not perfectly be accomplished. Nevertheless, the true value is between the error bars which is top and bottom bounds of the true temperature (excluding other sources of error than time response). Transient error is within 10% for the most of points. A peak transient error located near inner shear layer where the temperature gradient is the highest.

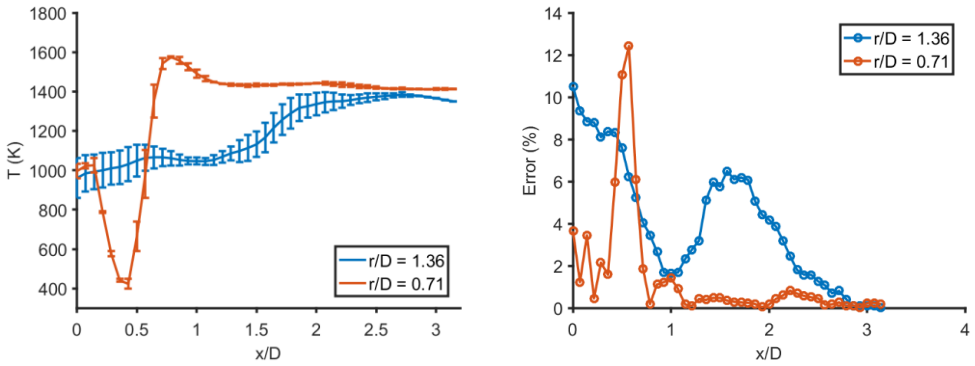

Figure 58. Estimated error of thermocouple measurement

4.6 SUMMARY AND DISCUSSION

Flow temperature in a lean-premixed swirl combustor was measured with a scanning thermocouple probe. A home-made thermocouple scanning probe setup was described. Radial profiles were measured in a transition piece and at the combustor exit to determine pattern factor. The relation of calculated pattern factor to the axial length is shown. The pattern factor at the exit was 0.04. Axial temperature distribution was presented inside the primary zone of the combustor. The temperature ranged from 400-1600 K in the combustor. The profile near wall was 1000-1400 K, which shows significant contribution of the flow temperature to the convection heat transfer to the liner wall. This can be studied further, with non-intrusive techniques, such as optical flow temperature measurement. Further comparison with PIV measured flow field will make more comprehensive data about the swirl flow in this model combustor.

Flow temperature directly impact on the convective heat transfer. The results shown here can be used for heat transfer analysis on the combustor walls. Insights about the 2D distribution of the temperature compared with flow structure helps understanding behavior of the reacting flows. Moreover, the near wall temperature profile can be used to quantitatively validate models for convective heat transfer at the liner wall.

CHAPTER 5. FLAME INFRARED RADIATION MEASUREMENT

This chapter describes a proposed diagnostic concept of flame infrared radiation measurement. Infrared radiation measurement was demonstrated for a model gas turbine combustor. An IR thermographic camera and a filter glass were used to capture the infrared signal from the flame through the glass liner during reacting condition. Schott KG glass filtering enabled flame measurement through a quartz combustor wall within wavelength of 1-2.7 μm. Feasibility of the technique and potential value for combustor systems are shown in this work. Flow characteristics in the infrared measurement agreed with flame luminosity observation. Features including double shear layers, fresh mixture flows could only be captured with infrared measurement.

5.1 BACKGROUND

The study of flow field characteristics in reacting flow in a harsh environment at high temperatures is very challenging. Experimental data are important in combustor studies especially for turbulent reacting flows, due to their inherent complexities. Numerical analysis of complex turbulent reacting flows is technically difficult, and the accuracy of characterizing such flows is limited compared to non-reacting cases. Measuring infrared emission of reacting flow with an infrared thermographic camera can provide information about thermal properties inside a model combustor under reacting conditions.

Measuring infrared radiation is a non-intrusive time resolved technique which does not affect the flow field compared to a probe based technique. The proposed experimental setup is relatively simple and inexpensive compared to other optical measurement techniques such as laser induced fluorescence (LIF), Rayleigh scattering, Raman scattering, thermographic phosphor etc. [87,88,99,100]. Infrared measurements of flame are available in the literature to correlate with temperature for laminar flames and sooty diffusion flames [101-105]. Their non-intrusive (or partially intrusive) capabilities are advantageous for high temperature field measurements. However, most of them require delicate alignments of complicated experimental setups, and good

understanding of theoretical backgrounds in optics, which are not always available except for optical diagnostics experts. Measuring infrared emission of reacting flow with an infrared thermographic camera can provide information about flow properties inside combustors during reaction in simpler way. By measuring infrared radiation, a non-intrusive time resolved technique can be achieved. Infrared measurements of flame are available in the literature to correlate with temperature for laminar flames and sooty diffusion flames [102-105]. Applying these techniques to turbulent flows within swirl stabilized gas turbine combustor is the focus of this work.

Optical windows are necessary to measure the reacting flows under realistic condition. Quartz glass (fused silica) for the window has high transmissivity in visible light range, however the transmissivity is low in the infrared range. Zinc-Selenide (ZnSe) is infrared transmissive window material, but it is significantly expensive compared to quartz glass. The proposed technique in this work utilizes quartz glass wall as a combustor liner. KG glass filters were installed in front of the IR camera lens to measure infrared radiation from the reacting flows. A similar technique was recently developed for wall temperature and heat transfer measurement on quartz liner using the same combustor test rig [84].

5.2 EXPERIMENTAL SETUP

The IR camera measured the signal from one side of the test section through the quartz glass liner. A FLIR SC6700 camera was used with a 3 mm thick Schott KG2 filter (Figure 59). The KG glass is a heat absorbing filter and can also be an optical short pass filter. The wavelength range of measurement was determined by the response range of infrared camera and absorption curve of quartz material. The camera sensor responds to infrared signal from a wavelength range of 1-5 μm. Infrared signals with wavelengths longer than 2.8 μm are blocked by the KG filter. Transmittance curves accounting for the material absorption and surface reflection are shown in Figure 60. Material property data was obtained from [106]. This filtering enables the camera to measure the IR signal through the quartz glass window.

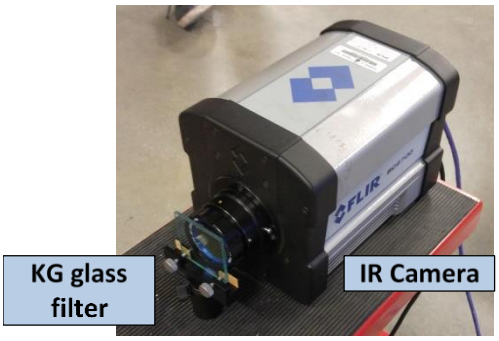

Figure 59. Thermographic camera and KG glass filter for flame measurement

Fused silica material typically does not show resonance bands at near infrared, but OH band of a small amount of water content (less than 5 ppm in GE 214 quartz) emits infrared longer than 2.8 µm at high temperature [107,108]. When the long wave quartz radiation is sufficiently blocked, the quartz is transparent in the camera view. Thus, the flame physically contained in the combustor can be measured without optical barriers in the measured wavelengths. Another advantage of using KG filter is to prevent saturation of camera sensor by reducing infrared signal strength.

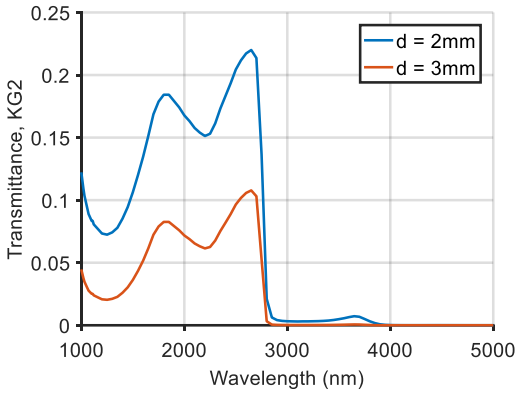

Figure 60. Transmission curves of KG2 glass filters with different thicknesses. [106].

Sources of optical radiation from chemically reacting flow can be soot particles or excited molecules or radicals [109]. Blackbody radiation from soot particle dominates in a rich flame with high carbon ratio in the fuel. For a land-based power generation gas turbine engine, lean and stable flame is required for higher performance and lower pollutant emission. Light radiations from molecules or radicals are in narrow bands, in a lean flame. Strong bands are commonly observed in ultraviolet and visible ranges, which are out of the measurement range of the infrared camera. The source of the infrared seems to be H_2O or CO_2 bands at the measurement range.

5.3 PROOF-OF-CONCEPT

A proof of concept measurement was conducted with a propane torch flame. TS-1500 low profile torch was used to form a flame. The flame was fuel lean without visible soot radiation. The camera measured infrared radiation from the flame through a quartz glass. Frame rate was 5 Hz and the data was averaged for 30 seconds. Infrared radiation from the flame dominated over radiation signals from surfaces and weak radiation was measured at metal part of the torch. Measured infrared emission and structures inside flame are shown in Figure 61. The filter reduced intensity of infrared radiation received by the camera. Measured infrared radiation distribution represents distribution of high temperature combustion product.

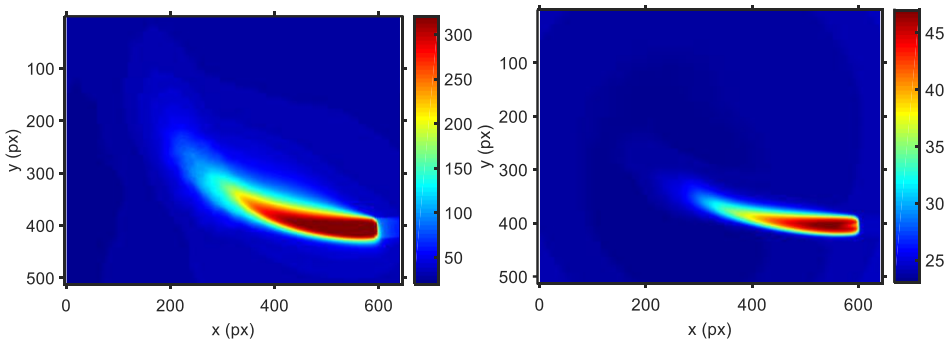

Figure 61. Proof of concept measurement with propane torch flame; (left) without filter (right) with KG2 filter. Color scales represent measured infrared intensity (a.u.).

5.4 COMBUSTOR FLAME MEASUREMENT

Figure 62 shows a typical RGB camera image of a flame in the model combustor rig. Flow direction is left to right. The fuel nozzle is installed at the center of a round dome plate shown on the left side. The main flame is anchored at the hub of the fuel nozzle as a cone. Burnt gas enters a transition zone on the right side, and then exits the combustor.

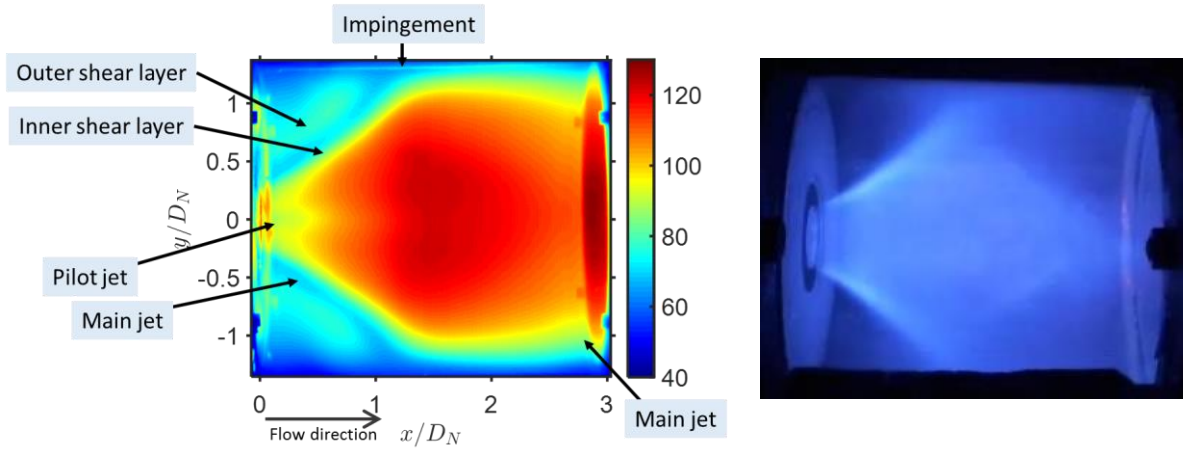

Figure 62. Averaged projection image of infrared radiation from reacting flow (a.u.) and RGB image of flame luminosity inside the combustor.

Measured infrared radiation of the reacting flow in the combustor is shown in Figure 62. Data was measured at 7.5 Hz rate for 60 s duration. Length scale was normalized with the fuel nozzle diameter (D_N). Flow characteristics observed in the infrared data agree with the flame luminosity in general. The main flame was observed as a cone, and strong intensity was radiated from the central recirculation zone. Radiation from corner recirculation zone was relatively weaker as expected from the characteristics of swirl flow.

There are several features observed from the infrared measurement that could not be seen in flame luminosity image in visible light. Two shear layers were observed from the infrared measurement. The layer between corner recirculation and incoming cold jet (x/D_N ~0.5, x/D_N ~ ± 0.8) was observed only in the infrared measurement and not visible in the regular image. Between those layers, fresh fuel air mixture incoming from the nozzle is shown as low signal gaps. Another relatively low intensity region was captured at the center near the fuel nozzle (x~0, y~0) due to fuel air mixture injected through a circular pilot nozzle at the center of the fuel nozzle hub.

5.5 ABEL TRANSFORMATION

The infrared radiation image was further reconstructed with Abel transformation. Infrared radiant energy density was spatially resolved, and inner structures of the reacting swirl flow were identified. The high density region was observed near flame front where recirculated flow is mixed with fresh mixture. Area of incoming mixture of main jet showed lowest density.

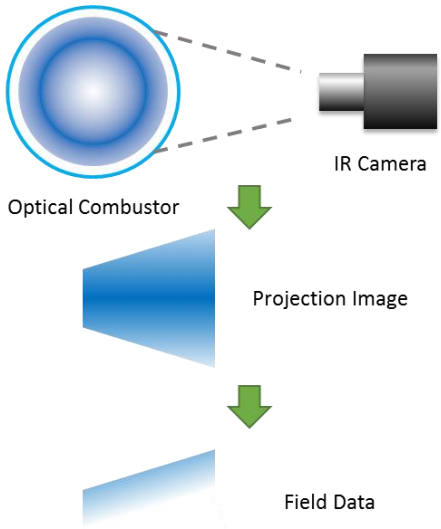

Figure 63. Reconstruction process from IR radiation projection image to field data

Assuming axially symmetric geometry, the data was further analyzed with a tomographic reconstruction. Abel transformation is useful technique to convert line-of-sight averaged projection images from axisymmetric objects to cross-section distributions at central axis. Similar techniques were applied to infrared measurements of various laminar flames [100, 102]. In this study, averaged symmetric image of a turbulent flame was reconstructed with Abel inversion.

The combustor is divided into concentric layers of different radiance densities ($\mathbf{X}_i$). A matrix (**A**) was obtained from path length segments ($l_{i,j}$) and radial location (r_i). Multiplication of inverse matrix to the line-of-sight averaged projection (**P**) gives radial distribution of radiant energy density (**X**).

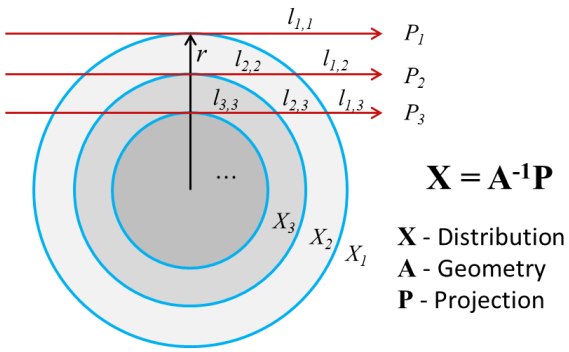

Figure 64. Principle of Abel transformation.

The reconstructed image shown on Figure 65 shows the infrared radiant energy density in radial axis. The inner structures of swirl flame are more distinct compared to the projection image. The most interesting observation is the flame front between incoming fresh mixture and central recirculation zone. It is shown as a high gradient curve starting from x ~ 0, r/D_N ~ 0.3 towards upper right direction, until impingement on the liner wall at x/D_N ~ 1.2, r/D_N ~ 1.4. The flame front divides the image into two zones, one with low radiation that includes incoming main jet and corner recirculation zone, and the other with high radiation at central recirculation zone.

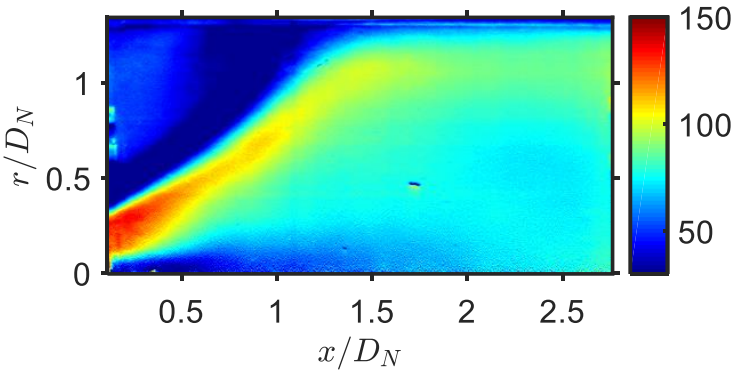

Figure 65. Reconstructed infrared radiant energy density (a.u.).

The highest density region was observed near the nozzle and lowest was at incoming fresh mixture at main jet. The high density region was located at where heat is transported from the flame front. The radiant energy density from the flame decreases as the flow moves to the downstream. On the other hand, total radiant energy increases due to increase in total volume along the radial axis. The density at the corner recirculation zone is very low, but higher than the incoming jet. Structure of the pilot jet at the center of the flame (r~0) is shown better than the projection. Comparison of the infrared radiant energy density with other diagnostic methods will help better understanding of the infrared diagnostics of turbulent reacting flow.

5.6 Effect of Equivalence Ratio

The reconstructed image on Figure 66 shows the infrared radiant energy density in radial axis. The highest radiation location is the flame front between incoming fresh mixture and central recirculation zone. The flame front divides the image into two zones, one with low radiation that

includes incoming main jet and corner recirculation zone, and the other with high radiation at central recirculation zone.

The radiant energy density were compared for three equivalence ratios of 0.60, 0.65 and 0.77 in Figure 66. The result is difficult to understand, because it is opposite from anticipation. The highest peak was found at low equivalence ratio. Area of high energy moved downstream with increase in equivalence ratio. Structures such as diverging angles, locations of flame front, size of recirculation zones, were invariant.

The equivalence ratio effect seems to have strong relations with optical emissivity of the partially transparent flow. This is more severe at the center location or near the axis. The most reliable information is infrared density near the wall. The reconstruction comparison on Figure 66 is showing that the near wall intensity does not vary a lot with different equivalence ratio. Details can be found in Figure 67 as well. Near wall intensity is quite different in the outer recirculation zone (x<1), but they are at similar level afterwards.

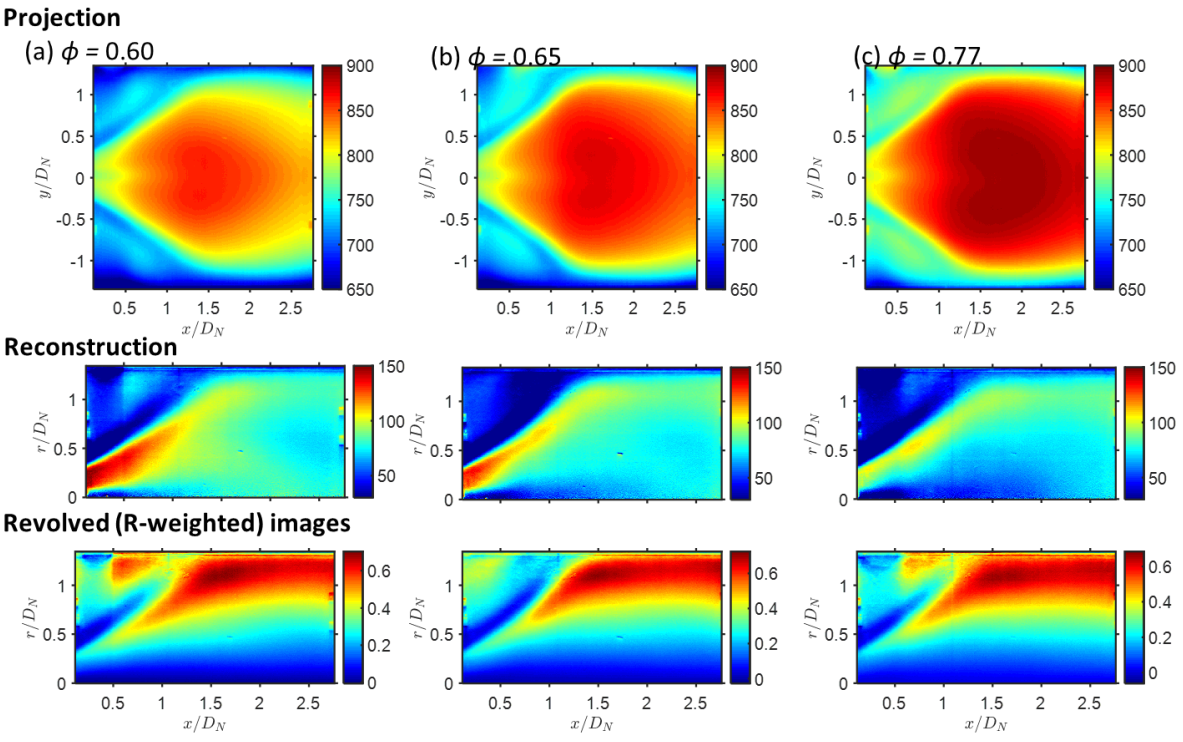

Figure 66. Reconstructed infrared radiant energy density (a.u.).

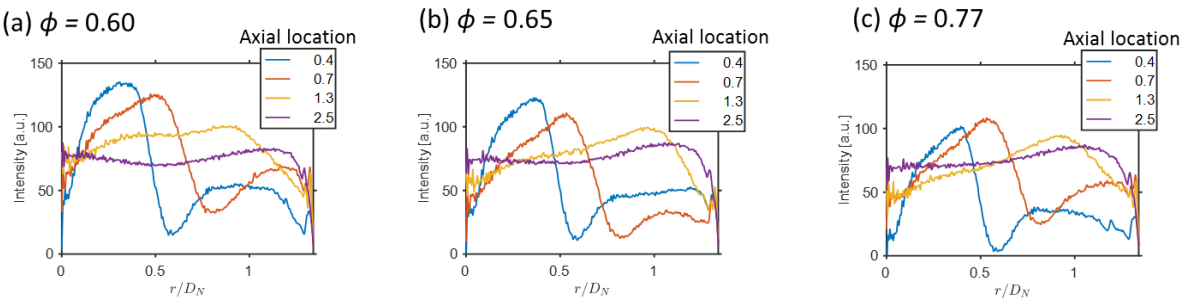

Figure 67. Profiles of reconstructed infrared radiation

5.7 SUMMARY AND DISCUSSION

A concept of infrared radiation measurement was demonstrated for a model gas turbine combustor. Initial experiments showed feasibility of the technique and potential value of similar measurements for combustor systems. Flow characteristics in the infrared measurement agreed with flame luminosity observation. Features including double shear layers, fresh mixture flows could only be captured with infrared measurement.

Abel transformation was applied to the measured projection. Infrared radiant energy distribution was spatially resolved, and inner structures of the reacting swirl flow could be identified. The high density region was observed near flame front where recirculated flow is mixed with fresh mixture. Area of incoming mixture of main jet showed lowest density.

Although the comparison shows this infrared measurements are not directly related to flame temperature or a particular flow property, this novel technique will be useful to investigate flow structures and information of reacting flow in gas turbine combustors and other high temperature flows.

Future study will focus on the analysis of the infrared measurement and comparison with actual temperature measurements. The emissivity of the partially transparent flow should be identified to correlate the infrared measurement to temperature field. If correlations can be found, the infrared technique will be more useful in the gas turbine research and other high temperature harsh environments.

CHAPTER 6. HEAT TRANSFER MEASUREMENT

This chapter covers liner wall heat transfer measurements focusing on the reacting conditions. The heat transfer measurement technique using infrared thermography was developed previously [84]. The heat transfer data was analyzed by a finite difference model. The results showed the promising capability of non-intrusive optical measurement of time-resolved liner heat flux and heat transfer coefficient distributions.

6.1 BACKGROUND

A technique to measure heat transfer with infrared camera was developed in this research group. The method was experimentally validated for non-reacting and reacting conditions in the combustor [84,90]. The new technique is able to measure the instantaneous (time-dependent) temperatures inner wall surface and outer wall surfaces. Numerical estimation of temperature profile yields time resolved heat transfer distribution using finite difference calculation with boundary temperature conditions from the measured data. Traditionally, inverse method was used in many works including experimental works using 3D heat transfer method [110-116]. The numerical technique used in this work is based on forward model, which is simpler than inverse calculation. However, there are not many cases where a time-dependent technique was applied to gas turbine research. A recent patent proposed a similar type of time dependent heat transfer method [117].

6.2 EXPERIMENTAL SETUP

The liner wall temperature was measured at inner and outer liner wall surfaces simultaneously. Two temperature profiles for inner and outer wall was acquired at different azimuthal location of the cylindrical quartz liner. To relate the two profiles in axial direction, an assumption of azimuthal symmetricity should be confirmed. The geometry was designed symmetrically, and the initial tests

of the technique validated the symmetric pattern of measured temperature. The inner and outer walls were coated with a high temperature black spray paint (Rust-Oleum®). The infrared emission from the paint surface is obtained with infrared camera to get the surface temperature distributions. A FLIR SC6700 camera was used, and the spectral range was 1-5 µm.

The liner wall temperature measurement setup of the combustor is shown in Figure 68. A single reacting case was selected (Reynolds number 50000, equivalence ratio 0.65 and pilot fuel split 6%). The inner wall and outer wall of the quartz liner was coated with flat black high temperature paint, and the outer wall was only partially painted so that the inner wall coating was visible from the outside. When the liner heated up, the paint emitted thermal radiation. The radiated energy at infrared wavelengths was captured with an infrared camera. Assuming the heat transfer was axisymmetric (verified by the temperature distributions observed), the inside and outside wall temperatures were measured simultaneously. As shown in Figure 68, only a portion of the outer liner wall was coated, and more than half of the inner surface was coated. In the measured temperature data, the outer wall temperature region is the area on the top of the contour.

The wall surfaces of quartz liner are coated with black spray paint. The inner wall is coated on the full area of the region of interest (ROI). The outer wall is coated only partially, covering upper half of the region. IR camera captures the surface temperature of inner wall coating and outer wall coating simultaneously.

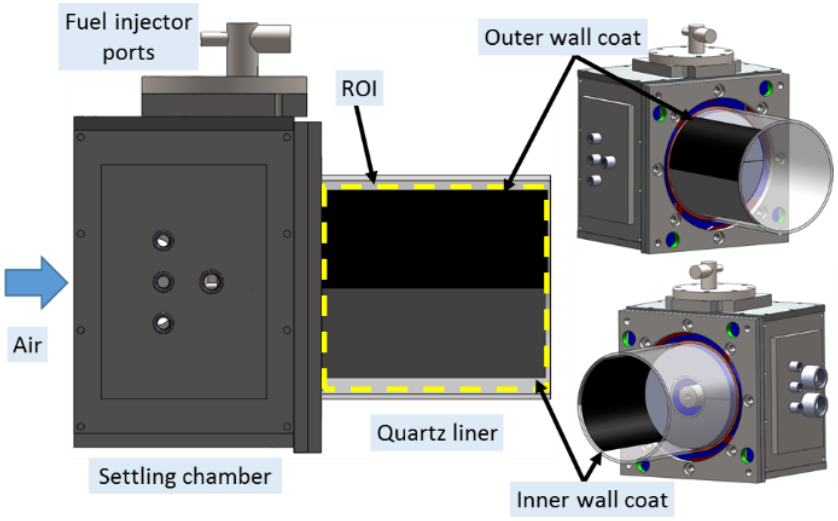

Figure 68. Schematic of wall temperature measurement with infrared thermographic camera. Region of interest (ROI) is indicated.

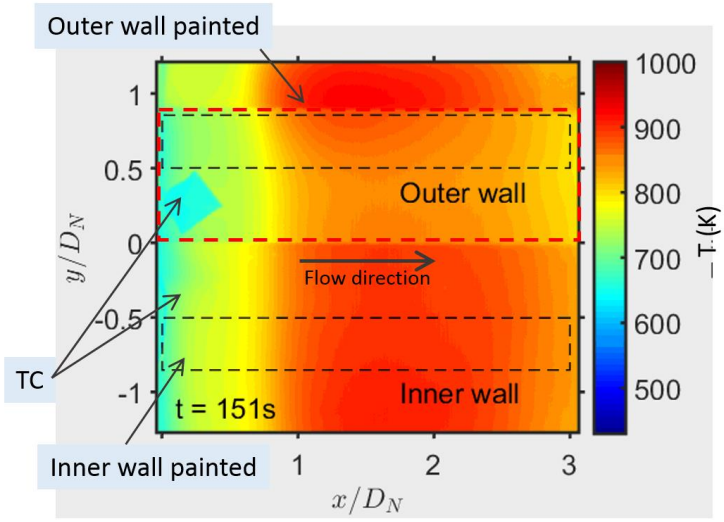

Figure 69. Region of interest in IR camera view

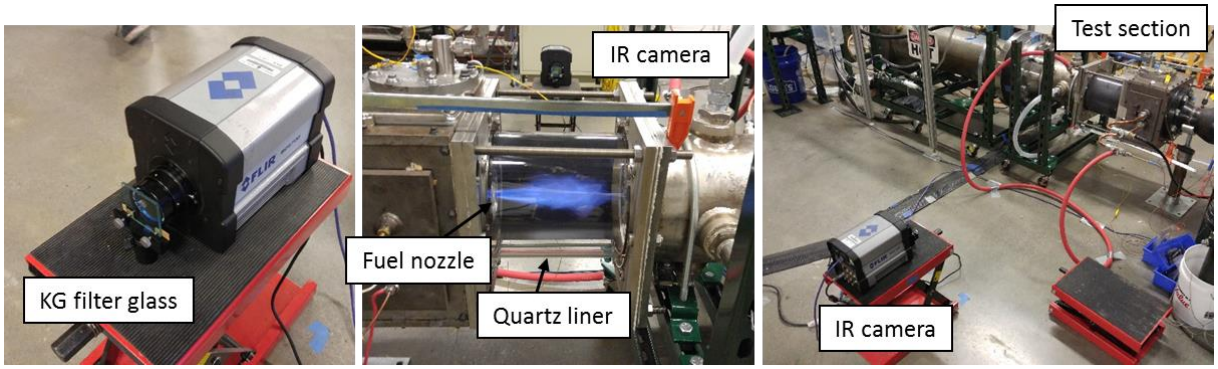

Figure 70. Heat transfer measurement setup, Left: IR camera with KG filter, Right: Test section with pilot flame

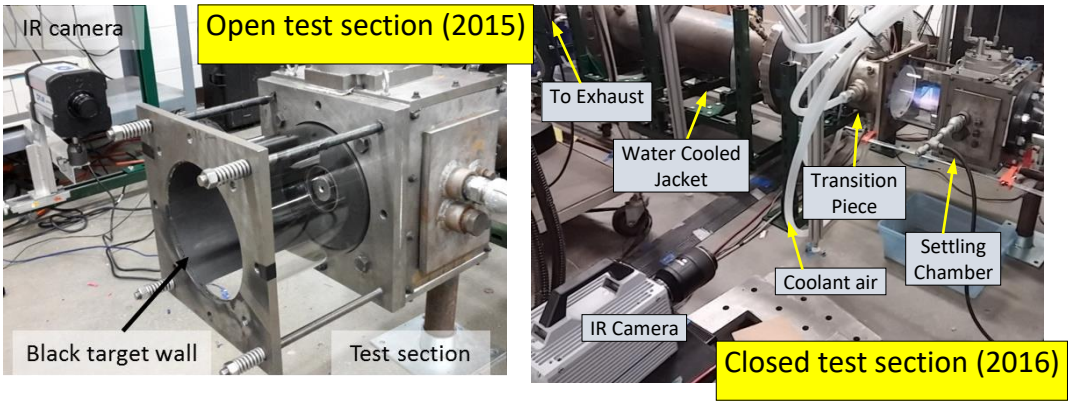

Figure 71. Photographs of previous IR measurement setup with open test section (left) and new IR heat transfer measurement setup with closed test section (right).

In the previous work, the setup was configured with open test section as seen in Figure 71. Continuing the established IR measurement technique, the technique for heat transfer measurement was applied to closed test section configuration. The condition is more realistic in this case considering effect of geometry on the flow. Combustor operating parameters are set to the same values as typical case of the PIV flow field experiment, and they were maintained at constant.

6.3 Infrared Liner Temperature Measurement

An infrared thermographic camera (FLIR SC6700) was used to measure the combustor liner temperatures at the inner and outer walls of the liner. A Schott KG2 glass with a 3 mm thickness covered the lens of the IR camera to remove the quartz liner absorption and emission signal. The IR camera has an spectral response range from 1 μm to 5 μm, and the KG glass filter absorbs 2.8 μm to 5 μm. Material property shows that the quartz glass is transparent (without absorption or emission) in 1 μm to 2.8 μm range, which was used for the inner wall and outer wall temperature measurement. Calibration of the IR data to wall temperature was separately done with a thermocouple measurement. Further details of the measurement technique, calibration of the temperature, and the effectiveness of the KG glass to block the emission from the quartz liner are discussed in [84,90].

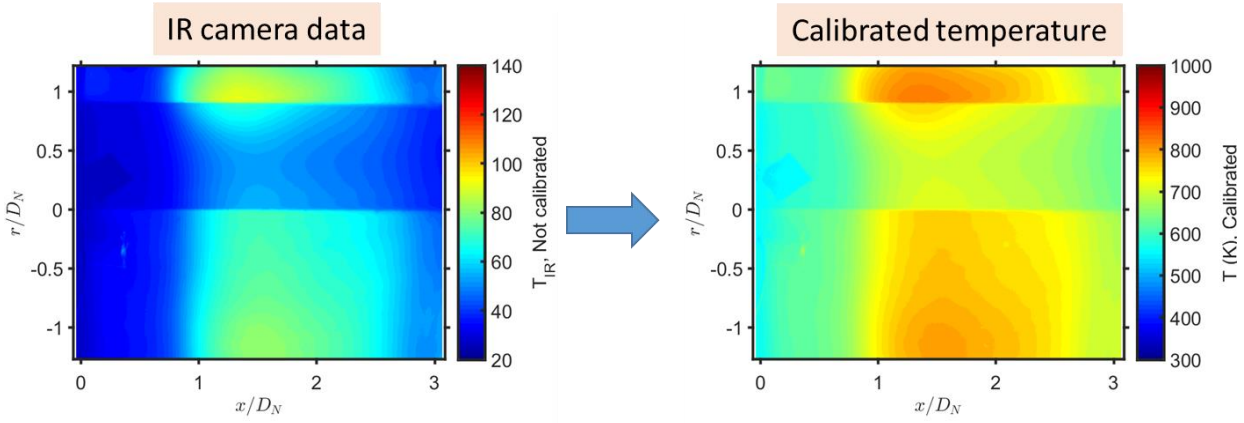

Figure 72. Example of IR camera data calibration

6.3.1 Liner Inner/Outer Wall Temperature

Figure 73 shows the infrared derived surface temperatures on the liner wall. Initially there was a pilot flame. The main flame was ignited at $t = 0$. The temperature increase was observed with good agreement with azimuthal symmetricity. The peak temperature band was observed. The marked locations on the figures show the area used for averaging the results in the radial direction. The data acquisition was continued until the liner temperature is almost at steady state.

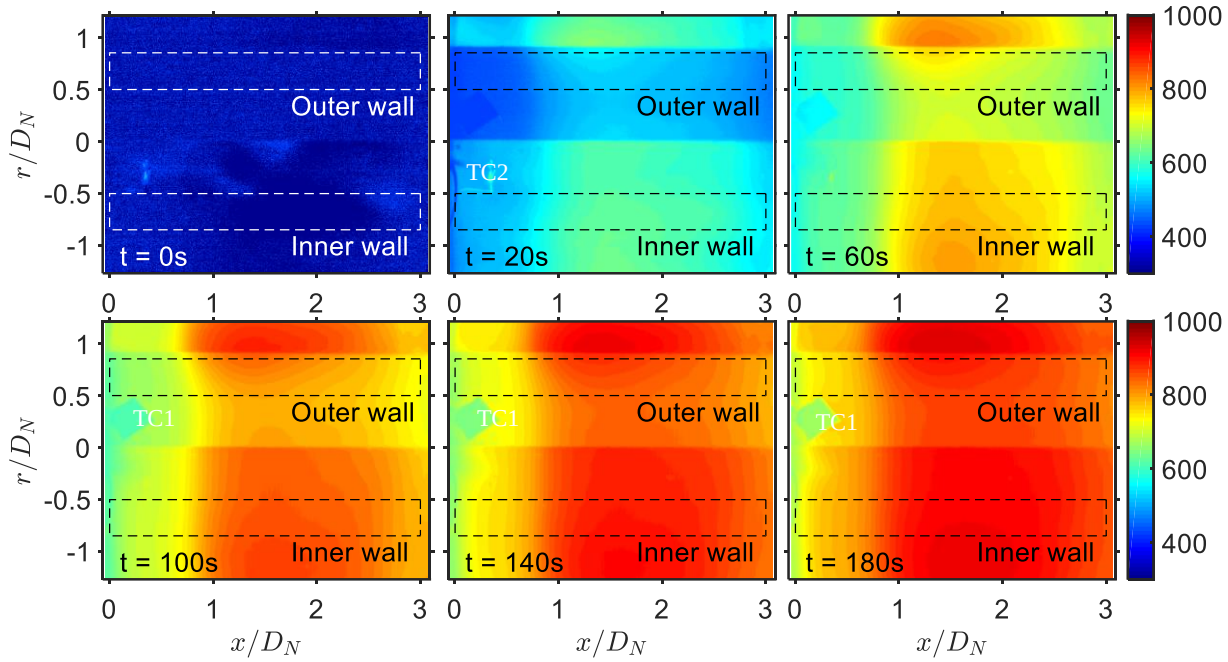

Figure 73. Calibrated liner temperature field (color scale in K) measured with infrared camera, at outer wall ($0<r/D_N<0.9$) and at inner wall ($r/D_N<0$). Dashed line rectangles show regions of interest for inner wall and outer wall. TC1 and TC2 labels indicate thermocouple locations attached on liner walls.

The rate of temperature increase was not uniform, nor constant. Figure 74 shows temperature profiles at the inner wall and outer wall of the quartz liner based on the IR camera data shown in Figure 73. Regardless of the shape of the profile at different times, peak temperature locations were constant at about $x \approx 1.5D_N$ in the axial location, which is $0.3D_N$ downstream of the flame jet impingement location. A possible explanation for the increased liner temperatures downstream of the location where the maximum convective heat transfer coefficient is expected (at the impingement location) is that the temperatures at the downstream annular flame jet (fully reacted) are presumably higher compared to the temperature close to the flow impingement point.

On the corner recirculation zone upstream of the impingement location, the lower flow temperature and the relatively lower heat transfer coefficients causes the slower temperature rise in the liner wall.

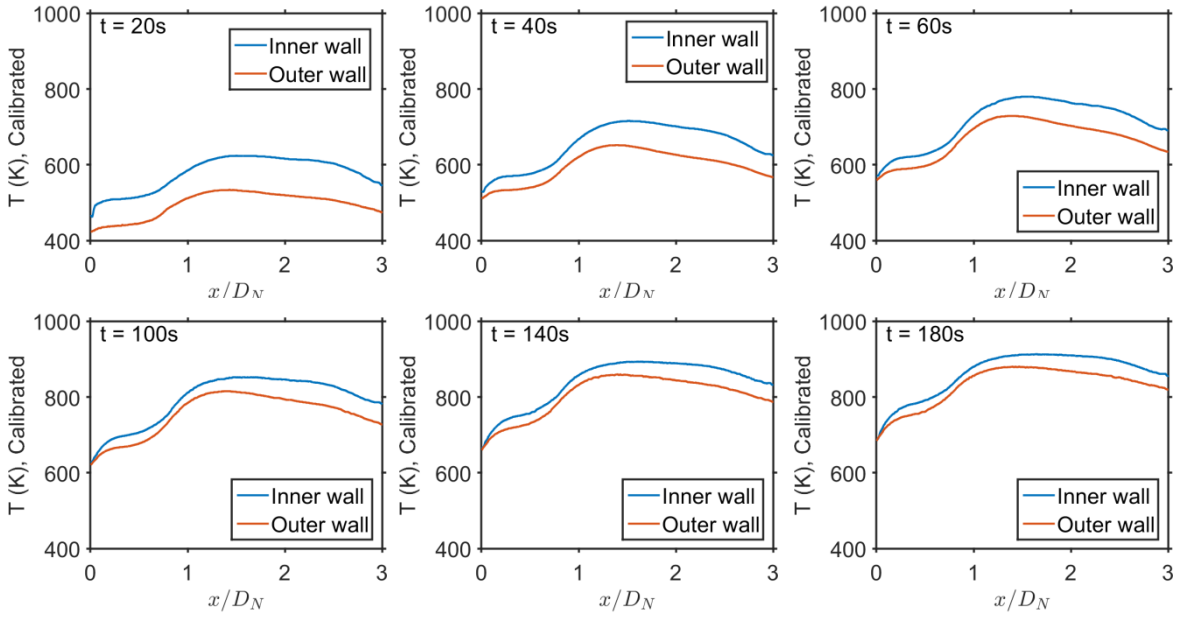

Figure 74. Liner temperature profile at inner wall and outer wall. 2D measurements were averaged in radial/tangential direction.

The peak wall temperature increased from below 400 K to 900 K during 180 s operation. Figure 75 shows the increase of the temperature in time at a fixed axial location. The heat transfer before the main flame ignition was indistinguishable from noise, because the initial temperature was lower than the minimum range this setup can capture. After the main flame ignition, the temperature increase shows typical time response of heating.

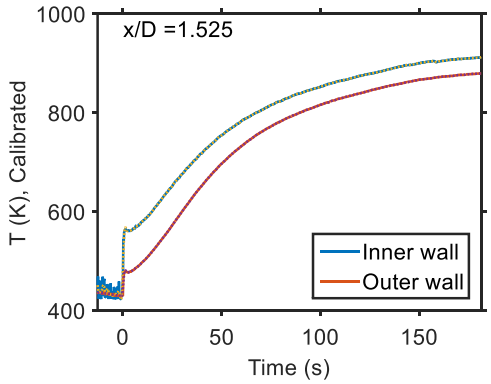

Figure 75. Temperature vs. time near peak location in x.

Figure 76 shows contours of inner and outer wall temperature profiles changing in time. The horizontal axisl is time, and the vertical axis is the axial distance from the dome plate. The peak heat location is almost constant. The peak temperature at the start and the end of the test is plotted more clearly in profiles in Figure 77.

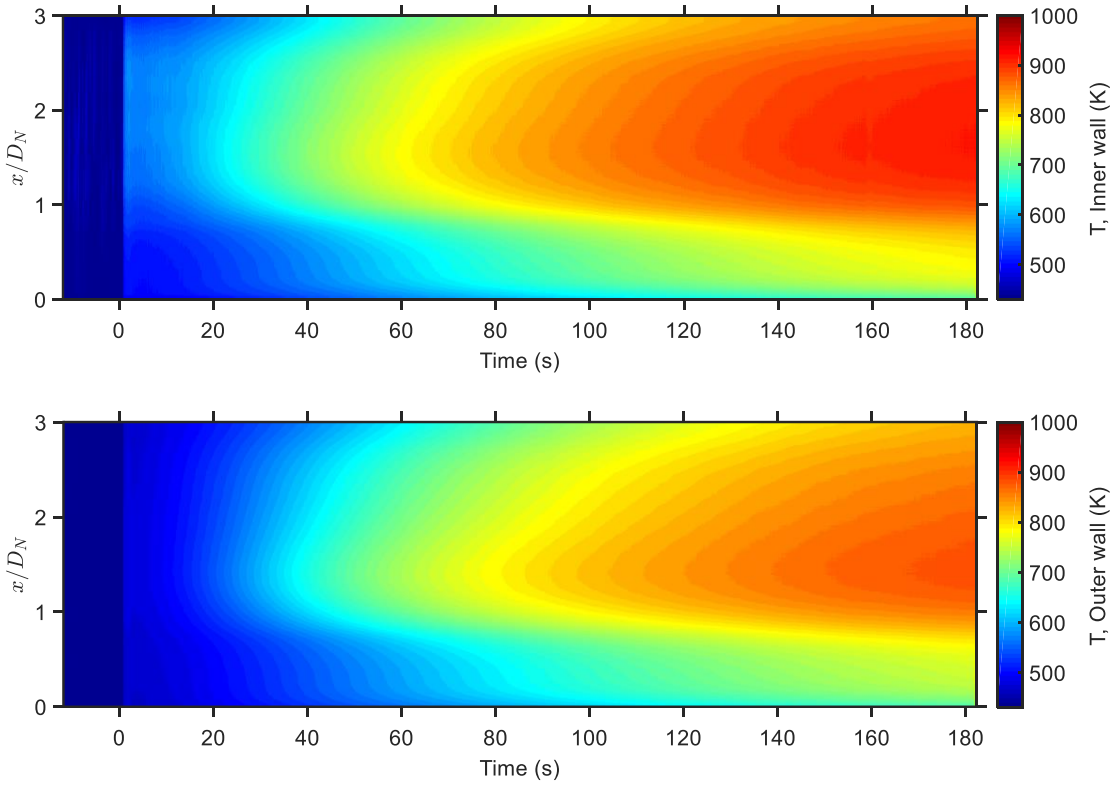

Figure 76. Inner and outer wall temperature evolution in time

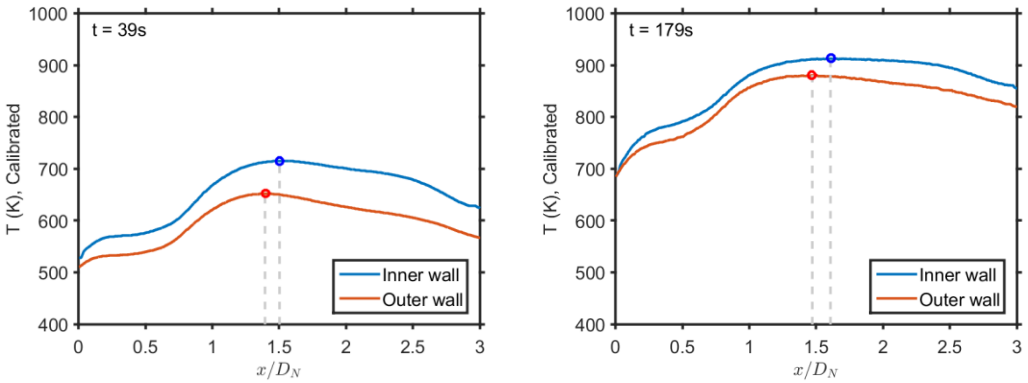

Figure 77. Peak heat transfer location in the start and at the end

6.3.2 Heat Flux: Quasi-steady State Assumption

Heat flux on the liner wall at an experimental time of 180 s was calculated from the temperature difference between the inner and outer wall, and the thermal conductivity of the liner at the mean temperature of the quartz. Quasi steady-state was assumed for the calculation, which is demonstrated by the relatively unchanging temperatures differentials observed for $t = 160$ s, 170 s, and 180 s. Measured peak heat flux on the liner in this case was approximately 23 kW/m^2 at $x \approx 2.3D_N$. A smaller peak of 15 kW/m^2 observed at $x \approx 0.5D_N$ seems to be caused by corner recirculation.

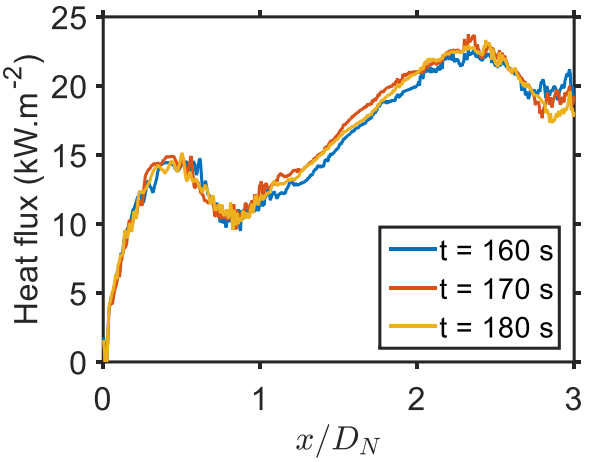

Figure 78. Heat flux on the liner under reacting condition with quasi-steady state assumption (R1 condition)

Heat transfer rate is expected to be high where there are high local Reynolds numbers and high fluid temperatures near the wall. Comparison of the heat flux with the flow field shows that the peak heat flux location was far downstream from the flow impingement location in axial direction. This seems to indicate that the increased temperature of the main flame jet at the downstream location increases heat flux to the liner, which could not be observed in non-reacting heat transfer studies. Moving forward, heat transfer measurements are planned to be performed for different reacting conditions.

6.4 FINITE DIFFERENCE ANALYSIS

6.4.1 Calculation Methodology

Finite difference analysis was performed using the acquired the time evolution of the inner and outer wall surface temperatures profiles on the combustor liner. The temperature distribution inside the liner material was calculated with a finite difference model using the experimentally obtained temperature distributions as boundary conditions. Temperature gradient at the inner surface in the material equals to the flame side total heat flux of the liner.

The temperature does not vary along the azimuthal direction due to axial symmetricity of the geometry. A major source of error in the azimuthal temperature measurement is the dependence of emissivity on the orientation. The IR camera and the normal direction of the surface should be less than 40° for minimal temperature error. In our measurement, the regions of interest are close to the center. Experimentally measured azimuthal temperature variation was less than 12 K. Under the axial symmetricity assumption, the heat transfer model was simplified to 2 dimensions. The domains are axial location *x*, radial location *r* (liner thickness), and time *t*. The boundaries in the azimuthal direction were considered as adiabatic condition ($\partial T/\partial \theta = 0$). The conduction heat transfer of solid material of liner is express as Equation 20. Radiation heat transfer between the inner nodes were assumed to be negligible. Thus, Fourier's law relates the conduction heat transfer and temperature distribution in the solid material.

$$k c_p \frac{\partial T}{\partial t} = \frac{\partial}{\partial x}\left(k \frac{\partial T}{\partial x}\right) + \frac{1}{r}\frac{\partial}{\partial r}\left(kr \frac{\partial T}{\partial r}\right) \tag{20}$$

Implicit Euler method was used to discretize the temperature distribution with first order finite difference in time and second order in space. Simplicity and stability are merits of the implicit Euler method. Equation 21 is the discretized equation with indices *l* and *m* for space (*x* and *r* coordinates respectively) and *n* for time. Material properties are functions of temperature, which varies with time. The conductivity of the quartz k, and the local heat capacity ρc_p were updated during the calculation based on the temperature at previous time step to simplify the computation. The radial domain extends from $r_0 = 101.5$ mm to $r_{mm} = 105.5$ mm, and the axial domain from $x_0 = 0$ to $x_{ll} \approx 207$ mm.

$$
\begin{aligned}
\left(\rho c_p\right)_{l,m}^{n-1} \frac{T_{l,m}^{n} - T_{l,m}^{n-1}}{\Delta t} & \\
&= k_{l,m}^{n-1} \left(\frac{T_{l+1,m}^{n} - 2T_{l,m}^{n} + T_{l-1,m}^{n}}{\Delta x^2}\right) \\
&+ \frac{1}{r}\left[k_{l,m}^{n-1}\left(\frac{T_{l,m+1}^{n} - T_{l,m-1}^{n}}{2\Delta r}\right)\right. \\
&\left. + k_{l,m}^{n-1} r \left(\frac{T_{l,m+1}^{n} - 2T_{l,m}^{n} + T_{l,m-1}^{n}}{\Delta r^2}\right)\right]
\end{aligned}
\tag{21}
$$

The equation is arranged to separate the unknown terms to the left and known terms to the right as in Equation 22.

$$
\left.
\begin{aligned}
T_{l,m}^{n} &\left(\frac{\left(\rho c_p\right)_{l,m}^{n-1}}{\Delta t} + \frac{2k_{l,m}^{n-1}}{\Delta r^2} + \frac{2k_{l,m}^{n-1}}{\Delta x^2}\right) \\
&+ T_{l,m+1}^{n}\left(-\frac{k_{l,m}^{n-1}}{2r\Delta r} - \frac{k_{l,m}^{n-1}}{\Delta r^2}\right) \\
&+ T_{l,m-1}^{n}\left(\frac{k_{l,m}^{n-1}}{2r\Delta r} - \frac{k_{l,m}^{n-1}}{\Delta r^2}\right) \\
&+ T_{l+1,m}^{n}\left(-\frac{k_{l,m}^{n-1}}{\Delta x^2}\right) \\
&+ T_{i-1,k}^{n}\left(-\frac{k_{l,m}^{n-1}}{\Delta x^2}\right)
\end{aligned}
\right\} = \frac{\left(\rho c_p\right)_{l,m}^{n-1}}{\Delta t} T_{l,m}^{n-1}
\tag{22}
$$

The system of equations was solved with MATLAB. A square matrix of size $ll * mm \times ll * mm$ is formulated from the coefficients of the left hand side terms. Final solution representing the temperature of internal nodes was obtained by matrix inversion with initial and boundary condition inputs. At the boundaries of axial location ($l = 0, 618$), adiabatic condition was applied as $T_{0,m}^{n} = T_{1,m}^{n}$ and $T_{ll,m}^{n} = T_{ll-1,m}^{n}$.

The heat flux on the flame side equals to the conduction heat transfer rate (total heat transfer) by energy balance at the inner surface as shown by Equation 23.

$$q''_{r=r_0} = h\left(T_{r=r_0} - T_\infty\right) = -k\frac{\partial T}{\partial r}_{r=r_0} \tag{23}$$

Equation 24 shows the relation for the discretized equations, with node indices, yielding the heat flux distribution (heat transfer rate per unit area). Temperature information at the radial nodes m_0 and m_1 were taken to determine the temperature gradient.

$$q''^{n}_{i} = -k^{n-1}_{l,m}\frac{T^{n}_{l,m0} - T^{n}_{l,m1}}{\Delta r} \tag{24}$$

The effect of total number of nodes in radial direction were tested. *mm* =15 were selected considering the accuracy and calculation time. To analyze 180 s of recorded data, the number of nodes were $ll = 618$, $mm = 15$, and $nn = 900$. For the selected grid size, the computation took approximately 30 minutes with a personal computer using a PC with Intel Xeon 2 GHz dual core processor).

6.4.2 Inner Node Temperature

Temperature distribution within the thickness of the quartz glass wall was obtained using finite difference solver. Boundary conditions are the measured wall temperatures. Figure 79 shows increasing temperature inside the liner wall at an axial location about center (x/D_N = 1.54). Two nodes at r=0 and r = 4 mm are measured data, which are used as inputs for the calculation. The heat flux information during the transient heat transfer process is extracted from this profile. The slope at the inner wall is directly proportional to the hot side the heat transfer. As data was spatially (1D) and temporally resolved, the final heat transfer was also temporal and spatial. It is noticeable that the temperature increases in time, but the heat flux or the slope of the curve at inner surface decreases, which means the hot side heat load decreases in time at the particular axial location.

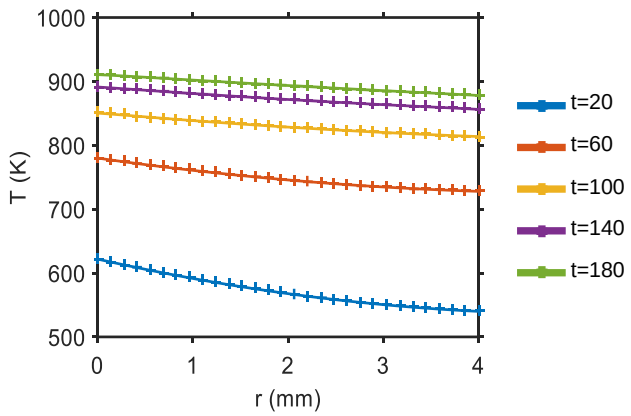

Figure 79. Radial temperature distribution within liner thickness for a selected axial location

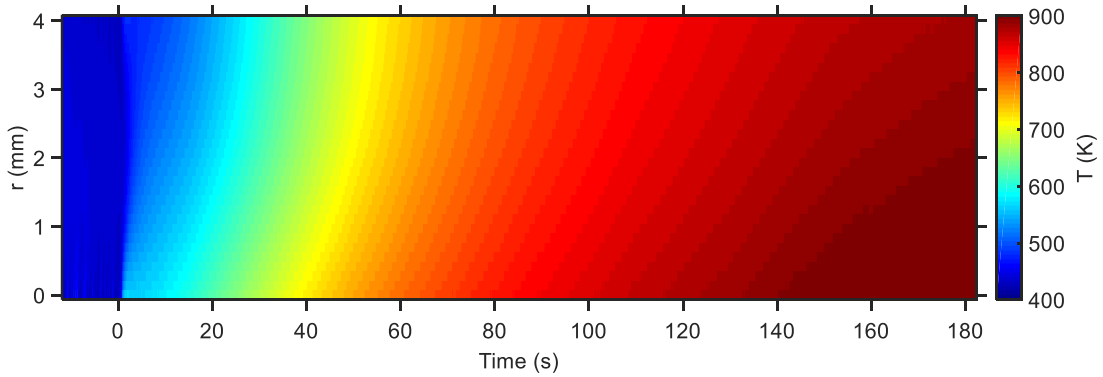

Figure 80. Time resolved radial temperature distribution of the liner wall

6.4.3 Heat Flux: Time-resolved Solution

Measured heat flux in longitudinal axis is shown in Figure 81. Peak heat flux location is denoted with red markers. Initially, high heat flux at low liner temperature was observed. As time moves, the peak heat flux reduces from 60 kW/m^2 to 23 kW/m^2, and the location also moved to the downstream from *x/D* = 1.8 to *x/D* = 2.4. Then, heat transfer is almost at steady state after 160 s. A smaller peak of 15 kW/m^2 was observed at $x \approx 0.5D_N$, due to heat release in the corner recirculation zone. The heat release in the corner recirculation was minor, but it needs to be considered as one of the characteristics of swirl combustors. The most distinct difference between this reacting heat flux profiles and the one at non-reacting flow which was reported in previous terms is that the heat flux increase along the x axis at $0.9 \leq x/D_N \leq 2.3$ due to heat release in reacting flow attached to liner wall. This feature was not observed in the non-reacting measurement.

It clearly means that the heat transfer measurement for realistic testing should be done under the reacting flow condition to accurately measure its characteristics.

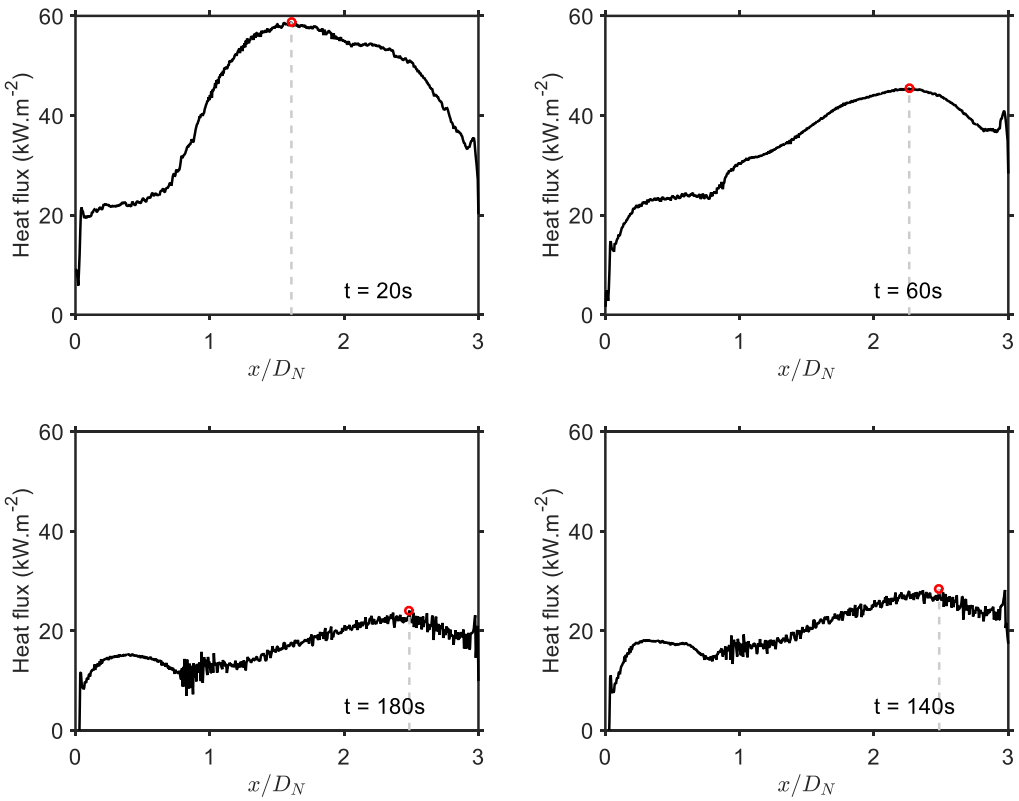

Figure 81. Measured combustor liner heat flux profiles chaning in time

Another way to look at the temperature and heat flux is contour plots. The 2-D plots in Figure 76 and Figure 82 are explaining the temporal evolution of the heat flux profile. The vertical axes on the plots are axial locations, and the horizontal axes are time. Color scales are for wall temperatures and hot side heat flux respectively. For a selected time, vertical color change at a fixed horizontal axis in the contour corresponds to the temperature or the heat flux profile at the moment. In those figures, Moving peak locations are easily observed. For temperature, the peak location is constant at around *x/D*=1.5. The peak location of heat flux, on the other hand, moves from *x/D* = 1.8 to *x/D* = 2.4.

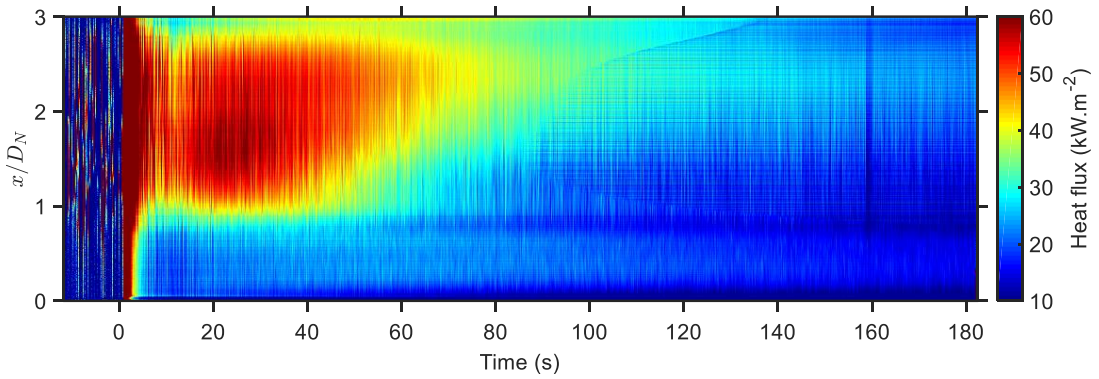

Figure 82. Hot side heat flux evolution in time

6.4.4 Azimuthal Temperature Variation

The wall temperatures measured in 2-dimension are averaged in the vertical direction, resulting in one-dimensional temperature distributions along inner wall and the outer wall. For heat flux calculation, temperature variation along an azimuthal direction is assumed to be small. The variation of the wall temperature is shown in Figure 83. Three axial locations were selected, and then instantaneous azimuthal (or vertical) wall temperatures are plotted for three selected times. Each plot shows increasing surface temperature profile in time. Each curve shows how the temperature varies along the azimuthal direction. The lower temperature zone indicate outer wall painted area. Regions of interest for this analysis are between gray dotted lines. Amounts of temperature variation were different at inner and outer walls, and they also changes in time. Top locations of the wall (y > 0.5) should be avoided in the future because of the most significant azimuthal temperature variation. Inner wall standard deviation is lower than 3.5 K. Peak of outer wall standard deviation is about 12 K at x/D_N = 1.13. Curvature effect, misalignment of geometry, non-uniform paint coat thickness or uneven natural convection at the outer surface might cause the temperature variation.

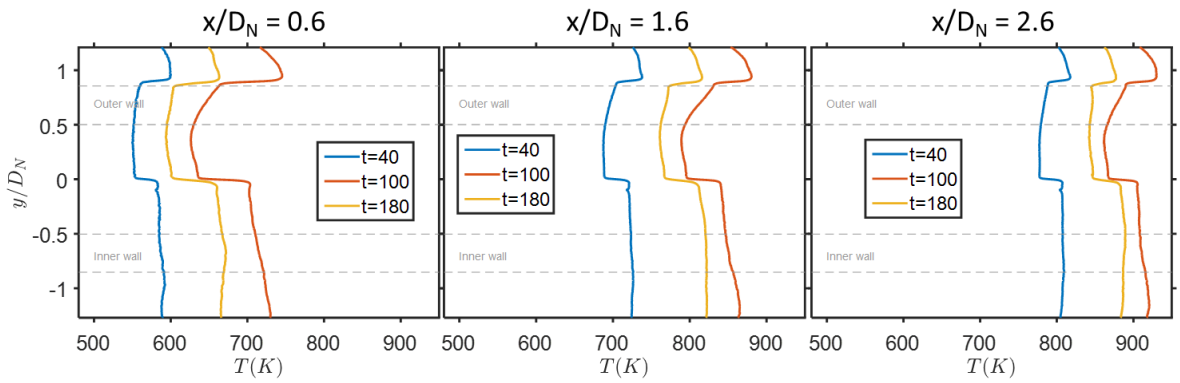

Figure 83. Azimuthal temperature variation for wall temperature measurement

A theoretical prediction of directional emissivity shown in Figure 84 implies that the radiation decreases when target surface is not perpendicular to the sensor direction. Directional emissivity reduces significantly after 50-60 degree angle, which corresponds to the radial location at about 80% of the radius. The area we used for the analysis is within the theoretically valid area. However, due to surface roughness, uneven heat transfer, etc., the measured temperature varies more than the theory. This issue should be experimentally studied to quantify the uncertainty of the measurement. As the effect of directional emissivity is symmetric, even with the error added to the temperature measurement, its effect on heat transfer will be reduced.

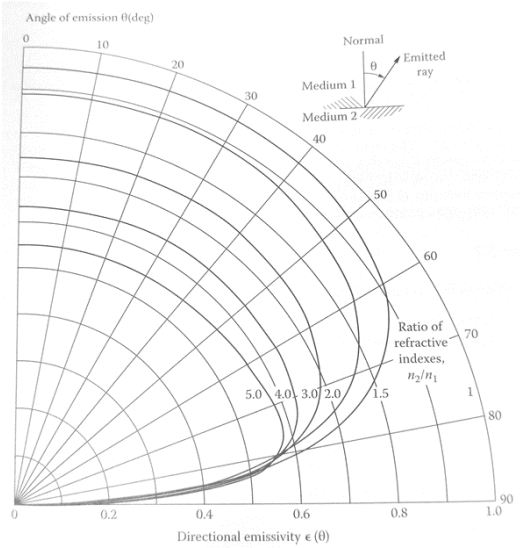

Figure 84. Theoretical prediction of directional emissivity [81].

6.4.5 Uncertainty

The infrared camera reading was calibrated to temperature with a look-up table and interpolation. The fitting table was obtained from comparisons with K-type thermocouples. The error associated with temperature fitting was about 2.5% including 0.75 % thermocouple accuracy.

Heat flux is more sensitive to measurement error than temperature, because the calculation uses difference value of two measurements for inner and outer walls. The relative magnitude of temperature measurement error increases when the difference temperature values decreases. The error is consist of systematic part and random part. By observing multiple sets of measurement data, systematic error related to camera and test section alignments, paint coating quality, and region of interest setting in the data processing showed stronger effect than random error on the measured heat flux. Quantitative uncertainty analysis of the heat transfer measurement has not been completed yet. However, findings about characteristics of heat flux in spatial distributions and time dependent evolution are still valid, despite of contribution from systematic error. Previous reported uncertainty of heat flux using same measurement technique with non-reacting condition was estimated to be less than 25%.

Finite deference calculation assumes linear initial temperature profile for inner nodes. Actual temperature profile inside the glass at initial state does not accurately match with the assumption. Temperature resolution at the initial cold wall condition (<400K) is less than the high temperature range, because of low signal strength with cold wall surfaces. However, updated boundary information during the forward step calculation reduces the effect of inaccuracy of the initial state. Number of time step before main flame ignition are the most important factor. In this work, data recording started at least 30 seconds before the ignition to assure negligible effect from initial conditions.

6.5 SUMMARY AND DISCUSSION

The transient liner heat transfer was measured with an infrared camera at one reacting condition. Wall temperature distributions were measured at the inner and outer wall surfaces of the optical combustor liner. Peak temperature locations were $\approx 0.3\ D_N$ downstream of the flame jet

impingement location, attributed to higher flow temperatures downstream of the flow impingement. The temperature rose up to 900 K after 3 minutes of operation. Heat flux transferred through the liner was measured as ≈ 23 kW/m^2, at $x \approx 2.3D_N$, with an assumption of quasi steady-state wall temperature.

In the PIV measurement, the flow field is shown to be invariant to operating conditions in reacting flows. Impingement locations and swirl structures did not vary with different equivalence ratio, air mass flow rate, pilot fuel ratio, and inlet temperature. Similar analysis needs to be done with wall heat transfer study. Temperature measurement with thermocouple (including indirect field information from IR flame radiation) can be used to explain the heat transfer. For example, Figure 85 compares near wall flow properties and liner heat transfer. Flow temperature and wall temperature are both showing characteristics step change due to cold region (outer recirculation). The points that are the boundary between low temperature and high temperature are different for flow and surface temperatures, because heat transfer is enhanced by flow impingement at *x/D* ~ 1.2. Peak temperature is located at *x/D* ~ 1.5, where the effect of impingement and high flow temperature partially overlaps.

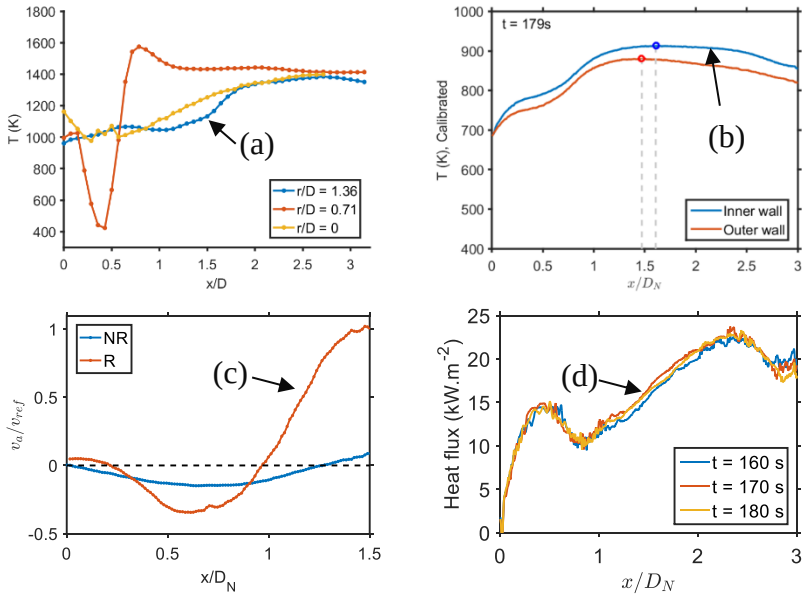

Figure 85. Near wall flow properties and liner heat transfer: (a) flow temperature, (b) inner wall surface temperature, (c) axial velocity, (d) wall heat flux

Heat flux profile is distinct from temperature profiles. Flow velocity profile (shown until *x/D* ~ 1.5) shows zero crossing at *x/D* ~ 1.0 and negative and positive regions. A dip observed on

the heat flux profile at $x/D \sim 1.0$ coincide with the velocity zero crossing. The negative axial velocity meaning recirculation at ORZ, and location of the peak is close to the small heat flux peak at $x/D \sim 0.5$. Flow temperature is almost constant after the impingement, but the heat transfer increases until $x/D \sim 2.3$. This can be explained by increase in velocity due to heat release. The increased velocity causes higher local heat transfer coefficient, hence higher heat flux. The heat flux is more complex than the surface temperature because it is affected by time varying internal properties of solid and heat loss from the liner to the surrounding (by means of radiation and natural convection). Moreover, uncertainty of heat flux is relatively higher than other data. It is still challenging to reach strong conclusion to relate heat transfer, however, this investigation provides important characteristics of liner wall heat transfer and its relation to the reacting flow.

The following works regarding the combustor transfer will be parametric investigation for different operating conditions. Finally, the detailed experimental data about the flow properties and wall heat transfer will have direct impact on combustor thermal management. Empirical information about thermal stress and temperature distribution on swirl combustor will be very useful for optimal cooling design.

The thermal load on the combustor walls is an important design parameter for optimization of combustor cooling and emissions. Understanding the combustor wall temperature and velocity fields will provide insight into the mechanisms driving the convective heat loads. Therefore, it is necessary to improve experimental methods to experimentally corroborate the characteristics of reacting flow and to predict heat transfer in reacting condition. The transient infrared liner temperature measurement technique described in this study can be used as an accurate method for detailed 2D liner wall temperature and heat flux measurements, which to date are accomplished with thermocouples or thermal paints (low accuracy).

CHAPTER 7. CONCLUSIONS

The characteristics of various aspects of reacting flow in a model combustor were identified in this work. The key findings are: 1) independence of swirl flow structure and flow impingement location from combustor operating conditions, 2) detailed temperature and heat flux distribution of the swirling flow in the combustor primary zone, 3) infrared flow structure captured with IR camera, 4) time resolved surface temperature and heat flux distribution on the liner with reacting flow using IR camera. The observations provide information about the effects of the measured flow properties on the liner wall heat transfer under reacting swirl flow conditions. The experimental data using an industrial fuel nozzle in this work can be directly used for efficient thermal management design.

Planar particle image velocimetry (PIV) data were analyzed to understand the characteristics of the flow field. Characterizing the impingement location on the liner, and the turbulent kinetic energy (TKE) distribution were a fundamental part of the investigation. Proper orthogonal decomposition (POD) further analyzed the data to compare coherent structures in the reacting and non-reacting flows. Experiments were conducted at Reynolds numbers ranging between 50000 and 110000 (with respect to the nozzle diameter, D_N); equivalence ratios between 0.55 and 0.78; pilot fuel split ratios of 0 to 6%; inlet air temperature of 20 C to 200 C, two different fuel types with methane and propane.

Comparison between reacting and non-reacting flows yielded very interesting and striking differences. This is the first study that focuses on understanding the differences in flow fields with and without reaction in a realistic gas turbine combustor and the implications on heat flux distributions along the liner. Self-similar characteristics were observed at different reacting conditions. Flame jet impingement locations on the combustor liner wall were qualitatively determined. Swirling exit flow from the nozzle was found to be unaffected by the operating conditions with little effect on the liner. There were minor changes in the flow depending on different equivalence ratios (wider annular jet flow with high equivalence ratios indicating more mixing). Nevertheless, the jet impingement locations at the liner wall were consistent at around $x=1.16\ D_N$ with 7% standard deviation for the reacting conditions tested in this study. The self-similarity of the reacting flow field and the invariance of the location of flame impingement on the

liner wall, allows for scaling of the results to other operating points, simplifying the design and testing of cooling methods for combustor liners, and lowering the cost and effort to develop and operate combustors.

Flow temperature in a lean-premixed swirl combustor was measured with a scanning thermocouple probe. The 2-dimensional temperature map was obtained for reacting flow in the primary zone of the model combustor. The measured temperature in the main jet was about 400 K, and it increased gradually as the jet approached the wall. The peak temperature was about 1600 K at the inner shear layer and the center of inner recirculation zone. The near wall temperature profile along the axis was identified. The temperature in the outer recirculation was around 1000 K, while the temperature downstream of jet impingement location was around 1400 K. The non-uniform profile of near wall temperature observed in this work implies that the temperature difference will result in significant contribution to the convective wall heat transfer. If a single average flow temperature is used in the correlation for convective heat transfer, it will not accurately estimate the heat load, with more severe mismatch near outer recirculation zone in swirl combustors. The heat load estimation should account for the non-uniformity in the properties of reacting flow to optimize combustor cooling schemes.

Infrared radiation was also measured with a thermographic camera. Abel transformation reconstructed the projected image to infrared radiant energy density in 2D plane under axisymmetric assumption. Flow features in the infrared measurement agreed with flame luminosity and temperature map. An interesting fact is that infrared data could visualize flow structure that cannot be captured with a single method either an RGB camera or a thermocouple probe only. Double shear layer structure was not visible in the flame images, and the pilot jet did not appear in the thermocouple measured temperature map. Both could be captured with infrared image. The infrared thermographic imaging showed possibility as a non-intrusive diagnostic technique for turbulent flames in modern combustors.

Liner surface temperatures were measured with reacting flow in a combustor with an infrared camera for a single case. And time resolved axial distribution of hot side heat flux on combustor liner wall was calculated using finite difference model. Peak temperature locations were downstream of the flame jet impingement location by ≈0.3 D_N, attributed to higher flow temperatures. The temperature rose up to 900 K after 3 minutes of operation. Heat flux transferred through the liner was measured as ≈ 23 kW/m^2, at $x \approx 2.3D_N$. An intriguing phenomena observed

in this study is moving maximum heat flux location. While temperature peak is stationary, the heat flux peak changed its location in time. Further study about the peak heat flux location will improve understanding on thermal load on the liner. The time-resolved infrared liner temperature measurement technique described in this study can be used as an accurate method for detailed 2D liner wall temperature and heat flux measurements, which to date are accomplished with low accuracy thermocouples or thermal paints.

DLE combustors in modern gas turbines with minimized film cooling and dilution air. With minimal or no film cooling, it is more difficult to maintain the metal temperature below its limit. Optimized impingement cooling or other types of efficient backside cooling schemes are crucial for such configurations. Experimental heat transfer data and the relations to flow properties found in this work can provide useful data for the cooling design. For example, amount of coolant for impingement cooling can be minimized by adjusting location of impingement cooling jets and local coolant flow rate on the back side of liner, reflecting high wall temperature locations found in this work. From time-dependent wall temperature measurement and PIV flow measurement, the peak heat transfer location is found downstream of flow impingement, which was time independent. The first target of cooling should be the invariant peak temperature location. More specifically, the temperature profile data can be used as boundary conditions for numerical studies on design optimizations of the backside impingement cooling.

Understanding heat transfer from the working fluid to the solid surfaces are one of the prime interests in gas turbine combustor research. Convection is the most complicated process among different mechanisms of heat transfer, especially for reacting flow conditions. PIV velocity field and flow temperature measurement conducted under various conditions in this research showed important characteristics of flow properties and heat transfer. Further study on the relations between heat transfer and flow properties will allow systematic cooling design for improved combustor cooling and enhanced overall gas turbine performance, in terms of efficiency, pollutants and reliability.

NOMENCLATURE

A	Area
c_p	Specific heat capacity at constant pressure
CRZ	Central recirculation zone
d, D	Diameter
D_C	Combustor diameter
G_X	Axial flux of axial momentum
G_ϕ	Axial flux of tangential momentum
k	Thermal conductivity, Turbulent kinetic energy (TKE)
$\dot{m}$	Mass flow rate
Nu	Nusselt number
P, p	Pressure
Pr	Prandtl number
Q''	Heat Flux
Q	Heat rate, flow rate
r	Compression ratio (P_2/P_1), radial distance
R	Combustor radius
R_{XY}	Cross-correlation
Re	Reynolds Number
S	Swirl number
t	Temperature ratio (T_3/T_1)
T	Temperature
$\boldsymbol{v}$	Velocity field
VB	Vortex breakdown
W	Specific work output
x	Axial direction (along the combustor axis)
w	Tangential velocity
η	Thermal efficiency (net work output by heat input)

γ	Ratio of specific heats
μ	Dynamic viscosity
ϕ	Fuel-air equivalence ratio
ρ	Density
τ_s	Relaxation time
Ω	Vorticity

Subscript

$(\cdot)_1$	Inlet to the gas turbine.
$(\cdot)_2$	Outlet of the compressor (inlet of the combustor)
$(\cdot)_3$	Outlet of the combustor (inlet of the turbine)
$(\cdot)_4$	Gas turbine exhaust (outlet of the turbine)
$(\cdot)_{air}$	Air
$(\cdot)_C$	Related to the combustor diameter
$(\cdot)_f$	Related to the film temperature
$(\cdot)_{fluid}$	Fluid
$(\cdot)_N$	Nozzle
$(\cdot)_{particle}$	Particle
$(\cdot)_r$	Radial coordinate
$(\cdot)_{ref}$	Reference
$(\cdot)_W$	Related to the liner wall or surface
$(\cdot)_x$	Axial coordinate
$(\cdot)_\infty$	Related to the working fluid temperature
$\overline{(\cdot)}$	Mean
$\widehat{(\cdot)}$	Unit vector
$(\cdot)'$	Fluctuation

REFERENCES

[1] https://www.eia.gov/todayinenergy/detail.php?id=25392

[2] Saravanamuttoo, H.I.H., Rogers, G.F.C., and Cohen H., 2001, Gas Turbine Theory, 5th ed., Pearson Education Limited. ISBN-10: 0-13-015847-X.

[3] Han, J.C., Dutta, S. and Ekkad, S., 2012. Gas turbine heat transfer and cooling technology. CRC Press.

[4] Price, J.R., 2009, "Advanced Materials For Mercury 50 Gas Turbine Combustion System". Final Report submitted to U.S. Department of Energy, under Federal Contract DE-FC26-00CH11049.

[5] Nelson, W.A. and Orenstein, R.M., 1997. TBC experience in land-based gas turbines. Journal of Thermal Spray Technology, 6(2), pp.176-180.

[6] Miriyala, N., Fahme, A. and van Roode, M., 2001, June. Ceramic Stationary Gas Turbine Program: Combustor Liner Development Summary. In ASME Turbo Expo 2001: Power for Land, Sea, and Air (pp. V004T02A009-V004T02A009). American Society of Mechanical Engineers.

[7] Corman, G.S., Dean, A.J., Brabetz, S., Brun, M.K., Luthra, K.L., Tognarelli, L. and Pecchioli, M., 2000, May. Rig and engine testing of melt infiltrated ceramic composites for combustor and shroud applications. In ASME Turbo Expo 2000: Power for Land, Sea, and Air (pp. V004T02A019-V004T02A019). American Society of Mechanical Engineers.

[8] Bradshaw, S. and Waitz, I., 2009. Impact of manufacturing variability on combustor liner durability. Journal of Engineering for gas turbines and Power, 131(3), p.032503.

[9] Kim, K.M., Yun, N., Jeon, Y.H., Lee, D.H. and Cho, H.H., 2010. Failure analysis in after shell section of gas turbine combustion liner under base-load operation. Engineering Failure Analysis, 17(4), pp.848-856.

[10] Tinga, T., Van Kampen, J.F., De Jager, B. and Kok, J.B., 2007. Gas turbine combustor liner life assessment using a combined fluid/structural approach. Journal of Engineering for Gas Turbines and Power, 129(1), pp.69-79.

[11] Carter, T.J., 2005. Common failures in gas turbine blades. Engineering Failure Analysis, 12(2), pp.237-247.

[12] Correa, S.M., 1993. A review of NOx formation under gas-turbine combustion conditions. Combustion science and technology, 87(1-6), pp.329-362.

[13] Image by Jeff Dahl. https://en.wikipedia.org/wiki/Turbojet#/media/File:Jet_engine.svg

[14] Lefebvre A. H., and Ballal D. R., 2010, Gas Turbine Combustion, Alternative Fuels and Emissions, 3rd ed., CRC press, FL, USA.

[15] Mellor, A.M., 1990. Design of modern turbine combustors. Academic Pr.

[16] Photo by Oliver Cleynen, https://en.wikipedia.org/wiki/Combustor#/media/File: Combustor_ on_Rolls-Royce_Nene_turbojet_%281%29.jpg

[17] Environmental Protection Agency (EPA), 2006, "40 CFD Part 60, Standards of Performance for Stationary Combustion Turbines; Final Rule," Federal Register, 71:38482-38506.

[18] Kurz, R., Brun, K., Meher-Homji, C. and Moore, J., 2012. Gas turbine performance and maintenance. In 41st Turbomachinery Symposium, Houston, TX, Sept (pp. 24-27).

[19] Cowell, L., 2001, "Proven Solution Solar", Solar presentation in CORE Symposium.

[20] Huang, Y., and Yang, V., 2009, "Dynamics and stability of lean-premixed swirl-stabilitzed combustion," Progress in Energy and Combustion Science, 35, pp. 293-364.

[21] Lilley, D., 1977, "Swirl Flows in Combustion: A Review," AIAA Journal, 15, No.8, pp. 1063–1078.

[22] Beer, J.M., and Chigier, N.A., 1983, "Combustion Aerodynamics," Robert E. Krieger Publishing Company, Fl, USA.

[23] Syred, N., and Beer, J.M., 1974, "Combustion in Swirling Flows: A Review," Combustion and Flame, No.23, pp. 143-201.

[24] Gupta, A.K., Lilley, D.G., and Syred, N., 1984, "Swirl Flows," Abacus Press, MA, USA.

[25] Sloan, D., Smith, P.J., and Smoot, D., "Modeling of swirl in turbulent flow systems", Progress in Energy and Combustion Science, Vol. 12, No.3, pp. 163-250. DOI:10.1016/0360-1285(86)90016-X

[26] Hill, P.G., and Peterson, C.R., 1992, Mechanics and Thermodynamics of Propulsion, 2nd ed., Prentice Hall.

[27] Lieuwen, T.C., 2012, Unsteady Combustor Physics, 1st ed., Cambridge University press, NY, USA.

[28] Lucca-Negro, O., and O'Doherty, T., 2001, "Vortex Breakdown: a review," Progress in Energy and Combustion Science, No.27, pp. 431-481.

[29] Syred, N., 2006, "A review of oscillation mechanisms and the role of the precessing vortex core (PVC) in swirl combustion systems," Progress in Energy and Combustion Science, No.32, pp. 93-161.

[30] Kilik, E., 1976, "The influence of swirler design parameters on the aerodynamics of downstream recirculation region" (Doctoral Dissertation), Cranfield University.

[31] Farokhi S., Taghavi R., and Rice E.J., 1989, "The effect of initial swirl distribution on the evolution of a turbulent jet," AIAA Journal, Vol. 27, No. 6. DOI: 10.2514/3.10168

[32] Hallet, W.L.H., and Toews, D.J., 1987, "The effects of inlet conditions and expansion ratio on the onset of flow reversal in swirling flow in a sudden expansion", Experiments in Fluids, Vol. 5, No.2, pp. 129-133.

[33] Faler, J.H., and Leibovich, S., 1977, "Disrupted states of vortex flow and vortex breakdown," Physics of Fluids, Vol. 20, No.9, pp. 1385-1400. DOI: 10.1063/1.862033

[34] Terhaar, S., Reichel, T.G., Schrodinger, C., Rukes, L., Paschereit, C.O., and Oberleithner, K., 2015, "Vortex Breakdown Types and Global Modes in Swirling Combustor Flows with Axial Injection," Journal of Propulsion and Power, 31, No.1, pp.219-229.

[35] Carmack, A., Ekkad, S., Kim, Y., Moon, H.-K., Srinivasan, R., 2013, "Comparison of Flow and Heat Transfer Distributions in a Can Combustor for Radial and Axial Swirlers Under Cold Flow Conditions," Journal of Thermal Science and Engineering Applications, Vol.5, 031012.

[36] Strakey, P.A., and Yip, M.J., 2007, "Experimental and Numerical Investigation of a Swirl Stabilized Premixed Combustor Under Cold-Flow Conditions," Transactions of the ASME, Vol. 129, pp. 942-953.

[37] Ji, J., and Gore, J.P., 2002, "Flow structure in lean premixed swirling combustion," Proceedings of the Combustion Institute, Vol. 29, pp. 861-867.

[38] Lefebvre A. H., and Herbert, M.V., 1960, "Heat-Transfer Processes in Gas-Turbine Combustion Chambers," Proceedings of the Institution of Mechanical Engineers, Vol. 174, No. 1, pp. 463-478. DOI: 10.1243/PIME_PROC_1960_174_039_0

[39] Viskanta, R., and Menguc, M.P., 1987, "Radiation heat transfer in combustion systems", Progress in Energy and Combustion Science, Vol. 13, No. 2, pp. 97-160. DOI: 10.1016/0360-1285(87)90008-6

[40] Viskanta, R., 1993, "Heat Transfer to impinging isothermal gas and flame jets," Experimental Thermal and Fluid Science, Vol. 16, no. 2, pp. 111-134.DOI: 10.1016/0894-1777(93)90022-B

[41] Lefebvre, A.H., 1984. Flame radiation in gas turbine combustion chambers. International journal of heat and mass transfer, 27(9), pp.1493-1510.

[42] Burmeister, L.C., 1993, Convective Heat Transfer, 2nd ed., Wiley, ISBN: 047157709X

[43] Lienhard, J.H., and Lienhard, J.H., 2015, A Heat Transfer Textbook, 4th ed., Phlogiston Press, Cambridge, Massachusetts, USA.

[44] Petukhov, B.S., 1970. “Heat transfer and friction in turbulent pipe flow with variable physical properties,” Advances in heat transfer, Vol. 6, No. 503, pp 503-564.

[45] Gnielinski, V., 1975. “Neue Gleichungen für den Wärme-und den Stoffübergang in turbulent durchströmten Rohren und Kanälen,” Forschung im Ingenieurwesen A, Vol. 41, No. 1, pp.8-16.

[46] Gnielinski, V., 2013. “On heat transfer in tubes. International Journal of Heat and Mass Transfer,” 63, pp.134-140.

[47] Sleicher, C.A. and Rouse, M.W., 1975. “A convenient correlation for heat transfer to constant and variable property fluids in turbulent pipe flow,” International Journal of Heat and Mass Transfer, Vol. 18 No. 5, pp.677-683.

[48] Dellenback, P.A., Metzger, D.E. and Neitzel, G.P., 1987. “Heat transfer to turbulent swirling flow through a sudden axisymmetric expansion,” Journal of heat transfer, Vol. 109, No. 3, pp.613-620.

[49] Baughn, J.W., Hoffman, M.A., Takahashi, R.K. and Launder, B.E., 1984. “Local heat transfer downstream of an abrupt expansion in a circular channel with constant wall heat flux,” Journal of heat transfer, Vol. 106, No. 4, pp.789-796.

[50] Yilmaz, M., Comakli, O., Yapici, S. and Sara, O.N., 2003. “Heat transfer and friction characteristics in decaying swirl flow generated by different radial guide vane swirl generators,” Energy Conversion and Management, Vol. 44, No. 2, pp.283-300.

[51] Patil, S., Abraham, S., Tafti, D., Ekkad, S., Kim, Y., Dutta, P., Moon, H.K. and Srinivasan, R., 2011. “Experimental and numerical investigation of convective heat transfer in a gas turbine can combustor,” Journal of Turbomachinery, Vol. 133, No. 1, p.011028.

[52] Kedukodi, S., Ekkad, S., Moon, H.K., Kim, Y. and Srinivasan, R., 2015, June. “Numerical Investigation of Effect of Geometry Changes in a Model Combustor on Swirl Dominated Flow and Heat Transfer,” In ASME Turbo Expo 2015: Turbine Technical Conference and Exposition (pp. V05CT17A011-V05CT17A011). American Society of Mechanical Engineers.

[53] Patil, S., Sedalor, T., Tafti, D., Ekkad, S., Kim, Y., Dutta, P., Moon, H.K. and Srinivasan, R., 2011. “Study of flow and convective heat transfer in a simulated scaled up low emission annular combustor,” Journal of Thermal Science and Engineering Applications, Vol. 3, No. 3, p.031010.

[54] Gomez-Ramirez, D., Dilip, D., Ravi, B.V., Deshpande, S., Pandit, J., Ekkad, S.V., Moon, H.K., Kim, Y. and Srinivasan, R., 2015. “Combustor Heat Shield Impingement Cooling and its Effect on Liner Convective Heat Transfer for a Model Annular Combustor With Radial Swirlers,” In ASME Turbo Expo 2015: Turbine Technical Conference and Exposition (pp. V05CT17A010-V05CT17A010). American Society of Mechanical Engineers.

[55] Andreini, A., Caciolli, G., Facchini, B., Picchi, A. and Turrini, F., 2015. “Experimental investigation of the flow field and the heat transfer on a scaled cooled combustor liner with realistic swirling flow generated by a lean-burn injection system,” Journal of Turbomachinery, Vol. 137, No. 3, p.031012.

[56] Mazzei, L., Andreini, A., Facchini, B. and Turrini, F., 2016. “Impact of Swirl Flow on Combustor Liner Heat Transfer and Cooling: A Numerical Investigation With Hybrid Reynolds-Averaged Navier Stokes–Large Eddy Simulation Models,” Journal of Engineering for Gas Turbines and Power, Vol. 138, No. 5, p.051504.

[57] Ruedel, U., Trbojevic, B., Benz, U., Zajadatz, M. and Doebbeling, K., 2013, June. Development of an Annular Combustor Chamber. In ASME Turbo Expo 2013: Turbine Technical Conference and Exposition (pp. V03CT17A009-V03CT17A009). American Society of Mechanical Engineers.

[58] Lörstad, D., Lindholm, A., Pettersson, J., Björkman, M. and Hultmark, I., 2013, June. Siemens SGT-800 industrial gas turbine enhanced to 50MW: Combustor design modifications, validation and operation experience. In ASME Turbo Expo 2013: Turbine Technical Conference and Exposition (pp. V01BT04A038-V01BT04A038). American Society of Mechanical Engineers.

[59] Sen, B.A., Guo, Y., McKinney, R.G., Montanari, F. and Bedford, F.C., 2012, June. Pratt and Whitney gas turbine combustor design using ANSYS fluent and user Turbo Expo 2012: Turbine Technical Conference and Exposition (pp. 1547-1556). American Society of Mechanical Engineers.

[60] Lai, M.K., 1997, June. CFD analysis of liquid spray combustion in a gas turbine combustor. In ASME 1997 International Gas Turbine and Aeroengine Congress and Exhibition (pp. V002T06A044-V002T06A044). American Society of Mechanical Engineers.

[61] Aldén, M., Omrane, A., Richter, M. and Särner, G., 2011. Thermographic phosphors for thermometry: a survey of combustion applications. Progress in energy and combustion science, 37(4), pp.422-461.

[62] Brübach, J., Hage, M., Janicka, J. and Dreizler, A., 2009. Simultaneous phosphor and CARS thermometry at the wall–gas interface within a combustor. Proceedings of the combustion institute, 32(1), pp.855-861.

[63] Brübach, J., Pflitsch, C., Dreizler, A. and Atakan, B., 2013. On surface temperature measurements with thermographic phosphors: a review. Progress in Energy and Combustion Science, 39(1), pp.37-60.

[64] Feist, J.P., Heyes, A.L., Choy, K.L. and Su, B., 1999. Phosphor thermometry for high temperature gas turbine applications. In Instrumentation in Aerospace Simulation Facilities, 1999. ICIASF 99. 18th International Congress on (pp. 6-1). IEEE.

[65] Feist, J.P., Heyes, A.L. and Seefelt, S., 2003. Thermographic phosphor thermometry for film cooling studies in gas turbine combustors. Proceedings of the Institution of Mechanical Engineers, Part A: Journal of Power and Energy, 217(2), pp.193-200.

[66] Borman, G. and Nishiwaki, K., 1987. Internal-combustion engine heat transfer. Progress in energy and combustion science, 13(1), pp.1-46.

[67] Alkidas, A.C. and Myers, J.P., 1982. Transient heat-flux measurements in the combustion chamber of a spark-ignition engine. Journal of Heat Transfer, 104(1), pp.62-67.

[68] Vosen, S.R., Greif, R. and Westbrook, C.K., 1985, December. Unsteady heat transfer during laminar flame quenching. In Symposium (International) on Combustion (Vol. 20, No. 1, pp. 75-83). Elsevier.

[69] Vega, T., Wasson, A.R., Lattimer, B.Y., and Diller, T.E., 2015, "Partitioning measurements of convective and radiative heat flux" International Journal of Heat and Mass Transfer 84, pp. 827-838.

[70] T.E. Diller, Heat flux measurement, Ch8, in: M. Kutz (Ed.), Handbook of Measurement in Science and Engineering, Jon Wiley & Sons, NY, 2013.

[71] Lattimer, B.Y., Vandsburger, U., and Langley, L.W. "Detecting fires using a thin-film heat flux microsensor, in"ASME Winter Annual Meeting, Chicago, Illinois, HTD,vol.296 (1994): 137-142.

[72] Frankman, D., Webb, B.W., Butler, B.W., "Time-resolved radiation and convection heat transfer in combusting discontinous fuel beds," Combust. Sci. Technol. 182, no10 (2010): 1391-1412.

[73] Rippe, C.M. and Lattimer, B.Y., 2015. Full-field surface heat flux measurement using non-intrusive infrared thermography. Fire Safety Journal, 78, pp.238-250.

[74] Hindasageri, V., Vedula, R.P., and Prabhu, S.V., "Heat Transfer distribution for impinging methane-air premixed flame jets," Applied Thermal Engineering.73, (2014): 461-473.

[75] Baukal, C.E. and Gebhart, B. "A Review of Flame Impingement Heat Transfer Studies Part 1: Experimental Conditions" Combustion Science and Technology 104, no. 4-6 (1995): 339-357. DOI: 10.1080/00102209508907727

[76] Baukal, C.E. and Gebhart, B. "A Review of Flame Impingement Heat Transfer Studies Part 2: Measurements" Combustion Science and Technology 104, no. 4-6 (1995): 359-385. DOI: 10.1080/00102209508907728

[77] Baukal, C.E. and Gebhart, B. "A review of empirical flame impingement heat transfer correlations" International Journal of Heat and Fluid Flow 17, no. 4 (1996): 386-396.

[78] Viskanta, R. "Heat Transfer to impinging isothermal gas and flame jets" Experimental Thermal and Fluid Science 16, no. 2 (1993): 111-134.

[79] Baukal, C.E. and Gebhart, B. "Surface condition effects on flame impingement heat transfer" Experimental Thermal and Fluid Science 15, no. 4 (1997): 323-335.

[80] Chander, S. and Ray, A. "Flame Impingement heat transfer: A review" Energy Conversion and Management 46 (2005): 2803-2837.

[81] Fletcher, T.H., Ma, J., Rigby, J.R., et. al, "Soot in coal combustion systems" Progress in Energy and Combustion Science 23, no. 3 (1997): 283-301.

[82] J. R. Howell, M. P. Menguc, and R. Siegel, Thermal radiation heat transfer. CRC press, 2010.

[83] Keramida, E.P., Liakos, H.H., Founti, M.A., et. al, "Radiative heat transfer in natural gas-fired furnaces" International Journal of Heat and Mass Transfer 43, no. 10 (2000): 1801-1809.

[84] David Gomez-Ramirez, "Heat Transfer and Flow Measurements in an Atmospheric Lean Pre-Mixed Combustor," Virginia Tech, 2016.

[85] Gomez-Ramirez, D., Kedukodi, S., Gadiraju, S., Ekkad, S. V., Moon, H.-K., Kim, Y., and Srinivasan, R., 2016, "Gas Turbine Combustor Rig Development and Initial Observations at Cold and Reacting Flow Conditions," ASME Turbo Expo 2016: Turbomachinery Technical Conference and Exposition, American Society of Mechanical Engineers, p. V05BT17A016-V05BT17A016.

[86] Heitor, M. V., and Whitelaw, J. H., 1986, "Velocity, Temperature, and Species Characteristics of the Flow in a Gas-Turbine Combustor," Combust. Flame, 64(1), pp. 1–32.

[87] Weigand, P., Meier, W., Duan, X. R., Stricker, W., and Aigner, M., 2006, "Investigations of Swirl Flames in a Gas Turbine Model Combustor," Combust. Flame, 144(1–2), pp. 205–224.

[88] Stopper, U., Meier, W., Sadanandan, R., Stöhr, M., Aigner, M., and Bulat, G., 2013, "Experimental Study of Industrial Gas Turbine Flames Including Quantification of Pressure Influence on Flow Field, Fuel/Air Premixing and Flame Shape," Combust. Flame, 160(10), pp. 2103–2118.

[89] Gomez-Ramirez, D., Ekkad, S. V., Moon, H.-K., Kim, Y., and Srinivasan, R., 2017, "Isothermal Coherent Structures and Turbulent Flow Produced by a Gas Turbine

Combustor Lean Pre-Mixed Swirl Fuel Nozzle," Exp. Therm. Fluid Sci., 81, pp. 187–201.

[90] Gomez-Ramirez, D., Kedukodi, S., Ekkad, S. V., Moon, H.-K. X., Kim, Y., and Srinivasan, R., 2017, "Investigation of Isothermal Convective Heat Transfer in an Optical Combustor with a Low-Emissions Swirl Fuel Nozzle," Appl. Therm. Eng., 114, pp. 65–76.

[91] https://www.dantecdynamics.com/measurement-principles-of-piv

[92] Kedukodi, S., and Ekkad, S., 2015, "Effect of Downstream Contraction on Liner Heat Transfer in a Gas Turbine Combustor Swirl Flow," ASME 2015 Gas Turbine India Conference, American Society of Mechanical Engineers, p. V001T04A002–V001T04A002.

[93] Cowell, L., Etheridge, C., and Smith, K., 2002, "Ten Years of DLE Industrial Gas Turbine Operating Experiences," ASME Turbo Expo 2002: Power for Land, Sea, and Air, American Society of Mechanical Engineers, pp. 1123–1135.

[94] Chterev, I., Foley, C. W., Foti, D., Kostka, S., Caswell, A. W., Jiang, N., Lynch, A., Noble, D. R., Menon, S., Seitzman, J. M., and Lieuwen, T. C., 2014, "Flame and Flow Topologies in an Annular Swirling Flow," Combust. Sci. Technol., 186(8), pp. 1041–1074.

[95] Kewlani, G., Shanbhogue, S., and Ghoniem, A., 2016, "Investigations into the Impact of the Equivalence Ratio on Turbulent Premixed Combustion Using Particle Image Velocimetry and Large Eddy Simulation Techniques: 'V' and 'M' Flame Configurations in a Swirl Combustor," Energy Fuels, 30(4), pp. 3451–3462.

[96] Berrino, M., Lengani, D., Satta, F., Ubaldi, M., Zunino, P., Colantuoni, S., and Di Martino, P., 2015, "Investigation of the Dynamics of an Ultra Low NOx Injection System by POD Data Post-Processing," ASME Turbo Expo 2015: Turbine Technical Conference and Exposition, American Society of Mechanical Engineers, p. V04AT04A049–V04AT04A049.

[97] Park, S., Gomez-Ramirez, D., Gadiraju, S., Kedukodi, S., Ekkad, S., Moon, H.-K., Kim, Y., and Srinivasan, R., 2017, "Flow Field and Wall Temperature Measurements for Reacting Flow in a Lean Premixed Swirl Stabilized Can Combustor," ASME Turbo Expo

2017: Turbomachinery Technical Conference and Exposition, American Society of Mechanical Engineers, p. V05CT17A009–V05CT17A009.

[98] R. J. Moffat, “Gas temperature measurement,” in Temperature; Its Measurement and Control in Science and Industry, Volume 2, 1962, p. 553.

[99] R. Giezendanner-Thoben, U. Meier, W. Meier, J. Heinze, and M. Aigner, “Phase-locked two-line OH planar laser-induced fluorescence thermometry in a pulsating gas turbine model combustor at atmospheric pressure,” Applied optics, vol. 44, no. 31, pp. 6565–6577, 2005.

[100] R. L. Gordon, A. R. Masri, and E. Mastorakos, “Simultaneous Rayleigh temperature, OH- and CH2O-LIF imaging of methane jets in a vitiated coflow,” Combustion and Flame, vol. 155, no. 1–2, pp. 181–195, Oct. 2008.

[101] H. Uchiyama, M. Nakajima, and S. Yuta, “Measurement of flame temperature distribution by IR emission computed tomography,” Applied optics, vol. 24, no. 23, pp. 4111–4116, 1985.

[102] Y. R. Sivathanu and G. M. Faeth, “Infrared radiation statistics of nonluminous turbulent diffusion flames,” Ann Arbor, vol. 1050, pp. 48109–2140, 1991.

[103] C. Jir-Ming and Y. Jun-Hsien, “The measurement of open propane flame temperature using infrared technique,” Journal of Quantitative Spectroscopy and Radiative Transfer, vol. 56, no. 1, pp. 133–144, 1996.

[104] S. K. Jha, S. Fernando, and S. D. F. To, “Flame temperature analysis of biodiesel blends and components,” Fuel, vol. 87, no. 10–11, pp. 1982–1988, Aug. 2008.

[105] G. Parent, Z. Acem, S. Lechêne, and P. Boulet, “Measurement of infrared radiation emitted by the flame of a vegetation fire,” International Journal of Thermal Sciences, vol. 49, no. 3, pp. 555–562, Mar. 2010.

[106] http://www.schott.com/advanced_optics/english/products/optical-components/optical-filters/optical-filter-glass/index.html

[107] A. V. Dvurechenskii, V. A. Petrov, V. Y. Reznik, V. V. Kornev, and G. Y. Levenfel’d, “Investigation of spectral absorption coefficient of KI and KV quartz glasses in IR region to upper temperature limit,” Journal of Applied Spectroscopy, vol. 31, no. 3, pp. 1157–1160, 1979.

[108] E. C. Beder, C. D. Bass, and W. L. Shackleford, “Transmissivity and Absorption of Fused Quartz Between 0.22 μ and 3.5 μ from Room Temperature to 1500° C,” Applied Optics, vol. 10, no. 10, pp. 2263–2268, 1971.

[109] R. O. Buckius and C. L. Tien, “Infrared flame radiation,” International Journal of Heat and Mass Transfer, vol. 20, no. 2, pp. 93–106, 1977.

[110] Chantasiriwan, S., 1999. Inverse heat conduction problem of determining time-dependent heat transfer coefficient. International Journal of Heat and Mass Transfer, 42(23), pp.4275-4285.

[111] Haghighi, M.G., Eghtesad, M., Malekzadeh, P. and Necsulescu, D.S., 2008. Two-dimensional inverse heat transfer analysis of functionally graded materials in estimating time-dependent surface heat flux. Numerical Heat Transfer, Part A: Applications, 54(7), pp.744-762.

[112] Huang, C.H. and Wang, S.P., 1999. A three-dimensional inverse heat conduction problem in estimating surface heat flux by conjugate gradient method. International Journal of Heat and Mass Transfer, 42(18), pp.3387-3403.

[113] Huang, C.H. and Tsai, Y.L., 2005. A transient 3-D inverse problem in imaging the time-dependent local heat transfer coefficients for plate fin. Applied Thermal Engineering, 25(14), pp.2478-2495.

[114] Lee, H.L., Chang, W.J., Chen, W.L. and Yang, Y.C., 2012. Inverse heat transfer analysis of a functionally graded fin to estimate time-dependent base heat flux and temperature distributions. Energy Conversion and Management, 57, pp.1-7.

[115] Wang, T., Lin, M. and Bunker, R.S., 2005. Flow and heat transfer of confined impingement jets cooling using a 3-D transient liquid crystal scheme. International Journal of Heat and Mass Transfer, 48(23), pp.4887-4903.

[116] Lin, M. and Wang, T., 2002. A transient liquid crystal method using a 3-D inverse transient conduction scheme. International journal of heat and mass transfer, 45(17), pp.3491-3501.

[117] Rutledge, J.L. and Mccall, J.F., The United States of America, as represented by the Secretary of the Air Force, 2016. Method for determining time-resolved heat transfer coefficient and adiabatic effectiveness waveforms with unsteady film cooling. U.S. Patent 9,316,547.